2017

Actuation, Sensing And Control For Micro Bio Robots

Denise Wong
University of Pennsylvania, denwong@seas.upenn.edu

Actuation, Sensing And Control For Micro Bio Robots

Abstract
The continuing trend in miniaturization of technology, advancements in micro and nanofabrication and improvements in high-resolution imaging has enabled micro- and meso-scale robots that have many applications. They can be used for micro-assembly, directed drug delivery, microsurgery and high-resolution measurement. In order to create microrobots, microscopic sensors, actuators and controllers are needed. Unique challenges arise when building microscale robots. For inspiration, we look toward highly capable biological organisms, which excel at these length scales. In this dissertation we develop technologies that combine biological components and synthetic components to create actuation, sensing and assembly onboard microrobots. For actuation, we study the dynamics of synthetic micro structures that have been integrated with single-cell biological organisms to provide un-tethered onboard propulsion to the microrobot. For sensing, we integrate synthetically engineered sensor cells to enable a system capable of detecting a change in the local environment, then storing and reporting the information. Furthermore, we develop a bottom-up fabrication method using a macroscopic magnetic robot to direct the assembly of inorganic engineered micro structures. We showcase the capability of this assembly method by demonstrating highly-specified, predictable assembly of microscale building blocks in a semi-autonomous experiment. These magnetic robots can be used to program the assembly of passive building blocks, with the building blocks themselves having the potential to be arbitrarily complex. We extend the magnetic robot actuation work to consider control algorithms for multiple robots by exploiting spatial gradients of magnetic fields. This thesis makes contributions toward actuation, sensing and control of autonomous micro systems and provides technologies that will lead to the development of swarms of microrobots with a suite of manipulation and sensing capabilities working together to sense and modify the environment.

Degree Type
Dissertation

Degree Name
Doctor of Philosophy (PhD)

Graduate Group
Mechanical Engineering & Applied Mechanics

First Advisor
Vijay Kumar

Keywords
Biology, Magnetics, Micro/Nano robotics, Robotics, Synthetic Biology

Subject Categories
Mechanical Engineering | Robotics

ACTUATION, SENSING AND CONTROL FOR MICRO BIO ROBOTS

Denise Wong

A DISSERTATION

in

Mechanical Engineering and Applied Mechanics

Presented to the Faculties of the University of Pennsylvania

in

Partial Fulfillment of the Requirements for the

Degree of Doctor of Philosophy

2017

Vijay Kumar, Ph.D., Supervisor of Dissertation
Professor of Mechanical Engineering and Applied Mechanics and Nemirovsky Family Dean of Penn Engineering, University of Pennsylvania

---

Kevin Turner, Ph.D., Graduate Group Chairperson
Professor of Mechanical Engineering and Applied Mechanics, University of Pennsylvania

Dissertation Committee

Mark Yim, Ph.D., Professor of Mechanical Engineering and Applied Mechanics, University of Pennsylvania
Vijay Kumar, Ph.D., Professor of Mechanical Engineering and Applied Mechanics and Nemirovsky Family Dean of Penn Engineering, University of Pennsylvania
Kathleen J. Stebe, Ph.D., Richer & Elizabeth Goodwin Professor of Chemical and Biolmolecular Engineering, University of Pennsylvania
M. Ani Hseih, Ph.D., Associate Professor of Mechanical Engineering and Mechanics, Drexel University

ACTUATION, SENSING AND CONTROL FOR MICRO BIO ROBOTS

Denise Wong

Dedicated to Mum and Kim

Acknowledgments

First and foremost, I would like to thank my advisor, Vijay Kumar for the opportunity to carry out this multi-disciplinary research and work with collaborators in a wide range of fields. The freedom to explore new directions with your guidance and support was invaluable and allowed me to develop into an independent researcher. I would also like to give thanks to my committee members for their feedback and thoughtful discussions.

A special thanks to Ed Steager, who has been my mentor, collaborator and friend from the very beginning. He has been a partner and sounding board on all the projects in this thesis. Thank you for the hours of great conversation about research, life and everything in between. You were a source of optimism and light when we were running experiments in the dark. We are evidence that no idea is too crazy to try! I'd also like to thank all my collaborators. In particular, Kate Stebe and Iris Liu contributed their expertise in surface interactions. I also want to thank Elizabeth Hunter for the countless research discussions.

I have made lifelong friendships at Penn. I was fortunate enough to begin my PhD with a stellar team of academics in the MEAM department. Special thanks to Justin Thomas and Alison Patteson for your friendship and support and to Rebecca Khurshid for her bountiful energy, advice and encouragement. I would also like to thank all the members of MRSL and GRASP lab for enriching my Penn experience both in and outside of the lab.

I am grateful for the unconditional support of Alex Tozzo, who constantly challenges me to be better. Last and wholeheartedly, thank you to my family for unconditionally supporting me throughout my entire academic journey. This thesis would not have been possible without you all.

ABSTRACT

ACTUATION, SENSING AND CONTROL FOR MICRO BIO ROBOTS

Denise Wong

Vijay Kumar, Ph.D.

The continuing trend in miniaturization of technology, advancements in micro and nanofabrication and improvements in high-resolution imaging has enabled micro- and meso-scale robots that have many applications. They can be used for micro-assembly, directed drug delivery, microsurgery and high-resolution measurement. In order to create microrobots, microscopic sensors, actuators and controllers are needed. Unique challenges arise when building microscale robots. For inspiration, we look toward highly capable biological organisms, which excel at these length scales. In this dissertation we develop technologies that combine biological components and synthetic components to create actuation, sensing and assembly onboard microrobots. For actuation, we study the dynamics of synthetic micro structures that have been integrated with single-cell biological organisms to provide un-tethered onboard propulsion to the microrobot. For sensing, we integrate synthetically engineered sensor cells to enable a system capable of detecting a change in the local environment, then storing and reporting the information. Furthermore, we develop a bottom-up fabrication method using a macroscopic magnetic robot to direct the assembly of inorganic engineered micro structures. We showcase the capability of this assembly method by demonstrating highly-specified, predictable assembly of microscale building blocks in a semi-autonomous experiment. These magnetic robots can be used to program the assembly of passive building blocks, with the building blocks themselves having the potential to be arbitrarily complex. We extend the magnetic robot actuation work to consider control algorithms for multiple robots by exploiting spatial gradients of magnetic fields. This thesis makes contributions toward actuation, sensing and control of autonomous micro systems and provides technologies that will lead to the development of swarms of microrobots with a suite of manipulation and sensing capabilities working together to sense and modify the environment.

Contents

Acknowledgments **iv**

Abstract **v**

Contents **vi**

List of Tables **ix**

List of Figures **x**

1 Introduction **1**

2 Literature Review **5**
2.1 Swimming At Low Reynolds Number 5
2.1.1 Flagellated Bacteria Swimming 6
2.1.2 Microbiorobots Actuated By Bacteria 6
2.1.3 Controlling Biological Systems 7
2.2 Biological Sensors 8
2.3 Magnetically actuated robots 8
2.3.1 Control of Multiple Magnetic Robots 9

3 Sensing using Biology **11**
3.1 Introduction 12
3.2 Methods 13
3.2.1 Experimental Setup 14
3.2.2 Microrobot Fabrication 14
3.2.3 Fabrication of Plasmids and Strains 14
3.2.4 Fabrication of Biosensors 15
3.2.5 Flow Cytometry 15
3.2.6 Microscopy and Tracking 16
3.2.7 UV Exposure 16
3.3 Low Power Toggle Cells 17
3.3.1 Biochemical Model 17
3.3.2 Mathematical Model 19
3.3.3 Cell Validation 20

3.4 Results . . . 21
3.4.1 Biosensor Transport . . . 21
3.4.2 Sensor Response . . . 21
3.5 Conclusion . . . 25

4 Actuation Using Biology **27**
4.1 Bacteria Powered Microrobots . . . 27
4.1.1 Experimental Setup . . . 28
4.2 Stochastic Kinematic Model . . . 28
4.2.1 System Description . . . 30
4.2.2 Equations of Motion . . . 30
4.3 Orientation Experiment . . . 33
4.3.1 Results . . . 33
4.4 Edge Effect . . . 34
4.4.1 Results . . . 35
4.5 Actuation By Active Suspension . . . 38
4.5.1 Results . . . 39
4.6 Modeling Fluid Drag on an MBR . . . 41
4.7 Chemotactic Bottom-up Model . . . 43
4.7.1 Preliminary Results . . . 47
4.8 Conclusion . . . 47

5 Actuation using Magnetic Fields **49**
5.1 Magnetics Background . . . 50
5.2 Magnetic System Characterization . . . 53
5.2.1 Magnetic Field Characterization . . . 53
5.2.2 Robot Characterization . . . 57
5.3 Conclusion . . . 62

6 Control of Multiple Robots **64**
6.1 Control of Multiple Magnets in 1D . . . 64
6.1.1 Linear Configuration . . . 65
6.1.2 System Implementation . . . 68
6.1.3 Results . . . 72
6.2 Control of Multiple Magnets in a Plane . . . 75
6.2.1 Problem Formulation . . . 75
6.2.2 Approximate Model . . . 77
6.2.3 Simulation . . . 79
6.2.4 System Design . . . 81
6.2.5 Experimental Results . . . 82
6.2.6 Relevance to Microscale Systems . . . 85
6.2.7 Discussion . . . 86
6.3 Simulations of Multi-Magnet Control . . . 88
6.3.1 Simulation Design . . . 88
6.3.2 Simulation Results . . . 91
6.4 Conclusion . . . 95

7 Applications to Assembly **96**
7.1 Introduction and Related Work . . . 96
7.2 Capillarity Background . . . 99
7.3 System Design . . . 101
7.3.1 Magnetic Robots . . . 102
7.3.2 Passive Particles . . . 103
7.3.3 Feedback Control . . . 103
7.4 Experimental Results . . . 104
7.4.1 Assembly Using a Stationary Deformation Source . . . 104
7.4.2 Assembly Using a Mobile Deformation Source . . . 105
7.4.3 Geometry Effects on Assembly Dynamics . . . 107
7.5 Autonomous Assembly . . . 109
7.5.1 System Design Modifications for Autonomous Assembly . . . 109
7.5.2 Results . . . 113
7.6 Design Guidelines and Limitations . . . 114
7.7 Conclusion . . . 116

8 Conclusion **117**
8.1 Contributions . . . 117
8.2 Future Work . . . 119
8.2.1 Organic and Inorganic Microrobots . . . 119
8.2.2 Magnetic Robots for Probing Scientific Phenomenon . . . 120
8.2.3 Multi-Robot Control . . . 120
8.3 Concluding Remarks . . . 121

Bibliography **127**

List of Tables

1 MBR center exposure to near-UV light experiment. 36
2 MBR edge exposure to near-UV light experiment. 37

3 Electromagnetic coils parameters. 57

4 Parameters for experimental setup 72

5 Magnitude of key parameters for multi-magnet manipulation setup 115

List of Figures

1 Illustration of our biosensors . . . 12
2 Biosensor microfabrication . . . 16
3 Schematic showing gene circuit under different inducers and the corresponding activity of genes λcI and lacI. . . . 18
4 Mathematical model of the toggle switch dynamics. . . . 19
5 Flow cytometry analysis of engineered bacterial cells. . . . 21
6 Transport of biosensor substrates. . . . 22
7 Low power toggle cells in low vs high states. . . . 23
8 Sensor readout. . . . 23
9 Mean fluorescence intensity averaged across several distributed sensor micro plates. . . . 24
10 Integrated biosensing microrobots. . . . 24
11 Distributed biosensors. . . . 25

12 Microfabrication of microbiorobots. . . . 29
13 Image and schematics of a microbiorobot . . . 29
14 Forces exerted by bacteria on a microbiorobot. . . . 29
15 Histogram of rotation direction of square microbiorobots with cells attached to the top or bottom of microstructure. . . . 34
16 UV exposure to the center of a square microbiorobot. . . . 35
17 UV exposure to the corner of a square microbiorobot. . . . 36
18 Schematic and results comparing microbiorobots propelled by attached bacteria and free-swimming bacteria. . . . 40
19 Total stress profile of a translating H-shaped microbiorobot. . . . 41
20 Computational fluid dynamic model parameters for an MBR. . . . 43
21 MBR hydrodynamic model results. . . . 44
22 Preliminary modeling results for a predominantly rotating microbiorobot. . . . 45

23 Calibration of magnetic field using a magnetometer . . . 56
24 Empirically deriving the linear drag coefficient of a magnetic robot . . . 61
25 Empirically deriving the rotational drag coefficient of a magnetic robot . . . 62

26 1-D multi-magnet control configuration . . . 66
27 Schematic of 1-D 3 magnet simulation . . . 68
28 Simulation results from 3 magnet configuration . . . 69
29 Empirically determining magnetic parameters . . . 73

30 1-D multi-magnet control experimental results 74
31 Independent control of multiple magnetic robots utilizing spatially varying magnetic field gradients. 75
32 Multi-magnet control experimental implementation 78
33 Multi-magnet control simulation results 79
34 Multi-magnet control experimental results demonstrating the same velocity for two robots 83
35 Multi-magnet control experimental results demonstrating two robots with different trajectories 84
36 Multiple solutions satisfy that same force constraints in a multi-magnet control problem 87
37 Simulation results of 2 magnetic robots 92
38 A closer look at the start of the simulation of 2 magnetic robots 94

39 Magnetic robots as mobile deformation sources to control directed assembly at fluid interfaces 97
40 Capillary driven assembly on curved interfaces 100
41 Disk fabrication by photolithography 104
42 Collection of many passive particles using an actuated magnetic robot 105
43 Geometry effects on assembly dynamics 106
44 Effect of small-scale features on docking location 108
45 Autonomous robot for directed assembly 110
46 Assembly dynamics of microsphere assembly to triangular robot 113

Chapter 1

Introduction

We can imagine tiny robots being used for surveillance, environmental clean-up and in medicine. In medicine, compelling applications include directed drug delivery for localized disease treatment, minimally invasive surgery to enable new procedures and reduce recovery time and real-time health monitoring using embedded robots in the body to relay information to a doctor. In some sense, the white blood cell can be seen as the ultimate medical microrobot. It is able to circulate through the body in the blood stream in a passive state monitoring the environment. When an infection is detected, the white blood cell responds with a variety of methods depending on the type of white blood cell and the infection detected. The responses include creating antibodies to fight infection or engulfing the harmful foreign particle.

As the length scale of robots continues to decrease and approach the size of a single biological cell, applications in biological research emerge. Microrobots enable the investigation of microbiology in ways which were not previously possible. Recent rapid fundamental progress in microrobotics has given rise to applications including single-cell analysis, in vitro drug delivery to neurons and micro assembly of biologically infused hydrogels with applications in tissue engineering.

This dissertation extends these capabilities toward enabling microrobots for in vivo applications. Capabilities that an in vivo medical microrobot would need include tetherless

precise actuation, onboard sensing to detect stimuli present in the environment and information processing to respond to these changes. In the field of micro and nanofabrication, we will need new techniques to create these tiny complex structures.

In the most general sense, microrobots are engineered systems which operate on micrometer length scales, typically with characteristic dimensions less than 100 microns. Unique challenges arise when developing microrobots. Firstly, power sources and storage do not typically come in such small packages. Power is necessary for actuation and sensing activities. Secondly, sensors also do not come in such small packages. In addition to developing sensing capability on board microrobots it is necessary to store the data and then overcome the microscale-to-world interface problem to report the signal. Thirdly, addressing individual robots at this length scale is challenging because unique inputs are needed in a very small space. Typically, global inputs are used, which affect the entire system making it difficult to generate different responses between robots. Moreover, different physical phenomena dominate at this length scale. Therefore, it is not feasible to simply miniaturize solutions used on the macroscopic scale to create microrobots. It is important to appreciate these phenomena and the effects that they have on the behavior of microrobots. These differing physical phenomenon give rise to new opportunities for manipulation and control at the microscale. Chapter 2 provides background information on swimming at low Reynolds number and a literature review on related work.

This dissertation contributes to the field of microrobotics by developing technologies and methods that can be used to overcome some of the challenges that arise when creating robots at this length scale. We look to create systems that are a fusion of organic and inorganic components. From a bottom-up approach we have synthetically engineered biological organisms to be useful onboard sensors capable of taking in a signal, processing it and providing a readout. We also used single cell biological organisms as motors to provide untethered onboard power. At a slightly larger scale, we directed the assembly of inorganic engineered structures that will eventually be synthesized with the biological components.

Biology has created elegantly packaged self-contained sensors. In Chapter 3, we demon-

strate sensing by integrating genetically engineered, ultraviolet light-sensing bacteria with magnetic microrobots, creating the first controllable biological microrobot that is capable of exploring, recording and reporting on the state of the microscale environment. We demonstrate two proof-of-concept prototypes: (a) an integrated microrobot platform that is able to sense biochemical signals, and (b) a microrobot platform that is able to deploy biosensor payloads to monitor biochemical signals, both in a biological environment.

We accomplish actuation, sensing and control in microrobots in a variety of ways on several different platforms. In Chapter 4, we begin by exploring actuation. First, by integrating organic and in-organic components using flagellated bacteria to create untethered robots with onboard power. We probe the dynamics of the system by selectively immobilizing the biological motors attached to the microrobot to understand the forces that are being exerted. This informed a stochastic kinematic model that captures the predominant clockwise rotation of the microrobot when not affected by any external stimuli. Additionally, a bottom-up model is proposed to capture the stochasticity of such a system by modeling the individual cell on the microrobot.

Controlling biologically actuated robots is very challenging due to the stochasticity inherent in biological systems. For tasks that require high-precision position control, a more deterministic system may be preferable. Chapter 5 discusses the modeling of electromagnetic coils for the manipulation of magnetic microrobots as well as strategies for calibration of a magnetic manipulation system and the challenges which arise.

In Chapter 6, we consider, at a slightly larger scale, the control of single and multiple magnetically actuated robots using stationary electromagnetic coils. This work enables more complex micro manipulation tasks by enabling the control of multiple agents to accomplish grasping motions in addition to pushing.

To address challenges in micro and nanofabrication, we develop a bottom-up manufacturing technique to assemble complex microstructures from simple building blocks which uses capillary forces that arise at fluid interfaces. In Chapter 7, the magnetic actuation work is applied to enable the assembly of passive particles. The magnetically controlled robot acts

as a fluid interface deformation source to direct assembly of passive building blocks driven by capillarity. We leverage tools from interface physics to create a robust framework that can be used for automated micro assembly. In this chapter, we also discuss design guidelines and limitations of the system for future iterations of a magnetic manipulation system.

Chapter 2

Literature Review

Cells are compelling candidates for use in microscale systems for two particular reasons. Firstly, biological cells are self-contained systems which do not need an external power source. Secondly, they have the natural ability to respond to environmental cues, such as changes in chemical concentration, light exposure, and even magnetic field orientation. This sensory framework is contained in an exquisitely small package, which in the case of the rod-shaped bacteria *Escherichia coli* is typically 1 μm in diameter and 2 μm in length.

This chapter reviews the relevant concepts in low Reynolds number physics and related literature that will be used throughout the dissertation. Section 2.1 reviews concepts on swimming at low Reynolds number and related literature on bacteria propelled microrobots. Section 2.2 reviews related literature on using biological sensors. Section 2.3 reviews related literature in magnetic microrobot actuation and control for single and multiple robots.

2.1 Swimming At Low Reynolds Number

Building microscale robotic systems starts with understanding physics, specifically the fluid mechanics, at low Reynolds number. The Reynolds number, Re, is a non-dimensional number which compares the importance of inertial effects to viscous effects. The Reynolds number is defined by $Re = \frac{\rho U l}{\eta}$, where η, kinematic viscosity, and ρ, density, are fluid properties and l, characteristic length scale, and U, velocity, are boundary conditions and determined

by the robotic system in this case. In low Reynolds number environments, $Re << 1$, viscous effects dominate over inertial effects. Motion is determined by forces at that instant, independent of forces before or after this time [57]. The implications of this changes swimming strategies at macroscale compared to at microscale. In microscale, the swimming motion must be time reversible and non-reciprocal to result in a net displacement. Practically, this means that a video of forward swimming using non-reciprocal motion will look different when played backwards. Several different mechanisms are used by biological organisms for swimming at low Reynolds number, we focus on biological swimming of organisms using the rotation of helical flagella.

2.1.1 Flagellated Bacteria Swimming

Flagellated bacteria, such as *E.coli* and *S.Marcescens*, are made up of a cell body and many hair-like flagella coming off of the cell body. These flagella are helical and have a common and fixed chirality. These bacteria swim in fluidic environments by rotating these flagella. When all the flagella attached to the cell body are rotating in the same counter-clockwise direction (when viewed from behind), the flagella bundle together and the rotation generates a propulsive force that causes the cell to swim forward, executing a run [21]. When the rotation of a single flagellum switches direction, the flagella bundle is unraveled and a propulsive force is no longer present, instead this unbundling causes a torque and the cell rotates, executing a tumble. This mechanism of switching between run-and-tumble is what flagellated bacteria use to change direction when swimming. When flagellated bacteria swim in free solution, the motion can be approximated as a random walk [27], with a run to tumble ratio of 10:1.

2.1.2 Microbiorobots Actuated By Bacteria

The use of a bacterial carpet for creating flow patters in fluids was first observed by Darnton *et al.* [18]. In their experiments, they attached a monolayer of *S. marcescens* to a solid substrate and observed the trajectory of passive tracer beads above the monolayer of bacteria. The trajectories of particles close to the bacterial carpet when compared to trajectories of

particles further away indicate active fluid mixing close to the bacterial carpet as a result of the rotation of the bacteria flagella.

Flagellated bacteria can be attached directly to microstructures to provide onboard power [4, 67]. The bacteria on these structures coordinate to propel the microstructures in fluidic environments. Sakar *et al.* created a stochastic kinematic model for an MBR which is comprised of a microfabricated microstructure made from negative photoresist (SU-8) coated with a monolayer of swarming *S. marcescens* [61]. Instead of calculating the exact force exerted by each bacterium, this model parameterizes the distribution of the bacteria across the microstructure to predict the behavior of the MBR; these values are derived empirically. While these high level parameters are sufficient to describe the trajectory of the microstructure by taking into account the force exerted by the bacterium, it does not take into account the non-contact, hydrodynamic surface interaction that arises from the flagella of the bacteria near the edge of the MBR interacting with the planar surface under the MBR. We extend this stochastic kinematic model by adding additional high level parameters to capture both the propulsion by the bacteria and this hydrodynamic surface interaction.

2.1.3 Controlling Biological Systems

Several different methods have been proposed for controlling MBRs which comprise of flagellated bacteria attached to passive microstructures. Steager et al. use electrokinetic and galvanotactic behavior to control MBRs propelled by *S. marcescens* [68]. Behkam et al. toggle the on-off behavior of the biological motors of *S. marcescens* used to propel polystyrene beads through the addition of chemicals into the solution. By adding copper ions, the bacterial flagellar motors are stopped and the motion of bead is stopped, by adding ethylenediaminetetraacetic acid (EDTA) [4]. Zhuang et al. use chemotaxis to gather MBRs to a specific region defined by pH across a pH-gradient created in a microfluidic channel [89]. Phototaxis can also be used to control the behavior of bacterial actuators. Exposure to UV light will cease the motion of *S. marcescens*, this can be used to control microstructures that are propelled by cell that are attached to the microstructure [67] as well as cells that are in free solution [34].

2.2 Biological Sensors

In addition to being used for propulsion and control, the natural environmental responses of cells have been used in motility-based biosensors, where readout is performed based on the motility of the cells [69]. The sensory network in cells can also be used as onboard sensors on MBRs. We can leverage the rapid advancements in synthetic biology which have enabled the design of cells with highly specified functionality through genetic engineering [58]. By utilizing the ability to edit the genes of model organisms, like *E. coli*, the behavior of the cells or biosensors can be programmed. This programmability can extend well beyond innate sensing capabilities.

Synthetic gene networks have been designed to create digital signal processing capabilities such as bi-stable gene expression to create a toggle switch behavior that act as cell-based memory units [28]. Molecular systems can be constructed from predefined elements to perform multi-input logic computations within mammalian cells, where these components can be combined to create a biomolecular computer [60]. Moreover, synthetic gene networks have been constructed to emulate cell-based digital circuits based on principles of modern computing, such as counters[26]. Population behaviors can also be used to create edge detectors using light sensitive cells [77]. Furthermore, by employing existing mechanisms for quorum-sensing that enable communication between cells, capabilities can be extended to include population-level sensing and decision making [81].

2.3 Magnetically actuated robots

Magnetic actuation has also been demonstrated as a method for manipulation and has gained particular traction because of several properties that make it ideal for microrobot manipulation. Firstly, magnets can be controlled with and without line of sight, which allows the robot to be used in small and difficult to reach areas. Secondly, magnetic fields are widely accepted as safe to biological cells and tissue, and are already widely used in the medical field [25]. Numerous systems have been developed for magnetic manipulation of micro and meso-scale magnets using electromagnetic coils [36, 40, 52, 71]. In general, these

systems have been designed to manipulate one magnetic robot by controlling the global field of the workspace uniformly.

Microscale robots have demonstrated applications in biology such as cell manipulation and directed drug delivery [71]. Additionally, microrobots with sensing capabilities for measuring small forces [35, 74, 76] and external optical stimuli [73] have been developed.

2.3.1 Control of Multiple Magnetic Robots

A variety of methods have been demonstrated for the control of multiple magnetic microrobots. Magnetic actuation is an effective method for applying large forces, but individually addressing magnetic robots is challenging because magnets respond similarly in a global field. Khalil et al. [38] controlled a cluster of 100 μm diameter paramagnetic microparticles to manipulate microstructures in a plane for microassembly. Multiple microparticles are manipulated together to push non-magnetic microstructures into a desired position. While multiple microparticles are manipulated, all the particles move in the same general direction and microparticles are not individually addressable. Strategies for transport of passive payloads using a team of homogeneous robots controlled by global inputs are discussed by Becker et al. [3].

Heterogeneous teams of magnetic microrobots generate different resultant forces under the same global field. Diller et al. [20] used a team of microrobots which are geometrically different but had similar effective magnetization, which resulted in different rotational inertia and therefore angular acceleration. Position control of 3 robots, each having dimensions less than 1 mm, is demonstrated; however, the motion of the robots is coupled and arbitrary trajectories are not possible. Cheang et al. [15] demonstrated control of 2 geometrically similar and magnetically heterogeneous microswimmers using a global rotating magnetic field. By balancing the applied magnetic torque and the hydrodynamic torque, simultaneous control of two microswimmers moving in opposing directions with arbitrary speeds can be achieved. Mahoney et al. [42] demonstrated control of two helical microrobots using robots with different magnetization and friction such that different forward swimming speeds result from the same magnetic field rotation frequency. The direction traveled at a given time step

is the same but the velocity is different, which allows trajectories of the same shape but different size to be achieved. In these three methods, two microswimmers cannot swim in the same direction at the same velocity because the robots are heterogeneous.

Specialized printed circuit boards have been used to manipulate local magnetic fields on a surface to control multiple microrobots. Pelrine et al. [54] used layers of parallel and perpendicular traces on a printed circuit board to manipulate mm-sized magnetic robots. The current through the traces generate a local magnetic field and by varying the current through the traces the position of the robot is controlled. Cappelleri et al. [11] used microcoils on a printed circuit board to control multiple magnetic microrobots by affecting the local magnetic field. Planning and control algorithms for multiple microrobots on a planar system controlled by these microcoils are discussed by Chowdhury et al. [17]. Pawashe et al. [53] used a surface with electrostatic pads to selectively brake magnets and prevent them from moving while allowing the manipulation of other magnets away from the pad. These brakes are in fixed locations and the allowable trajectories are dominated by the position of the pads.

Apart from electromagnetic coils, mobile permanent magnets have also been used to control magnetic microrobots. Nelson and Abbott [48] demonstrated the ability to manipulate two magnetic devices by manipulating a single rotating magnetic dipole around the workspace. Converging, diverging and similar trajectories are achieved by exploiting the different magnetic field and field gradient at various locations around the magnetic dipole.

Chapter 3

Sensing using Biology

Microscale robots offer an unprecedented opportunity to perform tasks at resolutions approaching 1 μm, but the great majority of research to this point focuses on actuation. Potential applications for microrobots can be considerably expanded by integrating sensing, signal processing and feedback into the system. Due to the similarity in length scale to single cells, microrobots enable the investigation of microbiology in ways which were not previously possible. In Chapter 4, microrobots are used to probe the dynamics of the biological cells used to propel the robot. Biological organisms also have a natural inherent ability to sense their environment.

This chapter explores the integration of synthetic biology with microrobotic systems to create cell-based programmable mobile sensors, with signal processors and memory units. Specifically, we integrate genetically engineered, ultraviolet light-sensing bacteria with magnetic microrobots, creating the first controllable biological microrobot that is capable of exploring, recording and reporting on the state of the microscale environment. We demonstrate two proof-of-concept prototypes: (a) an integrated microrobot platform that is able to sense biochemical signals, and (b) a microrobot platform that is able to deploy biosensor payloads to monitor biochemical signals, both in a biological environment. These results have important implications for integrated micro-bio-robotic systems for applications in biological engineering and research.

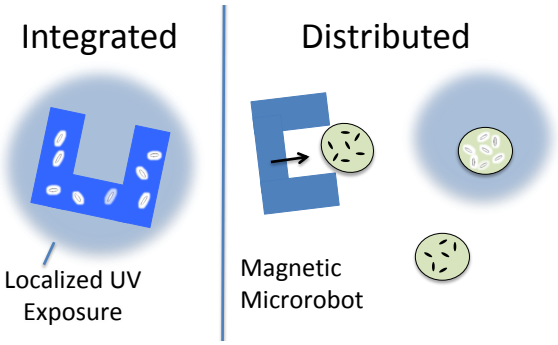

Figure 1: Biosensors. Cells engineered to sense UV radiation are attached either directly to the Integrated magnetic microrobot (left), or attached to Distributed passive microplates (right). The integrated approach is useful for rapid exploration of a workspace, but cell response and readout is on the order of hours. The distributed approach requires arrangement of several passive sensors, but mapping can be performed more quickly due to greater coverage.

The research in this chapter was originally published in [73].

3.1 Introduction

Rapid advancements in synthetic biology have enabled the design of cells with highly specified functionality through genetic engineering [58]. Cells are compelling candidates for use in microscale systems for two particular reasons. Firstly, biological cells are self-contained systems which do not need an external power source. Secondly, they have the natural ability to respond to environmental cues, such as changes in chemical concentration, light exposure, and even magnetic field orientation. This sensory framework is contained in an exquisitely small package, which in the case of the rod-shaped bacteria *Escherichia coli* is typically 1 μm in diameter and 2 μm in length. Given the extensive knowledge base on the genetic and proteomic makeup of model organisms such as *E.coli*, as well as rapid advances in genetic engineering, we can extend the idea of cells being good natural candidates for microscale biosensors to the concept of these cells being *programmable*. This programmability can be extended well beyond innate sensing capabilities. Combining advancements in both microrobotics and synthetic biology is an investigative path with significant potential [62].

3.2 Methods

We demonstrate a microrobotic system capable of sensing environmental changes with spatial resolutions at the scale of individual cells. We combine two technologies: (a) the ability to create mobile microrobots using magnetic actuation; and (b) tools from synthetic biology to create novel biosensors. These biosensors are designed to sense low doses of ultraviolet (UV) light. The information is stored in a *toggle switch* architecture, a switch that allows cells to toggle between stable states based on environmental stimuli, and the information readout is performed via production of fluorescent proteins within the cell. This form of sensing is useful for seeking potentially pathological conditions. The UV sensor is used here as a proxy for chemical biosensors, since it is simpler for proof-of-concept demonstrations with UV light, and, because of the similarity in architecture, it is not too difficult to engineer similar cells that can sense biochemicals.

We investigate two methodologies (Figure 1) for microrobotic biosensing systems. The first method, which we refer to as an integrated system, utilizes cells directly attached to magnetic microrobots. The integrated system enables rapid exploration of a region, however, the biosensor readout timescale is considerably longer than actuation time by the robot. Thus, actuation time is greatly restricted by readout. In the second method, which we call a distributed system, we attach cells to microscale plates that are then independently arranged by a single magnetic robot. In this system, several biosensors are rapidly arranged to cover a region. In both systems, the sensor consists of a population of cells, whether they are attached to the microrobot or the passive microscale plate.

A single cell is not a reliable biosensor because individual cells exhibit stochastic behavior. However, reliable results can be obtained for groups of cells. Fluorescence microscopy is used to read out the response of cell populations. Specifically, we show how sensors can be transported and read out to indicate the presence of UV radiation.

3.2.1 Experimental Setup

The experimental setup consists of four in-plane electromagnetic coils which use magnetic field gradients to actuate the magnetic microrobots. The coils are integrated on the stage of an epifluorescence microscope. The precise details of the setup have been previous described in detail and modeled [71].

3.2.2 Microrobot Fabrication

Microrobots are fabricated in a single-exposure process using traditional microfabrication techniques [63]. First a layer of 10% dextran in spin-coated on a clean glass slide, which acts as a sacrificial release layer. Next, a 2 μm layer of SU8-2002 is spin-coated. This layer is necessary as a mediating interface and enables uniform coating in the subsequent spin-coating step. Next, SU8 mixed with 5% iron oxide nanoparticles is spin-coated to a thickness in the range of 4-10 μm. A dark-field photomask is used during the exposure step, and the entire slide is then developed in PGMEA and dried with nitrogen.

3.2.3 Fabrication of Plasmids and Strains

Plasmids pHPTa and pCIRa were derived from the published pTAK plasmids and pZ expression vectors and previously published [28]. The plasmid pLPTa was built by performing site-directed mutagenesis on pHPTa to change the Glutamine at residue 233 of the cI protein to a Lysine to confer more sensitivity to UV irradiation. Co-transformations of pLPTa and pCIRa into *E.coli* strain JM2.300 yielded the experimental strain for all data collection. The experimental strains were cultured at 37°C in LB broth (BD Biosciences) supplemented with appropriate levels of ampicillin and tetracycline (Sigma) to maintain selection. Typically, cultures were inoculated with appropriate selection antibiotics and initial isopropyl-beta-thiogalactopyranoside (IPTG) to set toggle state and grown at 37°C for 16 hours. Cells were centrifuged and resuspended in fresh LB broth twice before additional growth periods dependent on downstream experiments.

3.2.4 Fabrication of Biosensors

Biosensors are SU8 epoxy microstructures with bacteria adhered to the surface (Figure 2). The fabrication process is optimized for compatibility with biological cells as well as compatibility with traditional bright-field and fluorescence microscopy. Initially, a water-soluble sacrificial layer of dextran is spin-coated onto a No. 0 glass slide to allow release of biosensors in subsequent experimental steps. On top of the dextran layer, 5-10 μm thick SU8 2000 series negative tone, photosensitive epoxy plates are fabricated using a single exposure through a chrome mask. For this study, a combination of 40, 60 and 80 μm diameter disks were fabricated. *E.coli* cells do not naturally adhere to SU8, so the surface of the plates were treated with 0.1% poly-L-lysine for 10 minutes, a protein which promotes binding of biological cells. The slides were then dried with compressed air. For SU8 experiments, following overnight cultures and subsequent washing away of IPTG, cells were grown in liquid LB media supplemented with appropriate antibiotics at 37°C for 4 hours before being deposited onto poly-L-lysine substrates and allowed to adhere for 5-10 minutes. Excess cells were washed from the surface and biosensors released into the experimental setup by inversion. Integrated biosensors were treated in a similar manner.

3.2.5 Flow Cytometry

Flow cytometry is used to characterize the level of fluorescence of individual cells. For cytometry experiments, following overnight cultures and subsequent washing away of IPTG, cells were grown in liquid culture at 30°C for 2 hours before exposure to UV irradiation (Stratalinker UV Crosslinker 2300) and additional growth at 30°C for 6 hours before analysis using a LSRFortessa cell analyzer (BD Biosciences) equipped with 488-nm argon excitation laser and 530/15 nm emission filter and a PMT setting of 360 V. Measurements were calibrated using Rainbow Calibration Particles (Spherotech RCP-30-5A) to normalize data between different experimental runs. For each sample, 10,000 events were collected.

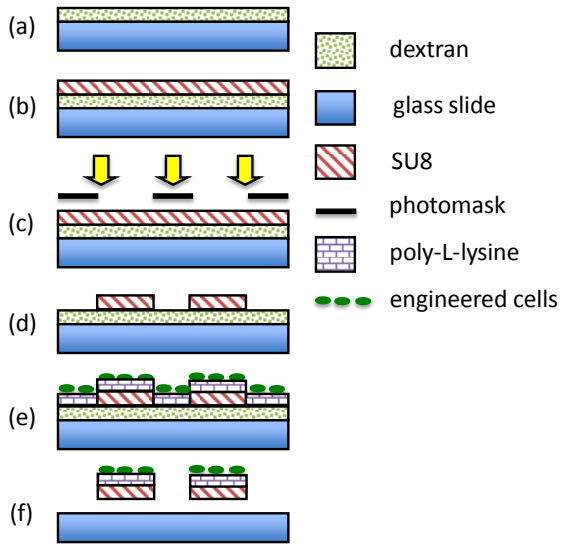

Figure 2: Biosensor microfabrication. (a) Glass slides are coated with dextran, which acts as a water-soluble sacrificial release layer. (b) SU8 forms the substrate of the biosensor. (c-d) Biosensors are patterned with photolithography. (e) Poly-L-lysine is deposited on the biosensor surface to enhance attachment of cells. (f) Microrobots are released in solution and dextran dissolves.

3.2.6 Microscopy and Tracking

Integrated and distributed biosensors were actuated and positioned using bright-field microscopy. Readout was performed using fluorescence at excitation/emission wavelengths optimized for green fluorescence protein (GFP). Although SU8 epoxy is fluorescent at wavelengths close to GFP, the emission spectra of SU8 and GFP do not significantly overlap.

3.2.7 UV Exposure

Cells were exposed to UV light with a mercury lamp with collimation optics. The light source was masked to create discrete regions of UV exposure. Exposure times of 10 seconds were sufficient to induce the population to switch to high state, thus activating the synthetically engineered response of producing Green Fluorescent Protein (GFP), which is a readout for this high state.

3.3 Low Power Toggle Cells

3.3.1 Biochemical Model

Bistability occurs in a genetic circuit when two repressible promoters are arranged in a mutually inhibitory network [28]. Promoters regulate the activity of genes that transcribe proteins. Each promoter, pλ and plac, triggers a gene, lacI and λcI respectively, that regulates the production of a protein, LacR and λCI respectively, which represses the behavior of the other promoter, Figure 3. In the absence of inducers, two stable states are possible: (1) when promoter, plac, transcribes the repressor protein λCI (low-state,) (2) when promoter, pλ, transcribes the repressor protein LacR (high-state.) A transient, externally triggered inducer can be used to switch between these two stable states. Hence the name toggle switch. In this toggle switch, the inducers are chemical inducer IPTG and UV light.

By inducing the cells with IPTG, the transcription of protein LacR is repressed, which results in a high level of activity of gene λcI and the transcription of protein λCI (low-state), Figure 3(b). At low-state promoter pλ is repressed and therefore the activity of gene lacI is low. The cells will stay in low state even after IPTG is removed from the environment Figure 3(c). By inducing the cells with a transient pulse of UV light, the cell switches to high-state. UV light causes repairable DNA-damage wherein the DNA becomes single-stranded, this activates an SOS-pathway and causes degradation of the protein λCI Figure 3(d). The degradation of protein λCI alleviates the repression of promoter pλ, increases the activity of gene lacI and hence the transcription of protein LacR. This protein represses the promoter plac and therefore the activity of gene λcI is low, Figure 3(e). In order to detect that a cell is at high state, transcription of green fluorescent protein (GFP) is synthetically engineered to be triggered by the transcription of the protein LacR. Thus, GFP transcription occurs in parallel with LacR transcription and is used as a signal indicating a cell is at high-state during experiments.

While bistable systems occurs naturally in biology, most are difficult to interface with as the inducers are not easily controlled externally and states are difficult to determine

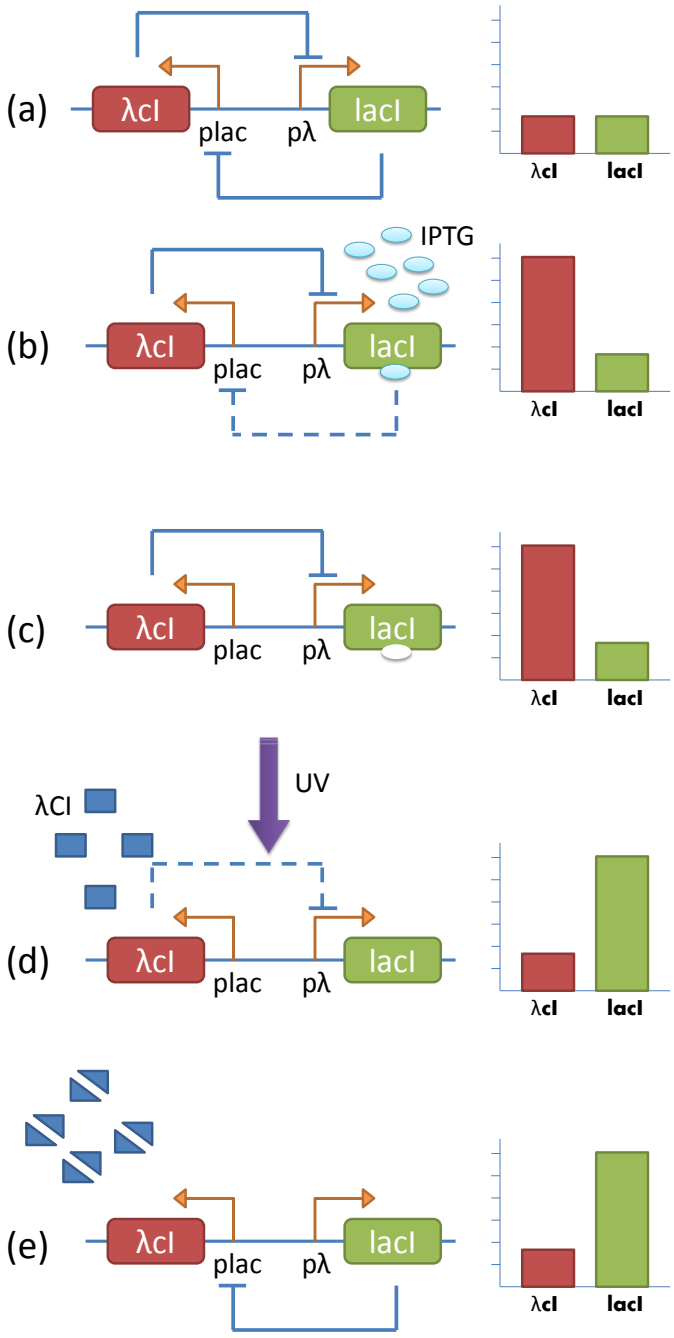

Figure 3: Schematic showing gene circuit under different inducers and the corresponding activity of genes λcI and lacI. (a) No inducer, basal levels of activity of both genes, (b) Induction with IPTG reduces activity of lacI and increases activity of λcI, (c) Low-state, even after IPTG is removed the cell is stable in low-state, (d) Induction with UV light causes the degradation of protein λCI and increases activity of lacI, and is linked to GFP production (e) High-state, even after the UV light is removed the cell is stable in high-state.

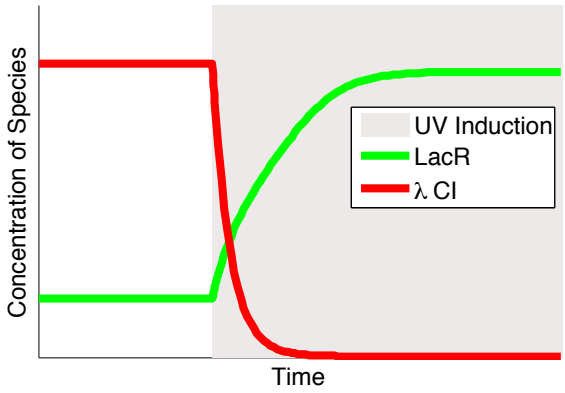

Figure 4: Mathematical model of the toggle switch dynamics. Transition between low-state where protein λCI is abundant and represses the transcription of protein LacR and high-state when protein LacR is abundant and represses the transcription of protein λCI. The time scale for the case in this work is on the order of hours.

externally as well. The specific sensor cell used in the experiments described here are *E.coli* JM2.300 cells synthetically engineered to include plasmids pLPTa and pCIRa. Plasmids are circular DNA molecules separate from the chromosomal DNA within the cell that carries a few genes that can be expressed within the cell. Plasmid pCIRa carries the genes for GFP production which is used as a reporter for high-state[39]. Plasmid pLPT is the regulatory circuit that contains the genes λcI and lacI and controls the expression of GFP in plasmid pCIRa.

3.3.2 Mathematical Model

The interactions between the components in the genetic toggle circuit can be described by a pair of coupled dimensionless nonlinear differential equations [28]:

$$\frac{dU}{dt} = \frac{\alpha_1}{1+V^\beta} - U \ , \ \frac{dV}{dt} = \frac{\alpha_2}{1+U^\gamma} - V$$

where U is the concentration of repressor protein LacR, V is the concentration of repressor protein λCI, α_1 is the effective rate of synthesis of repressor protein LacR, α_2 is the effective rate of synthesis of repressor protein λCI, β is the cooperativity of repression of promoter pλ and γ is the cooperativity of promoter plac.

Figure 4 illustrates the interactions between levels of proteins λCI and LacR. The start

of the graph shows the cell in low-state after IPTG induction when the level of protein λCI is high and level of protein LacR is low. The grey region indicates UV induction, this is modeled by decreasing the effective rate of synthesis of repressor protein λCI, α_2, and decreasing the cooperativity of repression of promoter, pλ. Increasing the effective rate of synthesis of repressor protein LacR, α_1, has a similar effect. UV induction causes a sharp change in the levels of each protein which destabilizes the high λCI state and drives the system to switch to the other stable state where the level of protein λCI is low and the level of protein LacR is high and as a result GFP is expressed. While the UV light exposure is transient, the effects of the induction are lasting; therefore the induction process extends beyond the duration of the UV light exposure.

Stochasticity in this system arises from the combination of bistable architecture with bimolecular processes involving few molecules [50]. This results in bimodal population distributions despite the same experimental conditions and induction levels. It has been shown that even a single-molecule event may trigger such phenotype switching [16]. Therefore, reading the fluorescence signal from multiple cells is important.

3.3.3 Cell Validation

Engineered cells need to be designed, tested and verified in liquid or agar cultures before integrating them with microrobots and sensor plates. Cells in JM2.300 background harboring both plasmids pCIRa and pLPTa as described in the methods were first tested and analyzed in a robot-free environment. Bulk cultures of the genetically engineered cells were grown to stationary phase over 16 hours at 37°C in the presence of IPTG. The introduction of IPTG set the cells into a state of high cI and low LacR with a basal level of GFP fluorescence. The IPTG was subsequently washed out and cells were grown in exponential phase for 3-4 cell divisions (2 hours at 30°C). The culture was split into two aliquots, and one was exposed to 50 μJ/cm^2 UV irradiation. The two independent cultures were then grown for an additional 9-12 cell divisions (6 hours at 30°C) and analyzed by flow cytometry. For cells exposed to UV irradiation compared to cells that did not receive any UV irradiation, there is an approximately 10-fold increase of fluorescence in the GFP channel (Figure 5).

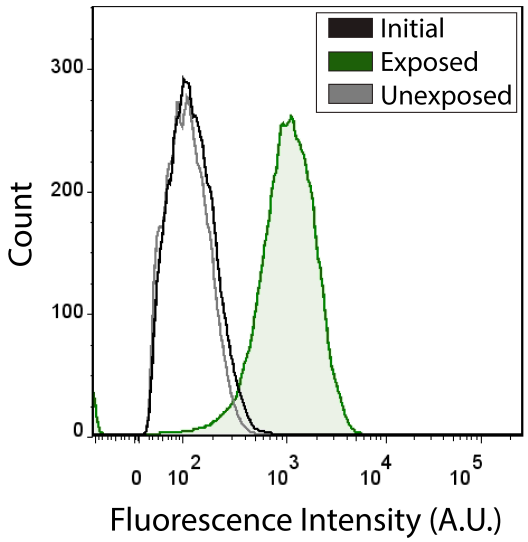

Figure 5: Flow cytometry analysis of engineered bacterial cells. Cells in JM2.300 background harboring both pCIRa and pLPTa exposed to 50 μJ/cm^2 UV irradiation. Initially, a homogenous population shows basal levels of fluorescence (black). The split population is then given or not given UV input and monitored after 6 hours with the exposed cells having a median fluorescence of 1030 A.U. and unexposed cells having a median fluorescence of 106 A.U., an approximately 10-fold increase in GFP fluorescence.

3.4 Results

3.4.1 Biosensor Transport

Biosensors are pushed in fluid using a magnetic robot (Figure 6). The sensor height should be a minimum of 5 μm so that the magnetic microrobot properly engages the edge of the biosensor for positioning. Microrobots transport 40-80 μm diameter biosensors of all sizes at speeds ranging from 0 to roughly 10 μm/s, despite the relatively significant viscous shear between the disk-shaped biosensor and the substrate. This process may be performed autonomously using visual feedback, as demonstrated in previous work [71].

3.4.2 Sensor Response

To replicate the appropriate cellular response after transferring cells between labs, as well as to characterize the UV response on the experimental apparatus used for magnetic actuation, cells were again characterized for UV exposure dose in liquid culture. The response

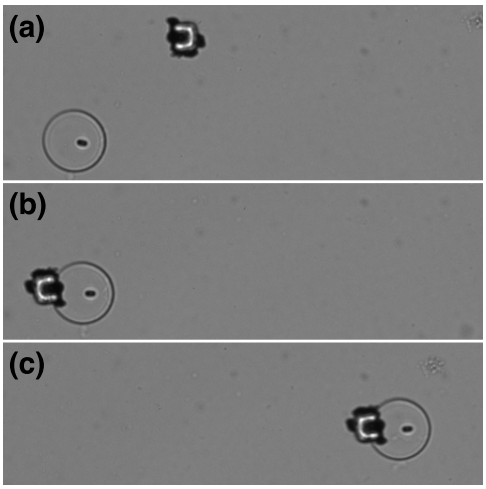

Figure 6: Transport of biosensor substrates. (a-c) An 80 μm SU8 plate is approached from the left, engaged, and transported. Biosensors are individually distributed in this fashion.

is dramatic for UV exposure times of approximately 10 s as observed using fluorescence microscopy (Figure 7). It should be noted that exposure times much greater than 10 s cause cell death, which is an expected outcome. It was not assumed that cells would respond as designed upon attachment to biosensors. The attachment of cells to substrates or to the poly-L-lysine interface was anticipated to be a potential disruption to proper operation of the designed circuit. However, the cellular response is largely preserved for the conditions of the experiment. We did find that exposure conditions were affected by experimental apparatus. Microscope optics and lab ware such as Petri dish lids act as filters at the UV wavelengths that trigger the toggle switch.

As shown in Figures 8 and 9, GFP response is strong after 12 hrs, although not all cells switch to high state, which is observed as fluorescence. Even in an unexposed population of cells, there is a small subpopulation of cells in high state. Therefore, larger sensors give a more reliable readout of UV exposure due to the larger number of attached cells. The smallest sensors only have a few high state cells for the cell densities achieved in these experiments, and it should be considered that there is a significant chance that readings from small sets of total cells (5-10) may result in incorrect determination of UV exposure.

For the integrated system, where low power toggle cells are directly attached to the microrobot, a workspace may be traversed in a matter of seconds (Figure 10). However,

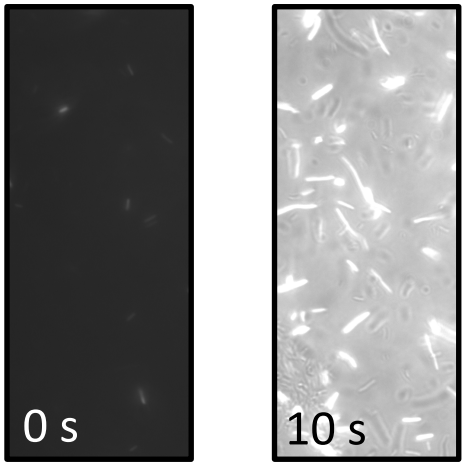

Figure 7: Low power toggle cells in low vs high states at 40× magnification. (Left) With no exposure to UV, the bulk of the population of cells stay remain in the low state (non fluorescent), however a small number of cells do express GFP. (Right) 10 s exposure to UV light induces cells to switch to high state, thus expressing GFP, but the expression of sufficient fluorescence for read out takes several hours. The high state image is taken 12 hours after exposure (induction).

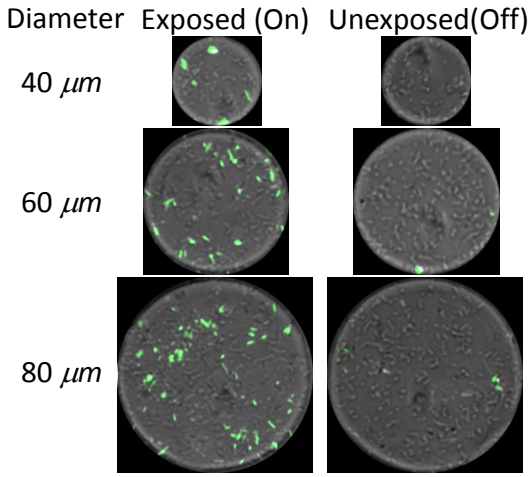

Figure 8: Sensor readout. Exposed sensors exhibit higher mean fluorescence with significantly higher numbers of cells in high state. Unexposed sensors still include a small population of fluorescing cells, which is an example of biological stochasticity. Thus, larger sensors give more reliable readout due to the higher number of cells.

expression of fluorescence takes several hours after exposure to UV light. Thus, mapping spatial location to the region of UV exposure is ambiguous, unless the robot is moved on a time scale matching readout. For the distributed system, collection and arrangement of biosensors takes minutes, and the position of the sensors are spatially correlated with UV exposure. As shown in Figure 11, distributed biosensors are collected and arranged with the

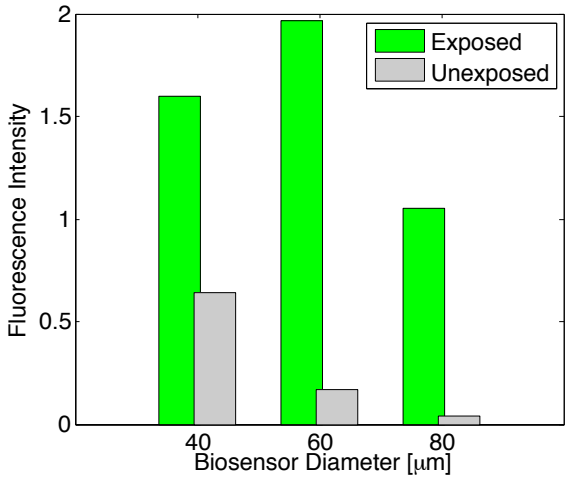

Figure 9: Mean fluorescence intensity averaged across several distributed sensor micro plates. Exposed sensors have significantly higher mean fluorescence intensity in comparison to unexposed sensors.

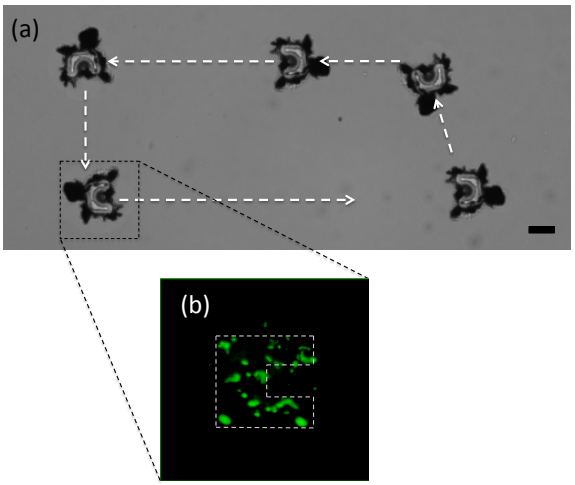

Figure 10: Integrated biosensing microrobots. (a) Magnetic microrobots are driven through a region of interest. Scale bar is 40 μm. (b) Cells attached in high state. Robot outline is indicated by dashed lines.

microrobot so that six divisions of the workspace are occupied by sensors. Current work in synthetic biology is targeted at greatly reducing the time required for readout, which would greatly enhance the practicality of these systems.

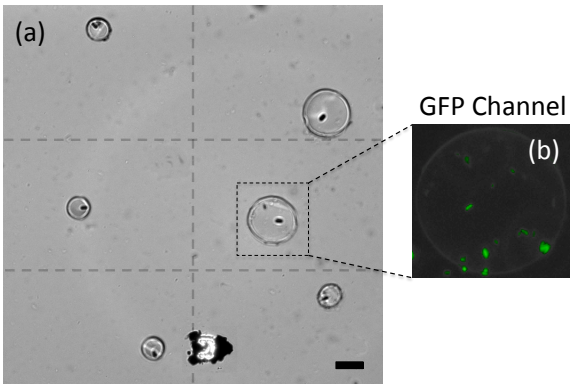

Figure 11: Distributed biosensors. (a) Six sensors are distributed to cover six division of a workspace, as delineated with dashed gray lines. (b) High state cells attached to the sampled biosensor indicate exposure to UV light. Scale bar is 40 μm.

3.5 Conclusion

In this chapter, we demonstrated the integration of microrobotic actuation techniques with engineered cells to create mobile biosensors. For this proof-of-concept prototype, we used cells that were programmed to respond to and report on exposure to UV light. This is the first time low power toggle cells have been attached as biosensors onto robots, a significant achievement that promises a pathway for transitioning research in synthetic biology to robotics. This means that cells that can serve as chemical sensors, data-loggers, or quorum sensors can also be incorporated into such systems. Thus advances in synthetic biology offer many techniques to integrate new capabilities into cells and microrobots, and provide an alternative path to microfabricating organic signal processors, power sources, and memory units.

While the results of this study are promising and suggest many exciting bridges between synthetic biology and robotics, there are several practical considerations. In most conventional robotic systems the characteristic time scales for sensing, processing and actuation are matched allowing for closed loop feedback control and motion planning. In our prototype systems, biosensors prove to be the bottleneck. The characteristic time for genetic regulation is of the order of minutes and that for cell division is of the order of tens of minutes. Whereas, as seen in Figure 11, it is clear that in the duration of a few minutes

a single robot can be used to place tens or even hundreds of sensors in targeted location enabling cell-specific measurements in samples of biological tissue. However, it will take much more time before a signal can be detected. In future work, it may be beneficial to consider other biological sensing mechanisms and reactions that have shorter reaction times that more closely match the time scales for actuation of the magnetic microrobots.

Chapter 4

Actuation Using Biology

In microscale applications such as cell manipulation, microassembly, and targeted drug delivery to cells, accurate control over a micromanipulator is important. At these length scales, having a self-powered, untethered system allows a wide range of environments to be explored, such as those that may be difficult to access. Additionally, such a system could be appropriate for in vivo applications.

This chapter explores the dynamics of microbiorobots (MBRs), which are robots constructed of a neutrally-buoyant microstructure powered by a monolayer of swarming flagellated bacteria adhered to the surface. The bacteria swim to propel the microstructure in a fluidic environment in the absence of external forces. The trajectory is a combination of translation and rotation, with the rotation generally observed to be clockwise when viewed from above.

The research in this chapter was originally published in [82, 85].

4.1 Bacteria Powered Microrobots

By attaching many of these biomolecular motors to a microstructure, the bacteria collectively cause the microstructure to move [4, 44, 67]. The work discussed in this section builds on the design of the microbiorobots (MBRs) proposed in [67]. The inherent motion of an MBR without any external forces applied has been characterized for such a system [61]. However,

this model does not take into account the hydrodynamic interaction between the flagella and the planar glass surface under the MBR. Further, the system is characterized by three unknown parameters which must be identified from experimental data.

A mathematical model is proposed for truly self-actuated microrobotic system driven by flagellated bacteria. The model considers both the propulsion force exerted by the bacteria and the non-contact, hydrodynamic surface interaction that arises from the flagella of the bacteria near the edge of the MBR interacting with the planar surface under the MBR. Experimental observations are used to validate this model.

4.1.1 Experimental Setup

A sacrificial layer of 10% dextran is first spin coated onto a glass slide, Figure 12 (a), followed by a layer of 5 μm SU-8 spin-coated on top. The SU-8 is then patterned by a photolithographic method. The slide is developed in Propylene Glycol Monomethyl Ether Acetate (PGMEA) and dried with nitrogen, Figure 12 (b). The microstructures release from the glass slide when exposed to water, Figure 12 (c). *S. marcescens* (ATCC 274) are cultured in LB broth to saturation. This culture is then used to inoculate an agar (swarm) plate (L-broth containing 0.6% Difco Bact -agar and 5 g/l glucose). Swarming begins in approximately 8 hours. The microstructures are blotted on the swarming bacteria and immediately released in a small petri dish with motility buffer (0.01 M potassium phosphate, 0.067 M sodium chloride, 10-4 M ethylenediaminetetraacetic acid (EDTA), and 0.002% Tween-20, pH 7.0) for experiments and observation.

4.2 Stochastic Kinematic Model

A stochastic kinematic model of the motion of a self-actuated MBR, e.g. actuated by the running and tumbling action of individual bacteria, is proposed by Sakar *et al.* [61]. The behavior of the bacteria are modeled as a Markov chain with two states, *run* and *tumble*, occurring at a ratio of 10 to 1 [61]. We extend this model with an added force from the interaction between the flagella of the bacteria close to the edge of the MBR interacting with the bottom surface under the MBR. 3 additional parameters are introduced in this model.

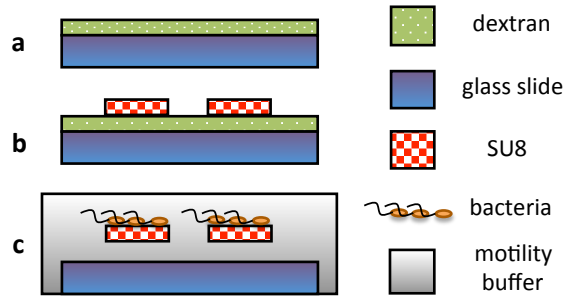

Figure 12: Microfabrication of MBRs, (a) Deposition of dextran layer onto glass slide, (b) Deposition and patterning of SU-8 on dextran, (c) Bacteria is blotted to the SU-8 microstructures and the MBRs are released using water.

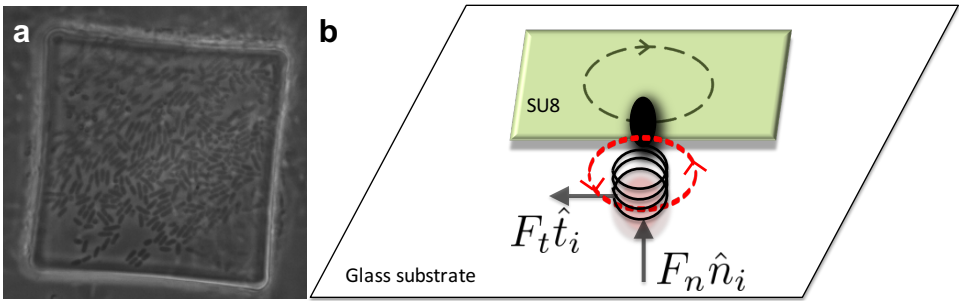

Figure 13: Image and schematics of an MBR: (a) Bacteria adhered to the surface of a 40 x 40 μm MBR (b) An oblique view from behind a bacterium extending past the edge of the SU8. Dashed ellipses with arrows indicate direction of rotation of the flagellum and MBR. Arrows $F_n\hat{n}_i$ and $F_t\hat{t}_i$ indicate the normal and tangential forces respectively. The normal force originates from the forward propulsion of the bacterium, the tangential force originates from the hydrodynamic interaction between the flagella and glass substrate when the bacterium is in the run state. The shaded region under the flagella indicates the hypothesized region of this hydrodynamic interaction. This tangential force creates a clockwise moment on the MBR which biases the rotation direction.

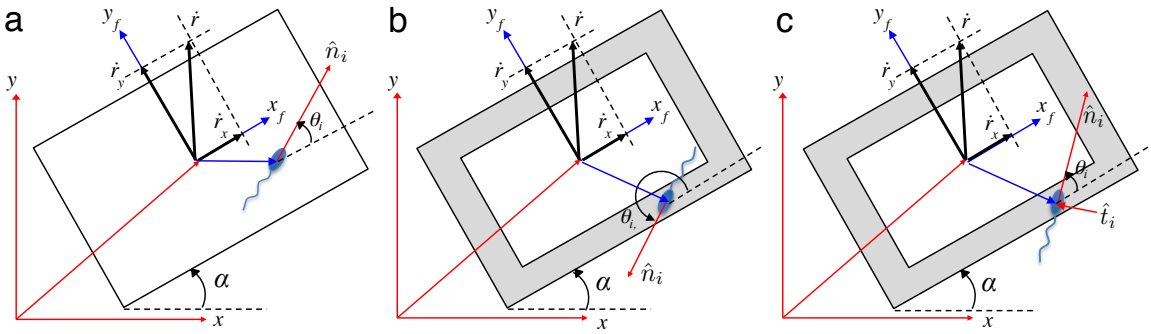

Figure 14: Forces exerted by bacteria on MBR. The shaded region indicates the region where the flagella of a bacterium may extend beyond the microstructure, (a) $N_{b,c}$: Bacterium located at center of MBR with force p_i in direction n_i, (b) $N_{b,c}$: Bacterium located close to edge of MBR and oriented such that the flagella extends into the microstructure, so exerts force p_i in direction n_i only, (c) $N_{b,e}$: Bacterium located close to edge of MBR and oriented such that the flagella extends off the microstructure, so exerts force p_i in direction n_i and q_i in direction t_i.

4.2.1 System Description

The total number of bacteria attached to the MBR, N_b, can be separated into bacteria attached in the center, $N_{b,c}$, and bacteria attached near the edge, $N_{b,e}$ which are oriented such that the flagellar bundle extends off the MBR. The force exerted (or applied) by the bacteria at the center is modeled by a propulsive force of magnitude, p_i, along the length of the body, with the direction denoted by the unit vector in the inertial frame, $\hat{n}_i$, Figure 14(a,b). The force exerted by the bacteria near the edge has the force p_i in the direction $\hat{n}_i$, similar to the bacteria at the center of the structure. These also exert an added force of magnitude, q_i, in the direction, $\hat{t}_i$, where $\hat{t}_i$ is perpendicular to $\hat{n}_i$, Figure 14(c). This is the force from the hydrodynamic interaction between the flagella and the bottom surface under the MBR [41]. The force vector exerted by each bacterium in the bacterium-fixed coordinate frame, which is rotated θ_i from the body-fixed frame (not shown in the schematic) in the center, $F_{i,c}$ and near the edge, $F_{i,e}$ are given by

$$\mathbf{F}_{i,c} = p_i \mathbf{n_i} \tag{4.1}$$

and

$$\mathbf{F}_{i,e} = p_i \mathbf{n_i} + q_i \mathbf{t_i} \tag{4.2}$$

4.2.2 Equations of Motion

With the additional tangential force component by the bacteria near the edge of the MBR, q_i, (as compared to the previous model) the equation of translational motion of the MBR is given by

$$M\frac{d^2\mathbf{r}}{dt^2} = \sum_{i=1}^{N_b} p_i \mathbf{n_i} + \sum_{i=1}^{N_{b,e}} q_i \mathbf{t_i} - k_T \frac{d\mathbf{r}}{dt}, \tag{4.3}$$

where M is the total mass of the MBR system including the bacteria and k_T is the translational viscous drag coefficient. The equation of rotational motion of the MBR is given

by

$$I\frac{d^2\alpha}{dt^2} = \sum_{i=1}^{N_b} p_i \cdot (b_{i,x}\sin\theta_i - b_{i,y}\cos\theta_i) + \sum_{i=1}^{N_{b,e}} q_i \cdot (b_{i,x}\cos\theta_i - b_{i,y}\sin\theta_i) - k_R\frac{d\alpha}{dt} \tag{4.4}$$

where $(b_{i,x}, b_{i,y})$ is the vector describing the location of the bacterium, i, from the center of the MBR in the body frame, I is the moment of inertia of the MBR and k_R is the rotational viscous drag coefficient. At low Reynolds number flows such as the system we have here, viscous effects dominate inertial forces, (e.g. $k_T >> M$ and $k_R >> I$) allowing us to eliminate the M and I terms in the equations of motion. Thus, equations (4.3) and (4.4) reduce to:

$$\frac{d\mathbf{r}}{dt} = \frac{1}{k_T}\left[\sum_{i=1}^{N_b} p_i\mathbf{n_i} + \sum_{i=1}^{N_{b,e}} q_i\mathbf{t_i}\right], \tag{4.5}$$

$$\frac{d\alpha}{dt} = \frac{1}{k_R}\sum_{i=1}^{N_b} p_i \cdot (b_{i,x}\sin\theta_i - b_{i,y}\cos\theta_i) + \frac{1}{k_R}\sum_{i=1}^{N_{b,e}} q_i \cdot (b_{i,x}\cos\theta_i - b_{i,y}\sin\theta_i). \tag{4.6}$$

From observations of the steady state behavior of *E.Coli* in the absence of external driving forces such as chemical gradients, we can make the extension that the propulsive force exerted by each bacterium is a stochastic process [6] and can be modeled as a Markov chain [12]. The frequency of the run and tumble states of the bacteria can be used to calculate the expected value of force exerted by the bacteria. Since in a tumble, the flagella unbundle and the propulsion force axial to the cell-body disappears, it is reasonable to assume that the tangential force also disappears during a tumble. By making this assumption the expected force exerted by each bacterium irrespective of the location of the bacterium can be calculated. These are expressed as $\bar{p}$ and $\bar{q}$ for the axial and tangential propulsion force for the bacterium. The expected values can be used to estimate the steady state behavior of the system as time approaches infinity, because the ratio of the standard deviation of motion to the expected value of the state of the system approaches 0 [61].

Taking equation (4.5), we can break this up into the expected motion in the $x-$ and $y-$

direction in the body-fixed frame and we can write the expected angular velocity expression,

$$\frac{dx_f}{dt} = \frac{\bar{p}}{k_T}\sum_{i=1}^{N_b}\cos\theta_i - \frac{\bar{q}}{k_T}\sum_{i=1}^{N_{b,e}}\sin\theta_i, \tag{4.7}$$

$$\frac{dy_f}{dt} = \frac{\bar{p}}{k_T}\sum_{i=1}^{N_b}\sin\theta_i + \frac{\bar{q}}{k_T}\sum_{i=1}^{N_{b,e}}\cos\theta_i, \tag{4.8}$$

$$\frac{d\alpha}{dt} = \frac{\bar{p}}{k_R}\sum_{i=1}^{N_b}\left(b_{i,x}\sin\theta_i - b_{i,y}\cos\theta_i\right) + \frac{\bar{q}}{k_R}\sum_{i=1}^{N_{b,e}}\left(b_{i,x}\cos\theta_i - b_{i,y}\sin\theta_i\right). \tag{4.9}$$

From these equations (4.7-4.9), 6 parameters that characterize the dynamics of the system can be identified:

$$\beta_1 := \frac{1}{k_T}\sum_{i=1}^{N_b}\cos\theta_i, \qquad \beta_2 := \frac{1}{k_T}\sum_{i=1}^{N_b}\sin\theta_i, \qquad \beta_3 := \frac{1}{k_R}\sum_{i=1}^{N_b}\left(b_{i,x}\sin\theta_i - b_{i,y}\cos\theta_i\right).$$
$$\gamma_1 := -\frac{1}{k_T}\sum_{i=1}^{N_{b,e}}\sin\theta_i, \qquad \gamma_2 := \frac{1}{k_T}\sum_{i=1}^{N_{b,e}}\cos\theta_i, \qquad \gamma_3 := \frac{1}{k_R}\sum_{i=1}^{N_{b,e}}\left(b_{i,x}\cos\theta_i - b_{i,y}\sin\theta_i\right).$$

These parameters are dependent on the geometry as well as the distribution of bacteria on the MBR. It is clear that γ_1 is a (negative) fraction of β_2, since the summation for γ_1 is the fraction of bacteria that are near the edge of the MBR. Similarly, γ_2 is a fraction of β_1. The relationship between β and γ are also geometry- and bacteria-distribution dependent and will vary case by case.

Using these parameters, the expectant motion in the inertial frame is given by

$$\frac{dx}{dt} = (\bar{p}\beta_1 + \bar{q}\gamma_1)\cos\alpha - (\bar{p}\beta_2 + \bar{q}\gamma_2)\sin\alpha, \tag{4.10}$$
$$\frac{dy}{dt} = (\bar{p}\beta_1 + \bar{q}\gamma_1)\sin\alpha + (\bar{p}\beta_2 + \bar{q}\gamma_2)\cos\alpha, \tag{4.11}$$
$$\frac{d\alpha}{dt} = \bar{p}\beta_3 + \bar{q}\gamma_3 \tag{4.12}$$

From experimental data for 80μm square MBRs, the magnitude of the system parameters for $\beta_{1,2}$ and $\gamma_{1,2}$ are on the order of 10s of μm/(s pN) and β_3 and γ_3 are on the order of 1

rad/(s pN). This model can be fit to experimental data and the parameters $\beta_{1,2,3}$, and $\gamma_{1,2,3}$ can be determined by observing the motion of the MBR.

4.3 Orientation Experiment

The first experiment conducted to probe the dynamics of the system involved using microstructures that had an asymmetric marking, the letter *F*, on them to determine the orientation of the MBRs. MBRs settle near the bottom of the observation chamber in one of two possible orientations. Either the bacteria are on the top of the SU-8 (*bacteria up*), or bacteria are on the bottom of the SU-8, such that the bacteria are close to the surface (*bacteria down*).

Microstructures of 40μm squares with a letter *F* etched out of them were used. The microstuctures are oriented during fabrication such that when viewed from above, the *F* is not inverted and the MBRs are *bacteria up*, whereas when the F is inverted, the MBRs are *bacteria down*. This orientation convention is ensured because the SU8 microstructures are attached to the glass slide when blotted on the bacteria and do not release from the slide until the glass slide with the MBRs are placed in the experimental chamber. For this experiment, in order to increase the number of MBRs that are *bacteria down*, the slide is inverted and shaken in the experimental chamber such that there is a distribution of up/down orientations.

4.3.1 Results

The rotation direction of 37 square MBRs, each with 40μm sides, were observed. Since the rotation rate varies greatly between different MBRs, a threshold of π radians per 60 seconds is used to determine whether an MBR is considered to be rotating. MBRs that have rotations under this threshold (i.e. not rotating as defined by this metric) have been ignored for this study. This threshold was chosen to eliminate MBRs that were not rotating or rotating very slowly. If a threshold less than π were used, the results would qualitiatively be the same.

Figure 15 shows a histogram of these results, while both the *bacteria up* and *bacteria*

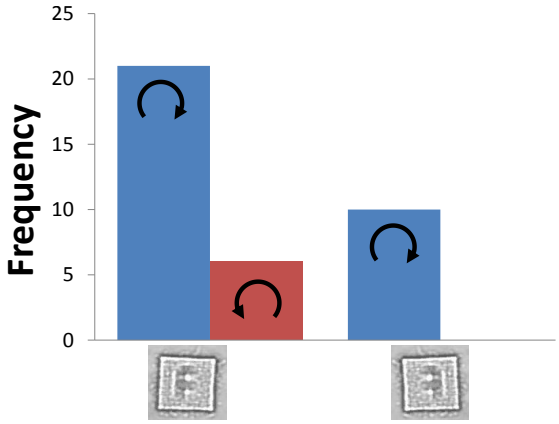

Figure 15: Histogram of rotation direction of 40 μm square MBRs characterized by whether the structures are *bacteria up*(left) or *bacteria down* (right). Results show the MBRs are have a tendency to rotate in the clockwise direction.

down MBRs can rotate clockwise (CW) and counter clockwise (CCW), the overall tendency irrespective of orientation is for the MBRs to rotate CW. The distribution in rotation direction and rate can be attributed to stochasticity in the system. This could be from the orientation and distribution of the bacteria or the randomness associated with the behavior of the bacteria. These results support the hypothesis that rotation of the MBRs is in part driven by a force tangential to the cell body that arises from the interaction between the glass slide on the bottom surface of the experimental chamber and the flagella of the bacteria close to the edge of the MBR; since the orientation will not affect the direction in which this tangential force is exerted. Additionally, this study also suggests that when the MBRs are released using the method of placing the glass slide on the bottom of the experimental chamber (without shaking upside down) the majority of MBRs will remain in the *bacteria up* orientation.

4.4 Edge Effect

To probe the effect of cell location on the MBR and the force exerted, we utilize the response of *S. Marcescens* to UV light to selectively immobilize the bacteria in localized regions of the MBR [67]. In all experiments, a square geometry for the MBR is used. A symmetric shape was chosen to negate any resultant moment that may be caused by randomly swimming

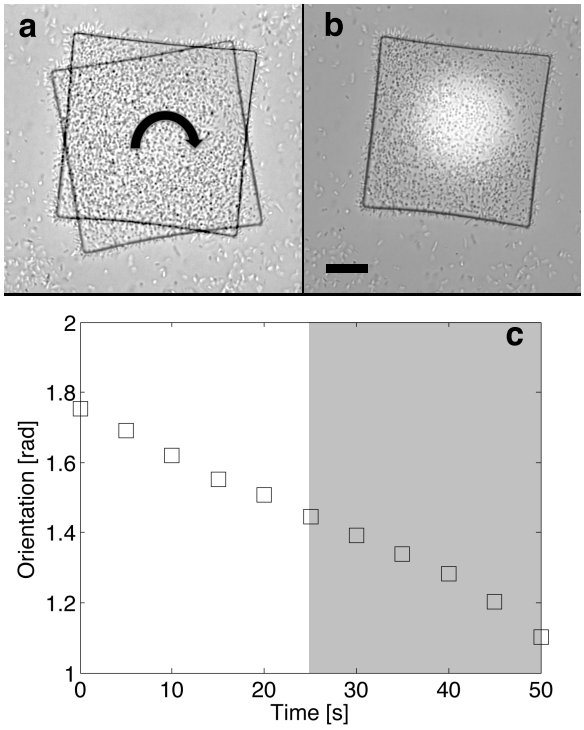

Figure 16: UV exposure to the center of a 80 × 80 μm square MBR: (a) Rotation direction of the MBR before UV exposure, (b) Location of UV exposure, (c) Orientation angle as a function of time for Table I. experiment (a), greyed out section indicates UV exposure. Angular velocity is approximately constant and independent of UV exposure. Scale bar is 20 μm.

bacteria in solution colliding with the structure [65].

To isolate the force contributions of bacteria adhered onto different parts of the MBR, *S.marcescens* are immobilized at localized regions on the MBR by selectively exposing the MBR to near-UV light. A DAPI (4',6-diamidino-2-phenylindole) filter and constricted iris aperture are used to create a circular spotlight of near-UV light with a diameter of 40 μm at 40X magnification. The microscope stage is moved to expose different areas of the MBR to the spotlight. Since the stage must be moved continually to direct the light on the desired part of the MBR, only data on the rotation and not the translation of the system are tracked.

4.4.1 Results

Square microstructures of 60 and 80 μm with a thickness of 2 μm were used for this experiment. The SU-8 photosensitive epoxy fluoresces under these wavelengths, and enables the

Table 1: MBR center exposure to near-UV light experiment.

	Angular Velocity (rad/sec)[a]		Change[b]
	Before UV	During UV	(%)
(a)	-0.012	-0.013	8.8
(b)	-0.009	-0.011	23.3
(c)	-0.011	-0.014	21.8
(d)	-0.018	-0.019	9.5
(e)	-0.008	-0.007	-9.3

[a] Fits measured data with at least a coefficient of determination of 0.98.

[b] Percent change before, ω_1, and during, ω_2, UV exposure, $\Delta\% = \frac{\omega_2 - \omega_1}{\omega_1}$.

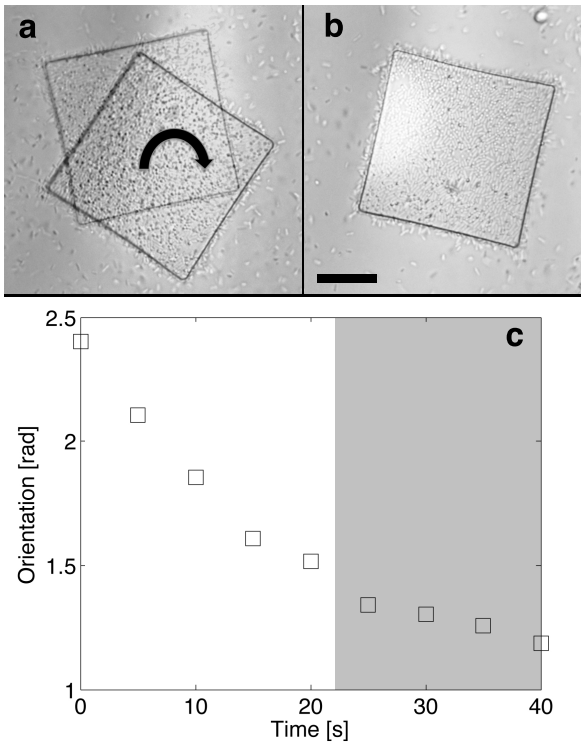

Figure 17: UV exposure to the corner of a 60 × 60 μm square MBR: (a) Rotation direction of the MBR before UV exposure, (b) Location of UV exposure, (c) Orientation angle as a function of time for Table II. experiment (a), greyed out section indicates UV exposure. Angular velocity is reduced after edge exposure. Scale bar is 20 μm.

Table 2: MBR edge exposure to near-UV light experiment.

	Angular Velocity (rad/sec)[c]		Change[b]
	Before UV	During UV	(%)
(a)	-0.045	-0.010	-77.5
(b)	-0.057	-0.029	-48.3
(c)	-0.048	-0.030	-36.8
(d)	-0.137	-0.094	-31.4
(e)	-0.027	-0.020	-26.2

[c] Fits measured data with at least a coefficient of determination of 0.95.

region where the bacteria were immobilized to be identified visually, Figure 16(b). Two different cases were tested to isolate and compare the contribution to the MBR motion. Firstly, the bacteria at the center of the microstructure were immobilized. In the second case, bacteria at the edge of the microstructure were immobilized. A time series plot of orientation angle is shown in Figure 16(c) and 17(c) to illustrate how immobilizing the bacteria on different regions of the MBR affects its angular velocity. Results from 5 different experiments for each case are reported in Table 3 and 2 for the two cases respectively.

When bacteria in the center of an MBR are exposed and the bacteria in this region are immobilized, only the bacteria on the edges are contributing to the angular velocity of the MBR. Observations show that small changes in angular velocity are detected when the center of the UV light is exposed (compared to angular velocity changes for the edge exposure cases,) as shown in Figure 16(c) and Table I. This effect supports the hypothesis that there is a near-wall hydrodynamic interaction between the flagella of the bacteria near the edge of the MBR and the bottom surface under the MBR which in turn results in a moment [41] causing the MBR to rotate.

When bacteria on one edge of an MBR are exposed, the angular velocity of the MBR decreases, as shown in Figure 17(c) and Table II. This suggests that fewer bacteria are exerting a tangential force on the edge contributing to the moment about the axis of rotation perpendicular to the plane, therefore resulting in a decrease in angular velocity after near-UV light exposure to the edge.

In a case where the bacteria in the center of the MBR are uniformly and randomly

distributed, the expected resultant moment contribution from these bacteria is 0. In practice, there is a resultant moment contribution by the center bacteria, but the magnitude is small compared to the contribution by the bacteria near the edge of the MBR as a result of the longer moment arm. This variation in bacteria distribution explains why the percentage change in angular velocity before and during near-UV light exposure to the center of the MBR varies between -9.3 and 23.3%.

4.5 Actuation By Active Suspension

Related works have shown that an active suspension, such as free-swimming bacteria in solution, can produce a biased rotation of microstructures. This motion is produced by stochastic collisions of bacteria with walls of asymmetric microstructure geometries, such as micro-gears [65], [19]. Previously demonstrated in a thin fluid film of free-swimming bacteria, asymmetric gear rotation has been observed primarily in the direction of the slanted edges of the gear teeth. This behavior has been explained from the observation of bacteria packing at the corners of gear teeth, in turn producing a moment acting on the microstructure [65]. In the current experiment, the effect of microstructure geometry on MBR motility is characterized. Specifically, two modes of interaction between bacteria and microstructure geometric features were examined: (1) propulsion resulting from bacteria adhered directly to the microstructure surface (Figure 18(a)) and (2) collisions between swimming bacteria in solution and the microstructure out-of-plane walls (Figure 18(b)). Each interaction mode was examined using asymmetric micro-gears of opposing gear tooth orientations, which measured approximately 10 μm in thickness and 70 μm across tip-to-tip of the gear teeth.

Microstructures were fabricated by spin coating a layer of 10 % dextran onto a glass slide followed by a layer of negative SU-8 negative photoresist. The layer of SU-8 was patterned via standard photolithographic methods, and subsequently developed with Propylene Glycol Monomethyl Ether Acetate (PGMEA) and dried with nitrogen. Serratia marcescens ATCC 274 (American Type Culture Collection, Manasas, VA) was cultured using a swarm plate technique (LB broth containing 0.6 % Difco Bacto-agar and 5 g/L glucose). An agar plate

was inoculated with approximately 2 μL of *S. Marcescens* saturated culture and swarming began in approximately 8 hours.

4.5.1 Results

The rotation direction was observed for 66 asymmetric micro-gears blotted with bacteria Figure 18c. Counterclockwise or clockwise rotation was observed for micro-gears independent of the tooth chirality. The distribution in rotation direction may be attributed to stochasticity in the system, such as orientation and dispersal of bacteria on the microstructure surface. However, the overall tendency is for blotted MBRs to rotate clockwise. The primary clockwise rotation direction may be supported by the near-wall swimming behavior of bacteria.

The effect of collisions between free-swimming bacteria and the microstructure walls is best observed by introducing an excess amount of surfactant to the motility solution. By weakening the surface energy between the cell body and the microstructure surface, bacteria were prevented from adhering. Collisions between swimming bacteria in the solution and walls of the structure created a net tangential force to rotate the MBR in a manner defined by the asymmetries of the microstructure. In this case, when no bacteria are adhered to the microstructures, all micro-gears possessing teeth of counterclockwise chirality, Figure 18(b)(i), were observed to rotate clockwise. Conversely, all micro-gears possessing clockwise oriented teeth, Figure 18(b)(ii), were observed to rotate counterclockwise. While this behavior has been observed previously in a thin-film suspension [19, 65], our experiments demonstrate that this effect of geometric microstructure asymmetries also pertains to MBR motility near a wall. Previous discussions on these collisions have implicated a bacterial packing effect which occurs at the corners of micro-gear teeth [65]. The experiments performed in this work suggest a different mechanism by which torque is generated to rotate these micro-gears. Bacteria in solution swim along the micro-gear slanted edges and instantaneously collide with the flat edge of the tooth, which applies a moment to the structure.

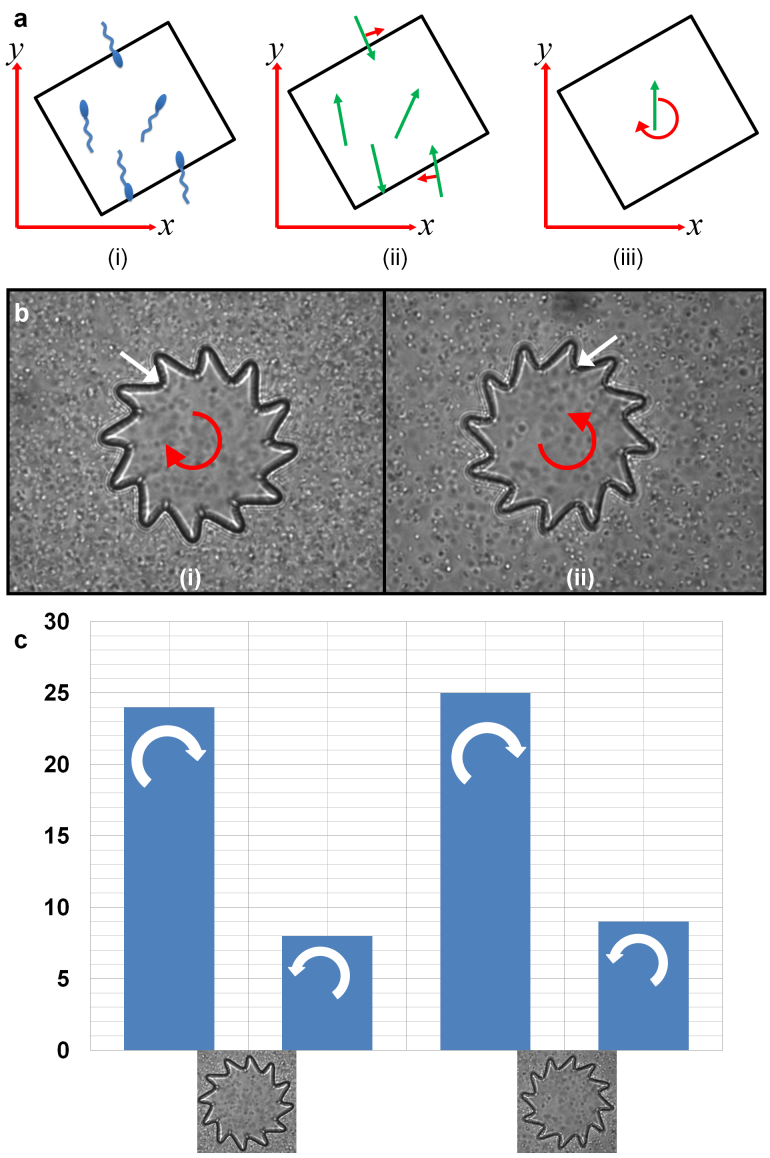

Figure 18: (a)Schematic of MBR showing propulsion forces from adhered bacteria. (i) Sample distribution of blotted bacteria on microstructure. (ii) Propulsive forces resulting from adhered bacteria. (iii) Resultant clockwise moment and some arbitrary force. (b)Collisions between swimming bacteria in solution and gears without adhered bacteria to the gears.(i) 100% clockwise rotation direction observed for micro-gears exhibiting counterclockwise oriented teeth.(ii) 100% counterclockwise rotation direction observed for micro-gears exhibiting clockwise oriented teeth. (c) Observed rotation direction for micro-gears propelled by adhered bacteria. Results indicate blotted MBRs have a tendency to rotate in the clockwise direction, despite gear tooth asymmetry and orientation.

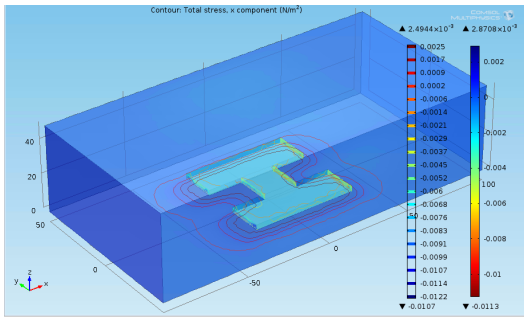

Figure 19: Total stress profile of a translating H-shaped MBR moving at a velocity of 10μm/s.

4.6 Modeling Fluid Drag on an MBR

To investigate the forces required to actuate an MBR, a hydrodynamic simulation to approximate microstructure motility was developed. Many bacteria collectively swim to propel a microstructure throughout a fluidic environment. While it would be very difficult to experimentally measure critical hydrodynamic parameters including shear stress and viscous drag force, these may be computed via numerical methods. We use the computed force required to rotate an MBR at a given angular velocity to estimate the collective force of bacteria acting along the MBR edge as well as to determine the coefficients for translational and rotational drag.

To approximate the hydrodynamic force required for *translational* motion of an MBR, we can prescribe the exact geometry of the microstructure and compute values using a moving wall model. Approximation of the hydrodynamic drag force on a translating MBR has been previously described [74]. For a translating H-shaped microstructure moving at a velocity of 10μm/s, the total drag force is 15 pN (Figure 19).

To approximate the hydrodynamic forces acting in the *rotational* frame, a disk-shaped geometry is used due to computational modeling restrictions (Figure 20). The following was assumed for the calculation of viscous drag on the plate:

1. Laminar flow
2. Incompressible flow,
3. Steady-state flow

4. Pure tangential velocity, $V_r = V_z = 0$
5. Constant density, ρ
6. Constant viscosity, μ

Using these assumptions, hydrodynamic forces acting on the plate may be derived from first principles. Beginning with the continuity equation in 3-dimensional polar coordinates:

$$\frac{\partial \rho}{\partial t} + \frac{1}{r}\frac{\partial}{\partial r}(\rho r V_r) + \frac{1}{r}\frac{\partial}{\partial \theta}(\rho V_\theta) + \frac{\partial}{\partial z}(\rho V_z) = 0 \tag{4.13}$$

where V_r, V_θ, and V_z are the velocities of the fluid in the r-, θ-, and z- coordinate respectively. From the assumption for a Newtonian fluid, we can assume that the fluid velocity is axisymmetric:

$$\frac{\partial V_\theta}{\partial \theta} = 0 \tag{4.14}$$

The Navier-Stokes equation of motion simplifies to the following in the r-component, θ-component and z-component, respectively.

$$-\rho\frac{V_\theta^2}{r} = -\frac{\partial \rho}{\partial r} \tag{4.15}$$

$$\mu\frac{\partial^2 V_\theta}{\partial z^2} = 0 \tag{4.16}$$

$$\frac{\partial \rho}{\partial z} = 0 \tag{4.17}$$

Using COMSOL Multiphysics Simulator for numerical analysis, the Navier-Stokes equations of fluid motion were simultaneously solved for velocity and viscous drag force on a rotating plate. The parameters were solved for a 2-dimensional axisymmetric geometric model in Stokes' flow (low Reynolds number). A rotational velocity was prescribed about the disk axis at its center, as well as appropriate moving wall boundary conditions on the disk edges. Results of the simulation show the disk rotating at an angular velocity symmetric about its axis. As expected, the angular velocity increases in magnitude from its center to the edge, where the velocity is maximum, this is illustrated qualitatively by the

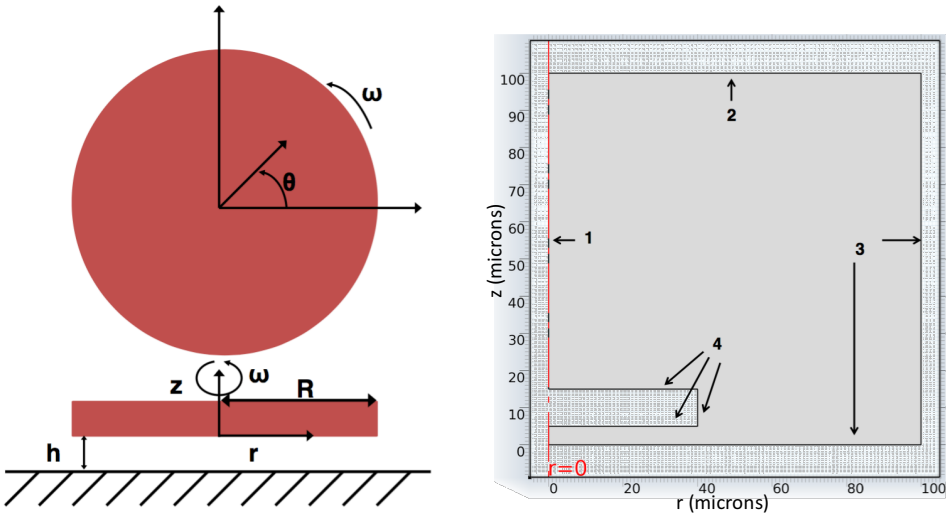

(a) (b)

Figure 20: Computational fluid dynamic model parameters for an MBR. (a) Parallel-plate rheometer model of an MBR. Rotation at a prescribed angular velocity of ω of a circular plate in polar coordinates (b) Prescribed boundary conditions of a 2-dimensional axisymmetric geometry for numerical simulation as follows, 1:Axial Symmetry, 2:Symmetry, 3: No-slip, 4: Moving wall at prescribed angular velocity.

red color indicating the greatest stress in Figure 21(a). Additionally, the stress distribution over the disk surface is as expected. Stress, in the angular direction, is greatest at the interface between the bottom surface of the disk and the planar surface of the fluid container 21(b,c). Integrating total stress in the angular direction over the disk radius, and again over the entire disk surface yields the viscous drag force. For a circular disk of radius 36.5 μm and thickness 10 μm rotating at an angular velocity of 10 deg/s at a distance 5 μm between the bottom surface of the MBR and the stationary planar glass slide, the magnitude of the total force exerted at the edge of the disk is 0.329 pN. Limitations pertaining to rotational modeling prevented the shapes used in experiments to be simulated. However, the results obtained for a circular disk may be applied to microstructures of other shapes.

4.7 Chemotactic Bottom-up Model

To capture the stochasticity of the MBR motion, a bottom-up model is developed that incorporates the distribution of bacteria, models the bio-molecular network governing the bacteria flagellar motor to capture the stochastic switching between run and tumble state of

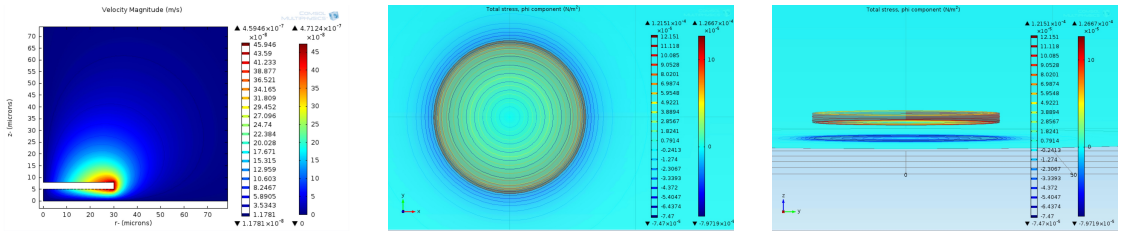

(a) (b) (c)

Figure 21: MBR hydrodynamic model results. (a) 2-dimensional axisymmetric velocity magnitude of a rotating MBR at a prescribed angular velocity of 10 deg/s. (b) Total stress profile projection in the x-y plane of a rotating MBR at a prescribed angular velocity of 10 deg/s. Stresses are radially symmetric. (c) Total stress profile projection in the y-z plane of a rotating MBR. Stresses are greatest at the disk edge and interface between the bottom surface of the disk and planar surface below. Where red indicates the greatest velocity and stress in the respective figures.

each bacterium and carries out a force balance for the entire system. A simplified chemotaxis model is used to simulate the run and tumble behavior of cells. Preliminary simulation results validated by experimentally observed clockwise angular velocity bias are shown.

From observations of the steady state behavior of *E.Coli* in the absence of external driving forces such as chemical gradients, we can make the extension that the propulsive force exerted by each bacterium is a stochastic process [6]. This process can be modeled in each cell using a Gillespie algorithm [29]. Assuming that cells do not interact with one another, an independent Gillespie algorithm is used to predict the state, run or tumble, of each cell attached to an MBR. By using a Gillespie algorithm, each generated trajectory will be unique as a different combination of run-tumble sequences will emerge. The result will be one possible trajectory for the MBR, by running many trials for the same system it is possible to obtain a distribution of trajectories.

To model the stochasticity of the flagella, a simplified chemical model of the chemotaxis network in *E.coli* is used. Since the specific interest is in the flagellum behavior in steady-state in the absence of chemical attractants, a simplified model is used which involves kinases CheA and protein CheY and the state of the flagella, equations 4.18 - 4.22, a specific rate of reaction denoted by the Greek letters, $\alpha, \beta, \gamma, \mu, \rho$, governs the rate of each equation.

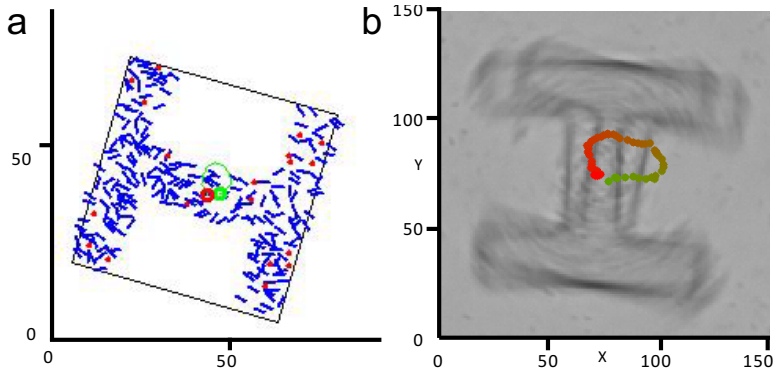

Figure 22: Preliminary modeling results for a predominantly rotating MBR, trajectory starts at green and ends at red. (a) Simulation trajectory, (b) Experimental trajectory.

$$CheA \xrightarrow{\alpha} CheA - p \tag{4.18}$$

$$CheA - p + CheY \xrightarrow{\beta} CheY - p + CheA \tag{4.19}$$

$$CheY - p \xrightarrow{\gamma} CheY \tag{4.20}$$

$$Tumble \xrightarrow{\mu} Run \tag{4.21}$$

$$CheY - p + Run \xrightarrow{\rho} CheY - p + Tumble \tag{4.22}$$

Equation 4.18 expresses the phosphorelation of kinases CheA to CheAp. The phosphoryl groups are not explicitly expressed (aside from when attached to a protein) or tracked in simulation as an abundance of them are assumed in the cell and therefore this is not a rate determinant chemical.

Equation 4.19 expresses the transfer of the phosphoryl group from CheA to CheY.

Equation 4.20 expresses the dephosphorelation of CheY. While CheZ is typically associated with this reaction, since CheZ does not change during this reaction and is not involved in other reactions in the model, its effect is encapsulated in the reaction rate γ.

Equation 4.21 expresses the transition of the flagellum from a run to a tumble state. The interaction of CheYp with the motor increases the probability of a tumble behavior, this relationship is created by including CheYp as a reactant and product in this reaction. Since

the state Run can only be 0 or 1, by setting the steady state of CheYp to be 1, when the level of CheYp drops the rate of tumbling will also decrease.

Equation 4.22 expresses the transition from tumble to run state. The rate of this reaction is unaffected by the levels of the chemicals in the cell. The state of CheA and CheY are enough to model the state of the cell because the motor behavior is directly dependent on its interaction with CheY; moreover, the phosphorelation state of CheY depends on CheA. CheZ, CheW, CheB and CheR are omitted as well as methylation reactions even though they are involved in the chemotaxis network. This is done to maintain simplicity of the model and because response to chemical stimuli are not considered here.

In this model, CheW, CheB and CheR are omitted as well as methylation reactions even though they are involved in the chemotaxis network. This is done to maintain simplicity of the model. CheB and CheR are omitted as they are components involved in the adaptation of receptor sensitivity to chemical concentration, which is not explicitly modeled in this system.

To validate the simulation, a free solution - no chemo-attractants or chemo-repellents, was simulated and compared to experimentally observed data. The following parameters were used for the single cell simulation, reaction rates:

α	β	γ	μ	ρ
0.11	1×10^{8}	0.031	10	1

Initial conditions:

Receptor	CheA	CheAp	CheY	CheYp	Flagella
I	0	0	1	1	Run

1000 simulations were run for 400 seconds. The trajectories generated show that direction of travel is equally likely in all directions. Additionally, the run to tumble ratio is 10 to 1, as shown experimentally [27]. These results help validate the simulation and it is consistent with experimentally observed cell behavior in free solution.

The rates of reaction α, β and γ were determined based on averages found in literature [9]. The rates for transition between run and tumble state were chosen so that the run and

tumble ratio would be 10 to 1, and the exponential distribution of rates is inherit in the Gillespie simulation. This ratio implies that the $\frac{\mu}{\rho}$ would have to be 10 in addition to the steady-state value of CheYp being 1. This is because the reaction from run to tumble is also a function of the concentration of CheYp; therefore, to maintain the run and tumble ratio, the steady-state value of CheYp must be 1 (alternatively the rate ρ could be scaled accordingly.)

For the simulation of an MBR, n-parrallel Gillespie simulations are run for n-cells attached to the MBR. At each successive reaction time, the equations of motion are updated and trajectory computed. The complexity of the simulation therefore increases linearly with the number of cells to run a simulation for the same duration.

4.7.1 Preliminary Results

Figure 22 shows similar trajectories between experiment and simulation, however the orientation does not match well. This suggests that there may be additional factors affecting the motion of the MBR not captured in this model. This may include the forces from bacteria running into the sides of the MBR and forces exerted on the MBR while the cell is in a tumble.

4.8 Conclusion

In this chapter, we propose two models, first, a top-down stochastic kinematic model, which informs the second, a bottom-up chemotactic model. The top-down stochastic kinematic model is able to capture the biased clockwise rotation of microbiorobots propelled by flagellated bacteria which are adhered to the surface of the robot. The model is validated in three different experiments to determine the force exerted by the bacteria attached at different locations on the microbiorobot. The force contribution by free-swimming bacteria in solution colliding with the sides of the microbiorobot is investigated by observing the dynamics of micro structures powered by an active suspension of bacteria in the solution surrounding the microstructure compared to microbiorobots powered by bacteria attached to the microstructure. The bottom-up model of bacteria propelled microstructures captures the

stochasticity of cell behavior. This chapter makes contributions towards steering bacteria propelled microbiorobots using external stimuli.

Chapter 5

Actuation using Magnetic Fields

The microrobots propelled by biological organisms, discussed in Chapter 4, have the benefit of onboard power in a small package; however, they are difficult to control because of the inherent stochasticity of biological organisms. Another method of actuating microrobots is embedding magnetic particles into the microstructures and using magnetic fields to actuate the robots. Magnetic manipulation enables more deterministic control and have been proposed for applications in various procedures in minimally invasive surgery and in vitro cell manipulation in biological experiments [40, 47, 70]. High-resolution manipulation is important in microrobotics, micro surgery, biosciences, micro materials, micro manufacturing and soft matter.

This chapter discusses the use of magnetic fields for manipulation of magnetic robots. An analytical solution to compute the magnetic field generated by a current carrying loop is presented using the Biot-Savart law. This is also used to calculate the force exerted on a magnet in the field. We discuss the empirical characterization of a magnetic manipulation system that consists of 4 stationary electromagnetic coils used to manipulate a magnetic robot made of permanent magnetic material pinned on an oil-water interface.

5.1 Magnetics Background

Nomenclature

For clarity and convenience, the following table lists the nomenclature and the SI units for each variable. These assignments are used throughout the thesis in the discussion of magnetically actuated robots.

An arrow above a variable signifies a vector with direction and magnitude; without the arrow signifies a scalar. A tilde above a variable signifies that it is non-dimensionalized. A hat signifies a unit vector. A capitol letter in boldface indicates a matrix.

I_i	Current through coil i	A
R_i	Radius of coil i	m
L_i	Position of coil i measured from origin	m
$\vec{m}_j$	Magnetic poles of permanent magnet j	Am
$\vec{\mu}_j$	Magnetic dipole moment for magnet j	Am^2
$\vec{x}_j$	Position of magnet j measured from origin	m
$\vec{F}_j$	Force acting on magnet j	N
$\vec{B}$	Magnetic field	T
$\vec{r}$	Vector between two permanent magnets	m
μ_0	Permeability constant for air, $4\pi \times 10^{-7}$	Tm/A

Magnetic Field

The magnetic field generated by a current loop can be derived by the Biot-Savart equation:

$$\vec{B}_{loop} = \frac{\mu_0 I}{4\pi} \int_C \frac{d\vec{s} \times \hat{l}}{|l|^2} \tag{5.1}$$

where I is the current, μ_0 is the permeability constant for air, $\hat{l}$ is the unit vector from the coil wire segment to the point of interest, and a closed loop integral is taken around the entire current loop, C, for each segment ds.

The magnetic field for the xy-plane at z=0 is computed using the Biot-Savart equation (5.1) for a circular loop with radius R centered at [0,0] with the face of the loop in the yz-plane and the axis of the coil aligned along the x-axis [5],

$$\vec{B} = B_x\hat{i} + B_y\hat{j}$$

$$B_x = \frac{\mu_0 IR}{4\pi}\int_0^{2\pi} \frac{R - ysin\phi'}{\left(R^2+y^2+x^2-2yRsin\phi'\right)^{3/2}}d\phi' \tag{5.2}$$

$$B_y = \frac{\mu_0 IRx}{4\pi}\int_0^{2\pi} \frac{sin\phi'}{\left(R^2+y^2+x^2-2yRsin\phi'\right)^{3/2}}d\phi' \tag{5.3}$$

where ϕ' is the variable of integration around the circular coil and is integrated around the full circle from 0 to 2π. This is summed over each coil. The solution of these integrals can be written in terms of incomplete elliptic integrals,

$$\begin{aligned} B_x = {} & \frac{\mu_0 I}{2\pi}\frac{1}{\sqrt{(R+|y|^2)+x^2}} \\ & \left[\mathcal{F}(\frac{\pi}{2},k^2) + \frac{R^2-y^2-x^2}{(R-|y|)^2+x^2)}\mathcal{E}(\frac{\pi}{2},k^2)\right] \end{aligned} \tag{5.4}$$

$$\begin{aligned} B_y = {} & \frac{IR\mu_0 x}{4\pi}\sqrt{\frac{\alpha}{(R-y)^2+x^2}}\left\{\frac{1}{Ry\sqrt{\alpha}\,(\alpha+2Ry)}\right. \\ & \left[\alpha\left(\mathcal{E}\left(\frac{\pi}{4},n^2\right)+\mathcal{E}\left(\frac{3\pi}{4},n^2\right)\right)\right. \\ & \left.\left.-(\alpha+2Ry)\left(\mathcal{F}\left(\frac{\pi}{4},n^2\right)+\mathcal{F}\left(\frac{3\pi}{4},n^2\right)\right)\right]\right\} \end{aligned} \tag{5.5}$$

where $\alpha = R^2+y^2+x^2$, $k^2 = \frac{4R|y|}{(R+|y|)^2+x^2}$ and $n^2 = \frac{-4Ry}{R^2-2Ry+y^2+x^2}$ in the incomplete elliptic integrals of the first and second kind, respectively, $\mathcal{F}$ and $\mathcal{E}$. The elliptic integral of the first kind, $\mathcal{F}$, and of the second kind, $\mathcal{E}$, are given by,

$$\mathcal{F}(\phi,p^2) = \int_0^{\phi}\frac{1}{\sqrt{1-p^2\sin^2\phi}}d\phi \tag{5.6}$$

$$\mathcal{E}(\phi, p^2) = \int_0^{\phi} \sqrt{1 - p^2 \sin^2 \phi} d\phi \tag{5.7}$$

These expressions are used to compute the force and torque exerted on a magnet.

Force

A force is exerted on a ferromagnetic particle with a magnetic dipole moment, $\vec{m}$, when in the presence of a magnetic field, $\vec{B}$. This force, $\vec{F}$, is calculated by,

$$\vec{F} = (\vec{m} \cdot \nabla) \vec{B} \tag{5.8}$$

The value for the magnetic dipole moment of the permanent magnet, $\vec{m}$, depends on material properties and geometry of the magnet.

Torque

The magnetic torque, $\vec{\tau}$, is calculated by,

$$\vec{\tau} = \vec{m} \times \vec{B} \tag{5.9}$$

The torque acts to align the dipole of the robot with the field, $\vec{B}$. In this model, we assume that this reorientation occurs immediately for the robot, which is a permanent magnet, and the robot is always torque free [1, 46]. The magnetic dipole moment, $\vec{m}$, is therefore expressed as:

$$\vec{m} = \frac{|m|}{|B(x,y)|}(B_x(x,y)\hat{i} + B_y(x,y)\hat{j}) \tag{5.10}$$

This is used with equation (5.8) and the expressions for the magnetic field to compute the force exerted on the magnet.

Magnet-Magnet Interaction

Using Coulomb's law for magnetic poles, which assumes that the magnetic poles are small enough to be assumed a point, the force, F_j exerted on magnet j separated from magnet k

by a vector $\vec{r}$ is given by,

$$\vec{F}_j = \frac{\mu_0 m_j m_k}{4\pi |r|^2} \hat{r} \tag{5.11}$$

The value for the magnitude of the magnetic poles of the permanent magnet, m_j and m_k, depend on material properties and geometry of the magnet and is derived empirically in the Section 6.1.1. While Coulomb's model is an approximation, the accuracy of the model improves as distance between magnets increase and is relevant for our application.

5.2 Magnetic System Characterization

To achieve high-resolution micromanipulation of a magnetic robot, it is important to characterize the system to generate an accurate model to map system inputs to robot behavior. This section discusses the system characterization of a magnetic manipulation system that consists of 4 stationary electromagnetic coils which is used to manipulate a magnetic robot made of permanent magnetic material pinned on an oil-water interface. The characterization of the system can be divided into two sections, magnetic field characterization and robot characterization. We introduce an empirical characterization method to parameterize the system. The system that is characterized here is used for experiments in Chapter 6 and 7.

5.2.1 Magnetic Field Characterization

The high-resolution manipulation of the magnetic robot requires an accurate model of the magnetic field and its gradients. In Chapter 6, we show that for reliable manipulation, it is important to have a spatial representation of the magnetic field to avoid creating regions of high variability in the magnetic field gradient close to the robot. Furthermore, the control algorithms proposed in Section 6.2 hinges on exploiting the spatially nonlinear magnetic field gradient to independently control multiple robots. Thus, in order to achieve sub-millimeter precision in robot position, it is important to have an accurate model that maps the vector of input currents into the system to the spatial magnetic field throughout the workspace.

Creating an accurate model of the magnetic field is challenging because most magnetic manipulation systems, including our own, are custom built. Variability can arise in custom built systems if the electromagnetic coils are hand wound. Additionally, rapid prototyp-

ing techniques and one-off designs can lead to low tolerances on measurements. For these systems, there does not exist a set of specifications that detail the shape of the magnetic field generated by each electromagnetic coil and the strength of the field. While electromagnetism is well studied and there are analytical equations that govern the magnetic field created by current through a wire, implementing these equations typically involves making some assumptions. Moreover, some of these equations do not hold for our system because the workspace is in close proximity to the workspace.

To validate a model, we need to measure the magnetic field. There is a wide range of commercially available tools for measuring magnetic fields. We needed to select one with 3-axes of measurement and a small form factor that allowed it to be maneuvered around the workspace.

Magnetometer

We operate close to the electromagnetic coils because the magnitude of the magnetic field decays at a rate of distance to the third power. As a result, using a point dipole model based on the geometry of the coils does not generate an accurate model of the magnetic field. In this model, we assume that the magnetic fields linearly superimpose and that neighboring electromagnetic coils do not interfere with one another. Moreover, we try to fit the magnetic field measurements to a point-dipole model parameterized to fit empirically measured data.

First, a 3-axis magnetometer, HMC 5843 Honeywell, is used to measure the magnetic field and an Arduino Uno is used for data acquisition. The position of the magnetometer is determined by tracking the AprilTag attached to the sensor using the overhead camera on the magnetic manipulation platform. Magnetic field readings are collected at 9 different locations on the workspace for a variety of different input currents being applied. For ease of data collection, currents are changed at a rate of 0.5 Hz, while magnetometer readings are taken at 1 Hz. Since the magnetometer returns a time averaged magnetometer reading, it is important to avoid taking readings right after the current has changed to minimize error.

This experiment is used to determine Earth's magnetic field, which is taken by averaging the baseline magnetic field across the workspace when all the coils are off. Earth's magnetic

field is measured as $\vec{B}_{Earth} = [36, -0.6]\,\mu\text{T}$, in the workspace fixed coordinate frame. Once these measurements are taken, it is important not to move the magnetic manipulation system otherwise, the calibration will need to be repeated.

To determine the magnetic field generated by one coil, Earth's magnetic field is subtracted from each field measurement. Figure 23a shows an example of the raw data from the measurements for coil 3, at [57.1, 0]mm with 1 A of current through it. As shown, the data taken using this method can be noisy. The data is sufficient to determine an order of magnitude for the magnet moment for the point dipole model, however, it does not provide the level of detail desired.

Empirical Method

The dipole moment of the electromagnetic coil is parameterized by the geometry of the coil using a solenoid representation. The multipole expansion for the vector potential of a line current of volume, V, is given by [30],

$$m = \frac{1}{2}\int (r \times V)\, dv \tag{5.12}$$

where m is the dipole moment, r is the distance from the center to the current carrying element of wire and integrated over the volume, v. The solution to (5.12) for a solenoid with a circular cross-section is given by [55],

$$m = \frac{\mu_0}{12} JL\left(3R^3T + 3R_iT^2 + T^3\right). \tag{5.13}$$

where J is the current density of the wire, L is the length of the winding along the coil axis direction, R_i is the inner radius of the coil, T is the winding thickness of the coil.

To refine the model for each coil, we ran experiments with a magnetic robot to empirically characterize the magnetic field. The robot is initialized in Earth's magnetic field and then one coil is turned on. The trajectory of the robot is divided into segments of length dt. For each segment of the trajectory, the dynamics of the robot is simulated using the state of the robot from the experiment. We optimize the inner radius of the coil to minimize the error

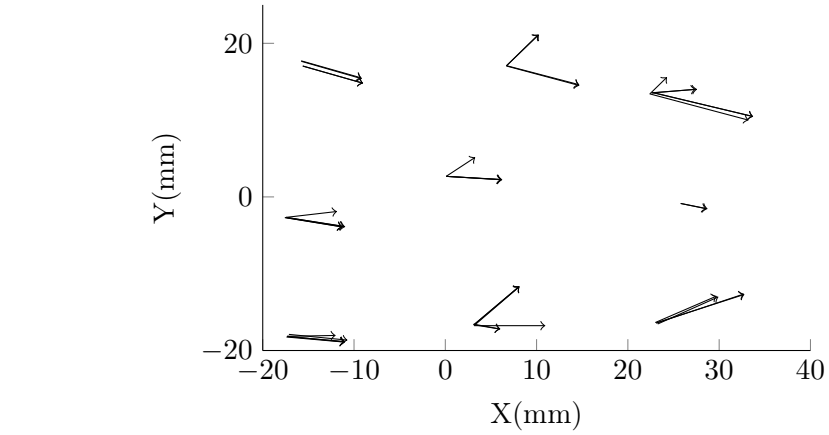

(a)

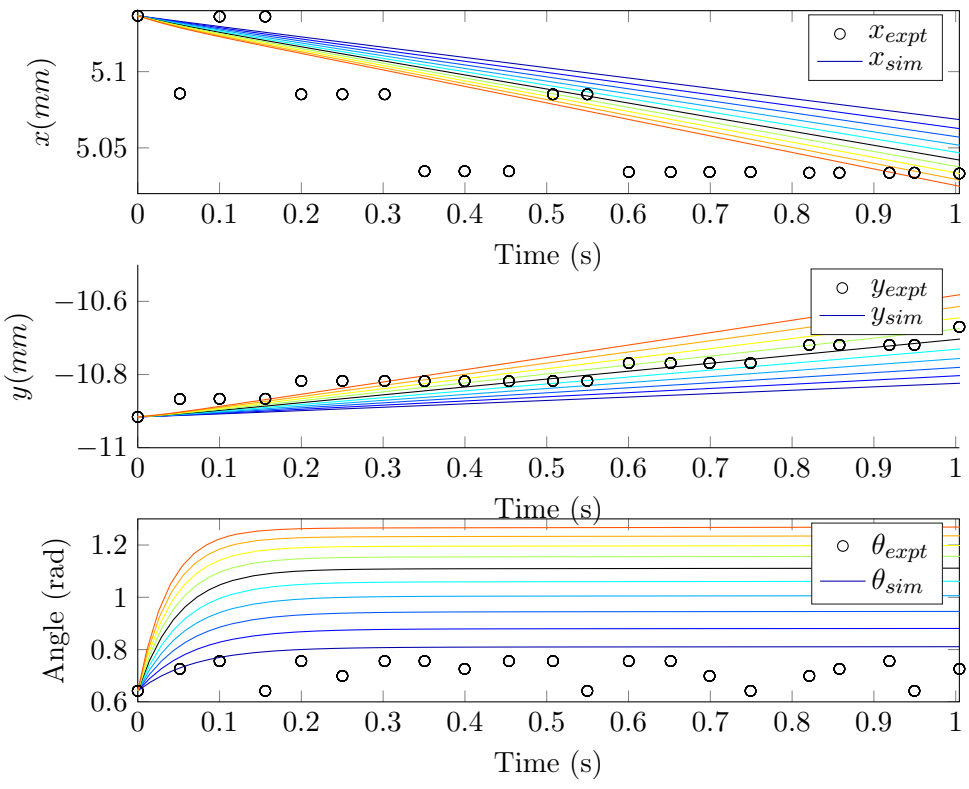

(b)

Figure 23: Calibration of the magnetic field. (a) Measurement magnetic field for Coil 3 at $[57.1, 0]$ with a current of 1 A (includes Earth's magnetic field.) (b) Optimization of coil parameters for coil 2. The lines show the trajectory for several different values of inner radius of the coil, with the black line showing the result with minimum error.

Table 3: Electromagnetic coils parameters.

Wire diameter, W_d	0.643	mm
Wire cross-sectional area, W_a	$\frac{\pi}{4}W_d^2$	mm^2
Length of coil winding, L	6	mm
Thickness of coil, T	3	mm
Inner diameter of coil R_i	O1	mm

between the robot position at the end of dt in simulation and experiment. This calibration is run for each coil such that each coil has a unique inner radius. Figure 23b shows the comparison between the simulation data and the trajectory for a window of 1s. The results are for a current of 2 A through coil 2. The different colors indicate simulations results for different values of R_i and the black line indicates the best fit value to minimize the error in the position at the end of this time window.

To add further detail to the simulation, we can measure the inductance of the electromagnetic coils to determine the temporal variation in the current and how that is affected by the frequency that the current is updated. The coils in this setup have an inductance of 540-552 μH at 1 kHz.

There are several sources of error with this method of calibration, including error in the tracking of the April Tag, discrepancy between the sensor position and assumed position at at the center of the device. Moreover, we assume that the three axes of the magnetometer are aligned, which is not true. Due to the accuracy desired for microscale precision in manipulation, a magnetometer with more detailed sensor placement would lead to a better calibration.

5.2.2 Robot Characterization

This section outlines experiments that can be used to empirically derive the linear drag coefficient and rotational drag coefficient of the robot. The drag coefficient is a function of geometry of the robot, therefore, for each robot of a different shape and size, these experiments will need to be run to derive their specific drag coefficient. The magnetic robot that is characterized in this section is made of Samarium Cobalt, SmCo, cut into an isosceles

triangle to allow the orientation of the robot and therefore the direction of the magnetic dipole moment to be determined visually. This robot is also used in experiments in Section 7.5.

At low Reynolds number, inertial forces are negligible. In a Stokes regime, the force and linear velocity relationship is linear and the torque and angular velocity relationship is linear. While the Reynolds number for this system is about unity, we show that the linear assumption generates a model that closely simulates empirical data.

Linear Drag Coefficient

At low Reynolds number, the linear velocity, $\vec{v}$, and force relationship, $\vec{F}$, is related by,

$$\vec{F} = C_L \vec{v} \tag{5.14}$$

where C_L is the linear drag coefficient with units kg s^{-1}. The force applied on the magnet by a magnetic field is given by (5.8). To relate the applied magnetic field to the velocity, we combine equations (5.14) and (5.8),

$$M_r V \left(\hat{m} \cdot \nabla\right) B = C_L \vec{v} \tag{5.15}$$

in this expression, the magnetic dipole moment of the robot $\vec{m}$ is written as $M_r V \hat{m}$, where M_r is the remnant magnetization of the robot, V is the volume of the robot, $\hat{m}$ is the unit vector of the dipole moment of the robot. This allows the robot dependent constants, M_r and V, to be factored into the drag coefficient ratio, $\mathbb{C}_L$, which we define as,

$$\mathbb{C}_L = \frac{C_L}{M_r v} \tag{5.16}$$

and we can rewrite (5.15) as,

$$\mathbb{C}_L = \frac{|\hat{m} \cdot \nabla B|}{|\vec{v}|}. \tag{5.17}$$

To compute $\mathbb{C}_L$ for the magnetic robot, we need a magnetic field source with a known

magnetic field. A permanent magnet with known remnant magnetization, B_r, can be used. The source should be chosen such that the velocity of the magnet is on the same order of magnitude as the velocity of the magnet when controlled by the electromagnetic coils. The magnetic dipole field of the permanent magnet is assumed to be a point-dipole

$$\vec{B} = 3\frac{(\vec{m} \cdot r)\, r}{|r|^5} - \frac{\vec{m}}{|r|^3} \tag{5.18}$$

where r is the distance from the point-dipole and $\vec{m}$ is the magnetic dipole moment of the permanent magnet and the magnetization of the permanent magnet, $M = \frac{B_r}{\mu_0}$, is calculated from the remnant magnetization of the permanent magnet.

This model is accurate far from the source, we assume that this distance is two-body lengths away from the source and we truncate the data 8 mm from the source. For each data point along the trajectory, the position and orientation of the magnet is determined using computer vision. While the magnetic field across the robot will vary, the robot is modeled as a point magnet at the areal center of the projection of the robot in the image. The velocity is calculated by numerically differentiating the position data and then smoothing it using a sliding window average.

The orientation of the magnetic source relative to the magnetic robot strongly influences the magnetic field at the location of the robot and therefore the force exerted on it. With the size of the magnets being small and the camera needing to be far enough away to capture the full trajectory, the magnet is just represented by a few pixels. Therefore, the orientation of the magnetic source is difficult to determine accurately from the images. Instead, the assumed orientation of the magnetic source is chosen by minimizing the absolute difference between the angle of the robot's magnetic dipole moment and the direction of the magnetic field at the respective position, which is the sum of the magnetic field from the permanent magnet source and Earth's magnetic field. The magnitude of Earth's magnetic field is on the order of magnitude of the applied field by the electromagnetic coils and is strong enough to reorient the magnetic robot to align to Earth's magnetic field (see Section 6.2 for detailed discussion.)

Figure 24 shows an example trajectory of a permanent magnet moving towards a stationary permanent magnetic field source. The magnetic field source is a stack of 2 neodymium (NdFeB, Grade N42) magnetic cylinders L:1/16 mm dia.:1/16 mm (K & J Magnetics, Inc.), with remnant magnetization, B_r =1.32 T. The data from the trajectory of the robot is shown in Figure 24a. Figure 24a shows the comparison between experimental data and the model for the unit vectors of force and the magnetic field for the permanent magnetic source at an angle of 2.94 rad from the x-axis at location $[0, 0]$. Figure 24c shows the drag coefficient ratio, $\mathbb{C}_L$, at each point along the trajectory of the robot. While the drag coefficient ratio varies throughout the trajectory, the variation is small. We choose a value of $\mathbb{C}_L$= 10 kg s^{-1} A^{-1} m^{-2} to represent the behavior.

Rotational Drag Coefficient

At low Reynolds number, the angular velocity, ω, and torque, τ, are related by,

$$\tau = C_R \omega \tag{5.19}$$

where C_R is the rotational drag coefficient with units N m s. The torque applied on a magnet by the applied magnetic field is given by equation (5.9). To relate the applied magnetic field to the angular velocity, we combine equation (5.19) and (5.9),

$$M_r V \left(\hat{m} \times \vec{B} \right) = C_R \omega \tag{5.20}$$

As with the linear drag coefficient ratio, we define the rotational drag coefficient ratio, $\mathbb{C}_R$,

$$\mathbb{C}_R = \frac{C_R}{M_R V} \tag{5.21}$$

and we can rewrite equation (5.20) into a form of values that can be empirically derived,

$$\mathbb{C}_R = \frac{|\hat{m} \times \vec{B}|}{|\omega|}. \tag{5.22}$$

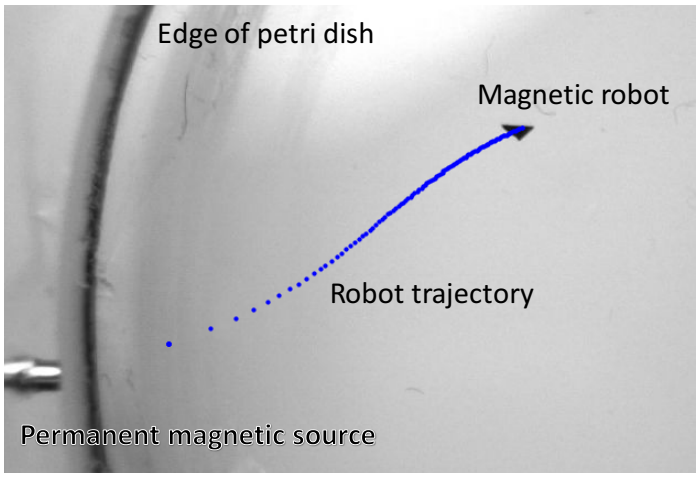

(a)

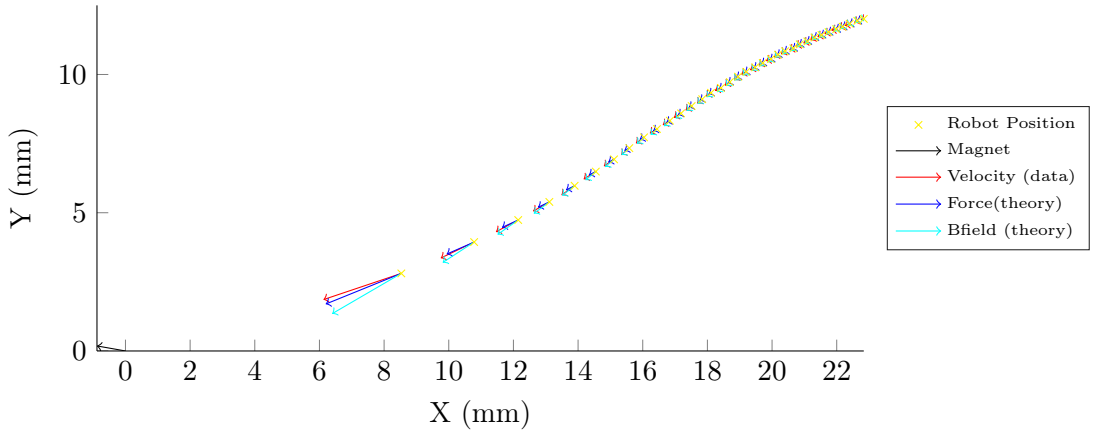

(b)

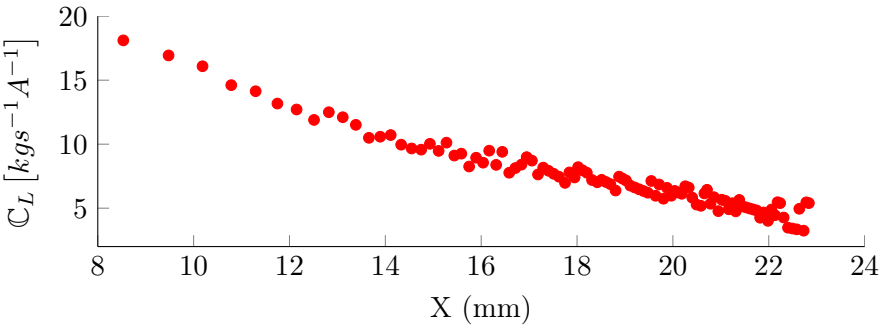

(c)

Figure 24: Empirically deriving the linear drag coefficient. (a) Overhead view of experimental setup with trajectory of the magnet in blue. (b) Comparing the theoretical force and velocity of the robot from experiments. (c) Linear drag ratio as a function of x-position.

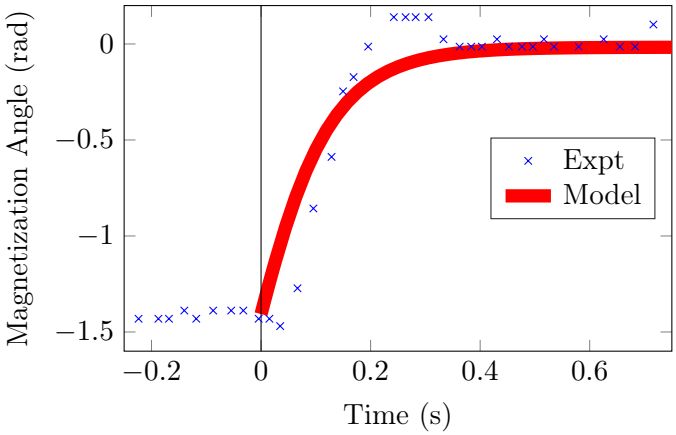

Figure 25: Empirically deriving the rotational drag coefficient. The Helmholtz coils are turned off at time = 0s. Earth's magnetic field is $\vec{B}_{Earth} = [36, -0.6]\,\mu$T. The red line shows the angle of the robot for $\mathbb{C}_R = 3.2 \times 10^{-6}$ kg m s^{-1}.

To compute $\mathbb{C}_R$ for the magnetic robot, we apply a uniform magnetic field to rotate the robot while minimizing translation. A uniform magnetic field is applied by using a pair of electromagnetic coils in a Helmholtz coil configuration to apply a uniform magnetic field in the positive y-direction. The electromagnetic coils are turned off and the robot rotates to align to Earth's magnetic field. The orientation of the robot is tracked using computer vision, the angular velocity is computed by numerically differentiating the orientation of the robot and the torque is compute at each orientation using equation (5.9).

Figure 25 shows the experimental data collected to derive the rotation drag coefficient ratio, $\mathbb{C}_R$. A least squares fit is used to solve for the rotational drag coefficient ratio by minimizing the difference between the experimental angle and theoretical angle of the robot. For our robot, the rotational drag coefficient ratio, $\mathbb{C}_R = 3.2 \times 10^{-6}$ kg m s^{-1}. The orientation of the angle using this value is shown by the red line in Figure 25.

5.3 Conclusion

This chapter reviews the analytical solution for manipulating a magnetic particle using magnetic fields. Specifically, the analysis considers the magnetic field generated by a circular current loop. The analysis is extended to consider the characterization of a magnetic manipulation system consisting of 4 stationary magnetic coils used to manipulate a magnetic

robot floating at a fluid interface. We outline a set of experimental studies that can be used to determine the dynamics of a magnetic robot being manipulated by a magnetic field generated by electromagnetic coils. We define drag coefficient ratios that relate the applied field to force and torque exerted on a robot. Procedures for using a known magnetic field to calibrate values for the drag coefficient ratio are presented. We found that when using a magnetometer to measure the magnetic field, locating the precise position of the sensor for each axis within the measurement device package is challenging and can lead to measurement error.

Chapter 6

Control of Multiple Robots

A major challenge of manipulating multiple magnets at the microscale is addressing them individually using global magnetic fields. In particular, it is difficult to control magnets which are identical in all aspects.

This chapter explores the use of electromagnetic coils to control multiple magnetic robots. We propose a force control method to manipulate multiple magnets by utilizing spatially varying gradients of the magnetic field with stationary electromagnetic coils. We first analyze a one-dimensional case where two electromagnetic coils are arranged linearly and permanent magnets are restricted to move axially along the vector of magnetization. Extending this to a planar system, we analyze a system with four electromagnetic coils arranged in a square around the workspace controlling two permanent magnets.

The research in this chapter was originally published in [84, 86].

6.1 Control of Multiple Magnets in 1D

We analyze a one-dimensional case where electromagnetic coils are arranged linearly and permanent magnets are restricted to move axially along the vector of magnetization. A mathematical model and dynamical simulation using empirically derived parameters demonstrate the ability to control the n-magnets independently using n-coils. We developed an experimental testbed to validate the mathematical and dynamical model.

6.1.1 Linear Configuration

We consider the one-dimensional problem where two permanent magnets are orientated to be repelling and are free to slide linearly in one dimension. Two electromagnetic coils bound the workspace and have their axes aligned along the same axis, Figure 26(a).

For the configuration illustrated in Figure 26(a) where the permanent magnets are restricted to travelling along the axis of the coil, Equation (5.1) simplifies to the magnetic field on-axis of one turn of wire of the electromagnetic coil,

$$B_{loop} = \frac{\mu_0 I R^2}{2\left(x^2 + R^2\right)^{3/2}} \tag{6.1}$$

where x is the distance from the center of the fixed electromagnetic coil to the center of the free permanent magnet. To calculated the magnetic field of the entire electromagnetic coil, this value must be multiplied by the number of turns of wire that make up the electromagnetic coil, n. Applying Equation (5.8) and (5.11), the force exerted on each magnet, F_1 and F_2, at position x_1 and x_2 can be written in matrix form:

$$\begin{bmatrix} F_1 \\ F_2 \end{bmatrix} = \begin{bmatrix} -\mu_1 \frac{3x_1\mu_0 R_1^2 n}{2\left(x_1^2+R_1^2\right)^{\frac{5}{2}}} & -\mu_1 \frac{3(x_1-L)\mu_0 R_2^2 n}{2\left((x_1-L)^2+R_2^2\right)^{\frac{5}{2}}} & -\frac{\mu_0 m_1 m_2}{4\pi(x_2-x_1)^2} \\ \mu_2 \frac{3x_2\mu_0 R_1^2 n}{2\left(x_2^2+R_1^2\right)^{\frac{5}{2}}} & \mu_2 \frac{3(x_2-L)\mu_0 R_2^2 n}{2\left((x_2-L)^2+R_2^2\right)^{\frac{5}{2}}} & \frac{\mu_0 m_1 m_2}{4\pi(x_2-x_1)^2} \end{bmatrix} \begin{bmatrix} I_1 \\ I_2 \\ 1 \end{bmatrix} \tag{6.2}$$

We apply this equation to the experimental implementation where the coils are the same size, $R = R_1 = R_2$ and the permanent magnets are assumed to always be aligned along the x-direction and with identical magnetization, $\vec{m} = m\hat{x}$, $|m| = m_1 = m_2$, $\mu = \mu_1 = \mu_2$. To investigate the equilibrium point, we set the sum of forces to zero such that the force between the magnets is equal to the opposing force exerted by the electromagnetic coils,

$$\begin{bmatrix} \frac{\mu_0 m^2}{4\pi(x_2-x_1)^2} \\ -\frac{\mu_0 m^2}{4\pi(x_2-x_1)^2} \end{bmatrix} = \begin{bmatrix} -\mu \frac{3x_1\mu_0 R^2 n}{2\left(x_1^2+R^2\right)^{\frac{5}{2}}} & -\mu \frac{3(x_1-L)\mu_0 R^2 n}{2\left((x_1-L)^2+R^2\right)^{\frac{5}{2}}} \\ \mu \frac{3x_2\mu_0 R^2 n}{2\left(x_2^2+R^2\right)^{\frac{5}{2}}} & \mu \frac{3(x_2-L)\mu_0 R^2 n}{2\left((x_2-L)^2+R^2\right)^{\frac{5}{2}}} \end{bmatrix} \begin{bmatrix} I_1 \\ I_2 \end{bmatrix} \tag{6.3}$$

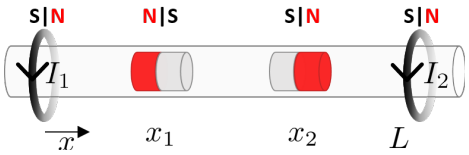

(a)

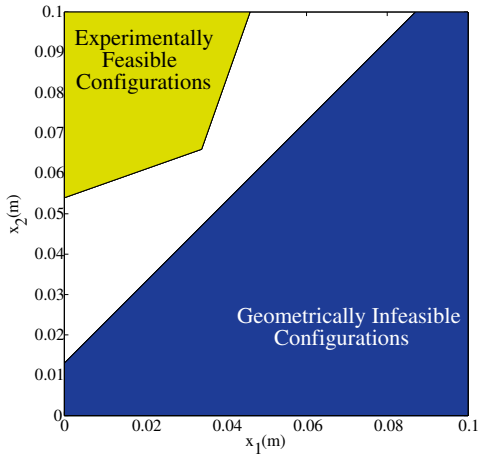

(b)

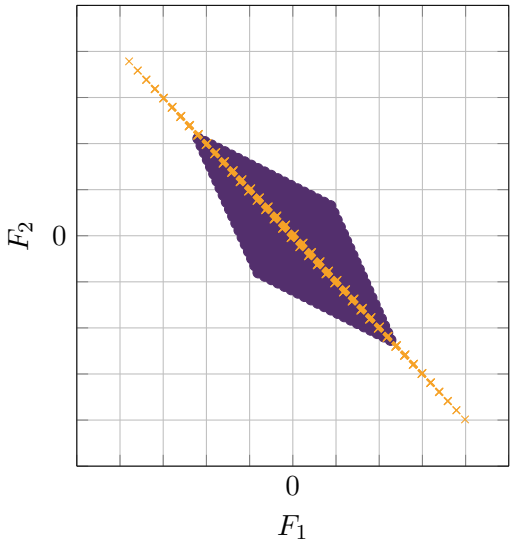

(c)

Figure 26: Linear configuration. (a) Schematic showing magnetic poles of permanent magnet and direction of poles when current is positive in coils. (b) Blue (dark) region shows geometrically inaccessible configurations and yellow (light) region shows experimentally feasible configurations given the current constraints. (c) Orange (light) region shows quantitatively the possible forces that can be exerted on magnet 1, F_1, (x-axis) and 2, F_2, (y-axis) for $[x_1, x_2] = [0.1, 0.9]$; purple (dark) regions for $[x_1, x_2] = [0.35, 0.65]$.

If a solution exists for values of the currents to reach the desired positions, the solution can be found by inverting the 2x2 matrix and pre-multiplying that to the vector on the left containing the inter-magnet forces. The determinant of the 2x2 matrix shows that a solution for the currents through the two coil exists for arbitrary values of x_1 and x_2 with the exception of $x_1 \neq x_2$, a configuration that is physically infeasible. While these configurations are theoretically reachable, in a practical application of this model, the reachable configurations are constrained by the range of current values that can be exerted. The experimentally feasible configurations simulated using the parameters in Table 4 are shown in Figure 26(b). The potential function, U, is used to explore the stability of the equilibrium; it is related to the force by, $F = -\frac{dU}{dx} = 0$. The stability is determined by computing the Hessian and solving for the eigenvalues. The equilibrium points for the linear configuration are unstable when the orientation of magnet 1 and 2 are the same and stable when the orientation of magnet 1 and 2 are opposite as in Figure 26(a). While theoretically the result is very similar, in application, stable systems are more forgiving to error and feedback loops with delays. The stable system is what we implement here.

In simulation, a system consisting of three magnets and three electromagnetic coils is explored. The third coil is added just right of coil 2 in the 2 magnet configuration, Figure 27. The forces acting on the system for the stable configuration of magnet orientations are given by Equation (6.4).

$$\begin{bmatrix} F_1 \\ F_2 \\ F_3 \end{bmatrix} = \begin{bmatrix} -\mu\frac{3x_1\mu_0R^2n}{2\left(x_1^2+R^2\right)^{\frac{5}{2}}} & -\mu\frac{3(x_1-L_2)\mu_0R^2n}{2\left((x_1-L_2)^2+R^2\right)^{\frac{5}{2}}} & -\mu\frac{3(x_1-L_3)\mu_0R^2n}{2\left((x_1-L_3)^2+R^2\right)^{\frac{5}{2}}} & (x_3-x_1)^{-2}-(x_2-x_1)^{-2} \\ \mu\frac{3x_2\mu_0R^2n}{2\left(x_2^2+R^2\right)^{\frac{5}{2}}} & \mu\frac{3(x_2-L_2)\mu_0R^2n}{2\left((x_2-L_2)^2+R^2\right)^{\frac{5}{2}}} & \mu\frac{3(x_2-L_3)\mu_0R^2n}{2\left((x_2-L_3)^2+R^2\right)^{\frac{5}{2}}} & (x_1-x_2)^{-2}-(x_3-x_2)^{-2} \\ -\mu\frac{3x_3\mu_0R^2n}{2\left(x_3^2+R^2\right)^{\frac{5}{2}}} & -\mu\frac{3(x_3-L_2)\mu_0R^2n}{2\left((x_3-L_2)^2+R^2\right)^{\frac{5}{2}}} & -\mu\frac{3(x_3-L_3)\mu_0R^2n}{2\left((x_3-L_3)^2+R^2\right)^{\frac{5}{2}}} & (x_2-x_3)^{-2}-(x_1-x_3)^{-2} \end{bmatrix} \begin{bmatrix} I_1 \\ I_2 \\ I_3 \\ \frac{\mu_0m^2}{4\pi} \end{bmatrix} \tag{6.4}$$

A similar analysis for the 3 coil configuration will show that a solution for currents exists to reach arbitrary values of x_1, x_2 and x_3 as long as the magnets are in a physically reachable configuration and maintain the same order, $x_1 < x_2 < x_3$.

The currents to reach the desired set of positions can be found by setting the resultant forces, $F_j = 0$, rearranging the equation and inverting the 3-by-3 matrix. A simulation of three magnets moving along a trajectory of 3 different distances is shown in Figure 28. The

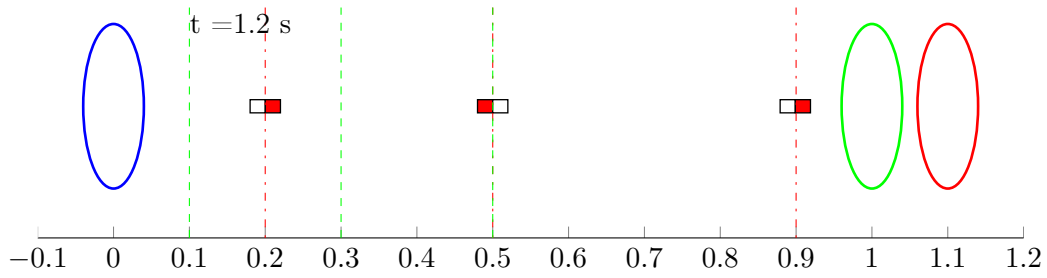

Figure 27: Schematic of 3 magnet simulation showing start locations in dotted lines with magnets in goal location for simulation experiment at time 1.2 seconds. Magnets are oriented in alternating reverse polarity so that the equilibrium positions are stable. Coils (ellipses) and magnets are ordered from left to right, in order 1, 2, 3. X-axis shows the non-dimensionalized position, $\frac{x}{L_2}$.

equations of motion are non-dimensionalized using the variable definitions with units:

$$\begin{aligned} \tilde{x_i} &= \frac{\tilde{x_j}}{R} && [=] \, dimensionless \\ \alpha &= \frac{L_2}{R} && [=] \, dimensionless \\ \tilde{I_j} &= \frac{\mu_0 \mu I_j}{R^2} && [=] \, N \\ \tilde{F_i} &= F_i && [=] \, N \end{aligned}$$

In this non-dimensionalized simulation, the coils are placed at a distance 0, 1 and 1.1. No bound is placed on the current through the coils. A quintic polynomial position function between two points is planned for each pair of start and goal locations to guarantee smooth acceleration. The update frequency and feedback loop is at 100Hz and a PD controller is implemented.

Similarly, to control more magnets in this linear configuration, additional coils can be added to the ends beyond the existing electromagnetic coils to match the number of magnets.

6.1.2 System Implementation

An experimental system is constructed to validate the ability to control the position of two magnets with two current inputs to the electromagnetic coils. In these experiments, the orientation of the magnets are opposing so that the equilibrium positions are stable.

The electromagnetic coils are made of 6.5m of 22 gauge, enamel coated copper wire (EIS) wound around an acrylic spool with an inner diameter of 51mm. Up to 5A of current flows through the coils. The current through the electromagnetic coils is controlled by a

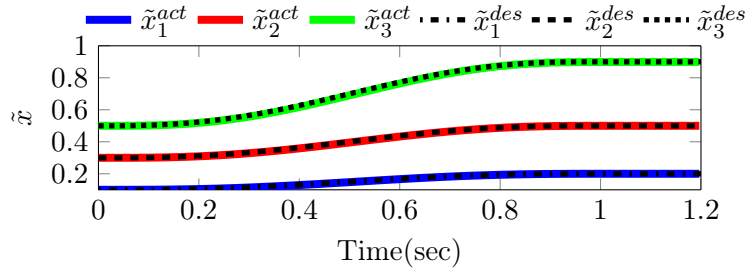

(a)

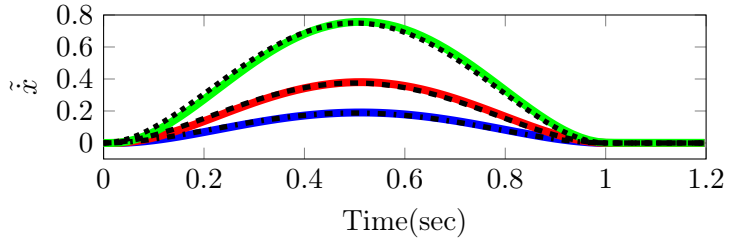

(b)

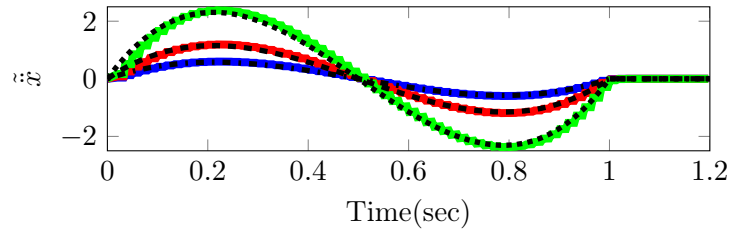

(c)

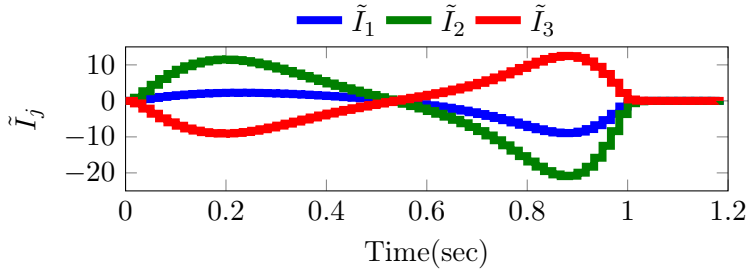

(d)

Figure 28: Simulation results from 3 magnet configuration driving magnet 1 between [0.1,0.2], magnet 2 [0.3,0.5], magnet 3 [0.5,0.9]. Non-dimensionalized variables showing desired values (des) in dashed black and actual values (act) in solid colored lines. (a) Position. (b) Velocity. (c) Acceleration. (d) Non-dimensionalized current updated at 100Hz.

micro controller board (Orion robotics) and sends pulse width modulated (PWM) signals through the coils. Each coil has a separate channel with a continuous 5A modulated signal, the effective current is assumed the corresponding fraction of the maximum current, $I = \frac{PWM}{512} I_{max}$. The permanent magnets are comprised of four neodymium-iron-boron (NdFeB) ring magnets, L:1.6mm ID:1.6mm OD:3.2mm (K& J Magnetics, Inc.), attached magnetically to increase length and total magnitude of the magnetic pole. The magnets are constrained in a clear plastic tube, the length of the magnet stack is greater than the inner diameter of the tube and prevents the magnet from flipping. The tube is dithered (vibrated) using a pager motor attached to one end of the tube to avoid stiction and to ensure the magnet can reach the stable equilibrium. A magnet of opposing polarity is placed at the ends of the tube to prevent the magnet from reaching the end and being ejected.

To determine the reachable equilibrium values given the physical constraints of the system, parameters for the magnitude of the magnetic pole and the magnetic dipole moment are determined empirically. Using these derived values and the limit of the current output to the coils, the feasible configurations of the magnets can be computed, yellow region in Figure 26(b). The feasible forces that can be exerted are shown for different position configurations in Figure 26(c). When magnets are close to the electromagnetic coils, a wider range of forces can be exerted than when the magnets are close to each other and far from the electromagnetic coils.

Position control is possible by implementing a feedback loop to compute the desired force in Equation (6.2). The position of the magnets is determined using vision feedback, a grayscale image is used to maximize frame rate. The magnets are covered in black tape and can be found in the image using a blob detector as implemented in OpenCV libraries [8]. A trajectory controller calculates the commanded force, F^{des}, using PID feedback from position and velocity with a feed forward acceleration term, $\vec{a}_T$.

$$\vec{F}^{des} = K_p \left(\vec{x}_T - \vec{x}\right) + K_d \left(\vec{v}_T - \vec{v}\right) + K_i \int \left(\vec{x}_T - \vec{x}\right) dt + \vec{a}_T M \tag{6.5}$$

where subscript T signifies the desired position, x, velocity, v, and acceleration, a, from

planned trajectory and without the subscript the actual position or velocity. K_p, K_d, K_i indicate the proportional, derivative and integral gains respectively. M is the mass of the magnets. This desired force is added to the inter-magnet force, left-hand side of Equation (6.3), to calculate the desired current.

Parameters

The force contribution by the electromagnetic coil on the magnet depends on two variables, the distance between the two as well as the current applied, Equation (6.2). This relationship is governed by the magnetic dipole moment for the magnet, μ, a value not typically specified for commercially available magnets. Two experiments are used to derive and verify this value. The setup consists of an electromagnetic coil, identical to that used in the system implementation; and a stack of four magnets attached to a 0-10 gram load cell (GSO-10, Transducer Techniques) using a brass (non-magnetic) screw. The force exerted between magnets with and without the screw is measured to determine that the presence of the screw does not have a significant effect on the force between the magnets. In the first experiment, the distance between the magnet and the electromagnetic coil is kept constant while the current was varied, Figure 29(a). As expected, the relationship is linear. From the slope of this plot, the magnitude of the magnetic dipole moment can be derived. To verify this value, the distance between the coil and magnet was varied while keeping the current constant. Figure 29(b) shows the data points collected and the model fit for two different currents.

The magnitude of the magnetic pole, m, in Equation (5.11) governs the force exerted between magnets. This value depends on material properties as well as geometry and is typically not part of the specifications of commercially available magnets. To determine the magnitude of the magnetic poles of the permanent magnet stack, m, the repulsion force between the magnets was measured for several distances. A stack of four magnets was attached to a stationary 0-10 gram load cell (GSO-10, Transducer Techniques). An identical stack of magnets was attached to an acrylic movable fixture. Rails were used to ensure the axes of the magnet stacks were aligned. Figure 29(c) shows the data points collected and

Table 4: Parameters for experimental setup

	Parameter	Value	Units
L	Distance between coils	0.100	m
R	Radius of coils	0.029	m
m	Magnitude magnetic pole	0.410	A m
μ	Magnitude magnetic dipole moment	5.5	A m^2
M	Mass of magnet	0.282	g
I	Current	$-5 < I < 5$	A
n	Number of turns of coil	44	

the linear least squares fit to the data using Equation (5.11). The distance between the magnets, r, was measured as the shortest distance between the magnets as this resulted in less error compared to defining r as the distance between magnet centers.

6.1.3 Results

To illustrate that the theoretical model matches the physical model well, an experiment was run in open loop with the right magnet stationary and the left magnet oscillating back and forth, the position and current profile are shown in Figure 30(a). The system has a lag in the response; this is likely a result of the dynamics of the system. While the model does not capture the dynamics of the system, the currents computed using the model are similar to the values necessary to drive the magnet to the desired locations. A controller can be used to improve the performance of the system.

Two examples of independent control with visual feedback are provided. First, a trajectory where both magnets are moving out of phase with the same amplitude (Figure 30(b)). Second, a trajectory where the right magnet is held still while the left magnet oscillates back and forth (Figure 30(c)). A trajectory controller to calculate the desired commanded force using PID feedback from position and velocity with a feed forward acceleration term is used, Equation (6.11). The current is updated at 5Hz.

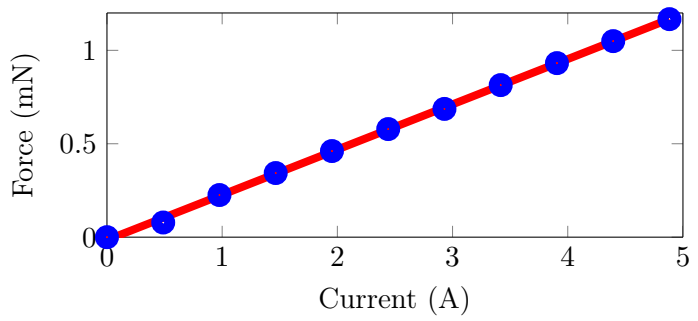

(a)

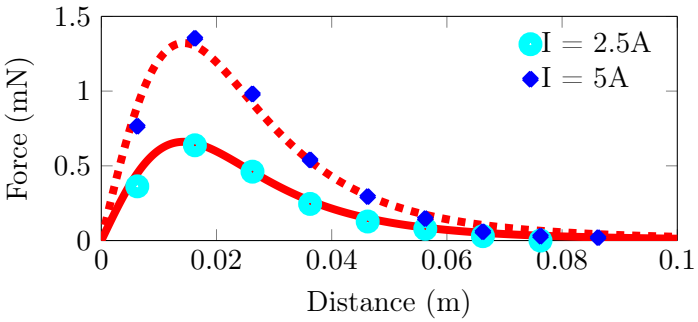

(b)

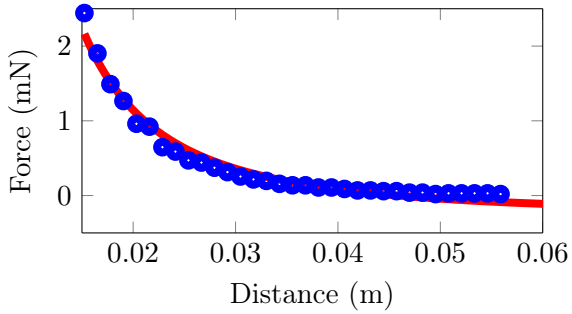

(c)

Figure 29: Empirically determining magnetic parameters. (a) Relating current to force for the magnet stack fixed at a distance of 1cm. This data is used to estimate the magnitude of the magnetic dipole moment, μ. (b) Verifying the μ value by comparing measured force for a constant current at varying distances to model fit using derived μ. (c) Relating distance and force between two magnets stacks. This data is used to estimate the magnitude of the magnetic pole, m.

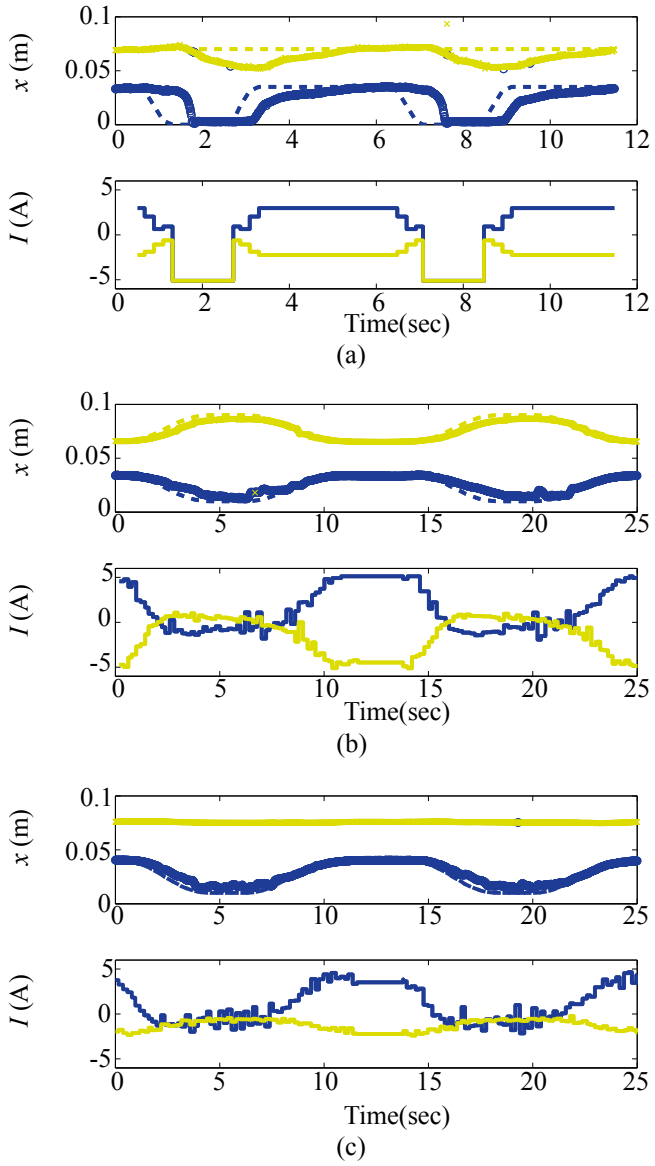

Figure 30: System implementation showing position of magnets and current value over time. Current is updated at 5Hz, position updated at 100Hz. Yellow (light) lines show position of magnet 1 and current value of coil 1, Blue (dark) lines show position of magnet 2 and current value coil 2. (a) Open Loop Control: right magnet held, left magnet oscillating. (b) Closed loop control: magnets oscillating out-of-phase. (c) Closed loop control: right magnet held, left magnet oscillating.

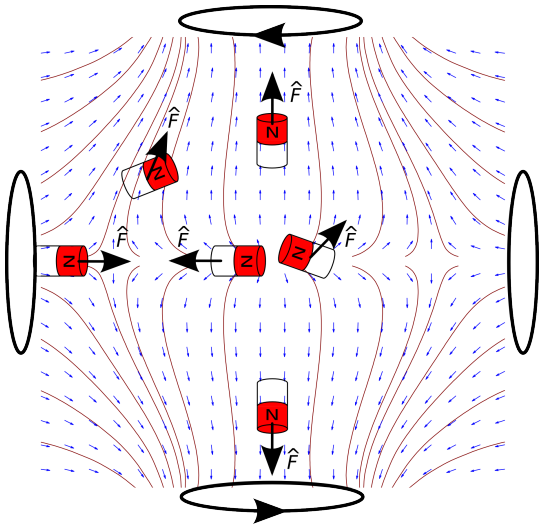

Figure 31: Independent control of multiple magnetic robots utilizing spatially varying gradients of the magnetic field. The grid of arrows shows the unit force exerted on a robot at that location as calculated using the closed-form solution for magnetic field generated by an electromagnetic coil. The streamlines are trajectories that a magnet would follow in a viscous fluid assumption using a Stokes model for fluid flow. Several magnets are illustrated in the workspace with their orientation and force vector, $\hat{F}$, illustrating the different forces exerted at different locations in the workspace.

6.2 Control of Multiple Magnets in a Plane

A major challenge of manipulating multiple magnets at the microscale is addressing them individually using global magnetic fields. In particular, it is difficult to control magnets which are identical in all aspects. This section proposes a force control method to manipulate multiple magnets by utilizing spatially varying gradients of the magnetic field with stationary electromagnetic coils. This approach is demonstrated using simulations and experiments on a macroscopic, planar system with two identical magnets controlled by four stationary electromagnets using visual feedback control. Simulation results show that this control strategy is also relevant for microscale systems by simulating a low Reynolds number environment.

6.2.1 Problem Formulation

To achieve independent control, the field gradient must be non-uniform such that different forces can be exerted within the workspace. Figure 31 shows the unit force vector field and corresponding streamlines lines generated by two opposing coils with equal and oppo-

site current to illustrate the direction of forces, $\hat{F}$, applied at various locations within the workspace and the orientation of a magnet at different locations. Depending on the location of the magnets, It is possible to move magnets away from each other or towards each other to obtain a grasping motion on a payload.

Equations (5.8), (5.2), (5.3) and (5.10) provide a mapping from the system inputs, currents, $\vec{u} = [I_1, I_2, I_3, I_4]^T$, to the forces, $\vec{F} = [F_{1,x}, F_{1,y}, F_{2,x}, F_{2,y}]^T$, at specific positions, $\vec{x} = [x_1, y_1, x_2, y_2]^T$. This mapping, Φ, which is a function of the robot positions, takes the current inputs and maps it to force exerted on the robots, $\Phi_x : U \rightarrow F$.

For clarity, the system of four equations can be written as:

$$\begin{aligned} F_{1,x} &= [m_{1,x}, m_{1,y}]\mathbf{D}_{1,x}\vec{u} \\ F_{1,y} &= [m_{1,x}, m_{1,y}]\mathbf{D}_{1,y}\vec{u} \\ F_{2,x} &= [m_{2,x}, m_{2,y}]\mathbf{D}_{2,x}\vec{u} \\ F_{2,y} &= [m_{2,x}, m_{2,y}]\mathbf{D}_{2,y}\vec{u} \end{aligned} \tag{6.6}$$

where $\vec{m}_i = [m_{i,x} m_{i,y}]$ is the vector of the magnetic dipole for the i-th robot and $\mathbf{D}_{i,j}$ is the 2×4 matrix form of the gradient of the magnetic field for the i-th robot in the j-th direction. $\mathbf{D}_{i,j}$ is expressed as:

$$\begin{aligned} \mathbf{D}_{i,x} &= \frac{\partial \mathbf{B}_i}{\partial x} \\ \mathbf{D}_{i,y} &= \frac{\partial \mathbf{B}_i}{\partial y}. \end{aligned} \tag{6.7}$$

The magnetic field at the position of the i-th robot is written in matrix form as a sum of the magnetic field contribution from each of the four coils is expressed as:

$$\mathbf{B}_i\vec{u} = \begin{bmatrix} \mathbb{B}_{1,i,x} & \mathbb{B}_{2,i,x} & \mathbb{B}_{3,i,x} & \mathbb{B}_{4,i,x} \\ \mathbb{B}_{1,i,y} & \mathbb{B}_{2,i,y} & \mathbb{B}_{3,i,y} & \mathbb{B}_{4,i,y} \end{bmatrix} \vec{u} \tag{6.8}$$

where $\mathbb{B}$ is the current-normalized magnetic field, the first index is the coil number, the

second is the i-th robot location and the third is the component direction.

To follow trajectories for two magnets in this planar configuration, the mapping, Φ_x, is inverted to solve for currents required to exert a desired force given the robot positions, $\Phi_x^{-1} : F \to U$. This inverse mapping cannot be derived explicitly because the force does not linearly depend on current, given that the orientation of the magnetic dipole, $\vec{m}$, is also a function of the current. The desired force is calculated by the feedback control algorithm and can be a function of the present and desired position, velocity and acceleration of the magnet. The desired force implemented in the simulation and experiments are described in the respective sections.

6.2.2 Approximate Model

To simplify the computations, a point-dipole model is used to approximate the magnetic field generated by the electromagnetic coil, equation (5.2), (5.3). The magnetic field generated by a coil with radius R centered at $[x, y]$ = [0,0] mm, oriented with its axis along the y-axis, with a current I computed by the point-dipole model is given by

$$\begin{aligned} B_x &= \frac{\mu_0 I R^2}{4r^3}\left[2 - \frac{3y^2}{r^2}\right] \\ B_y &= \frac{3\mu_0 I R^2 xy}{4r^5} \end{aligned} \tag{6.9}$$

where $r = \sqrt{x^2 + y^2}$, the distance from the center of the coil.

Far away from the coil, $R << r$, the magnetic field computed by the exact solution using elliptic integrals converges to the point-dipole model. Close to the coil, Figure 39(c,d) compares the discrepancy in the direction and magnitude of the magnetic field near one coil of radius 25.5 mm positioned at $[x, y] = [-57.5, 0]$ mm to mimic coil 1 in the experimental setup. The plot region represents the 60 mm square workspace centered at $[0, 0]$ mm, which is the center of the four coils. As expected, close to the edge of the coil, the angle and magnitude discrepancy is the greatest, and is relatively small at the center of the workspace.

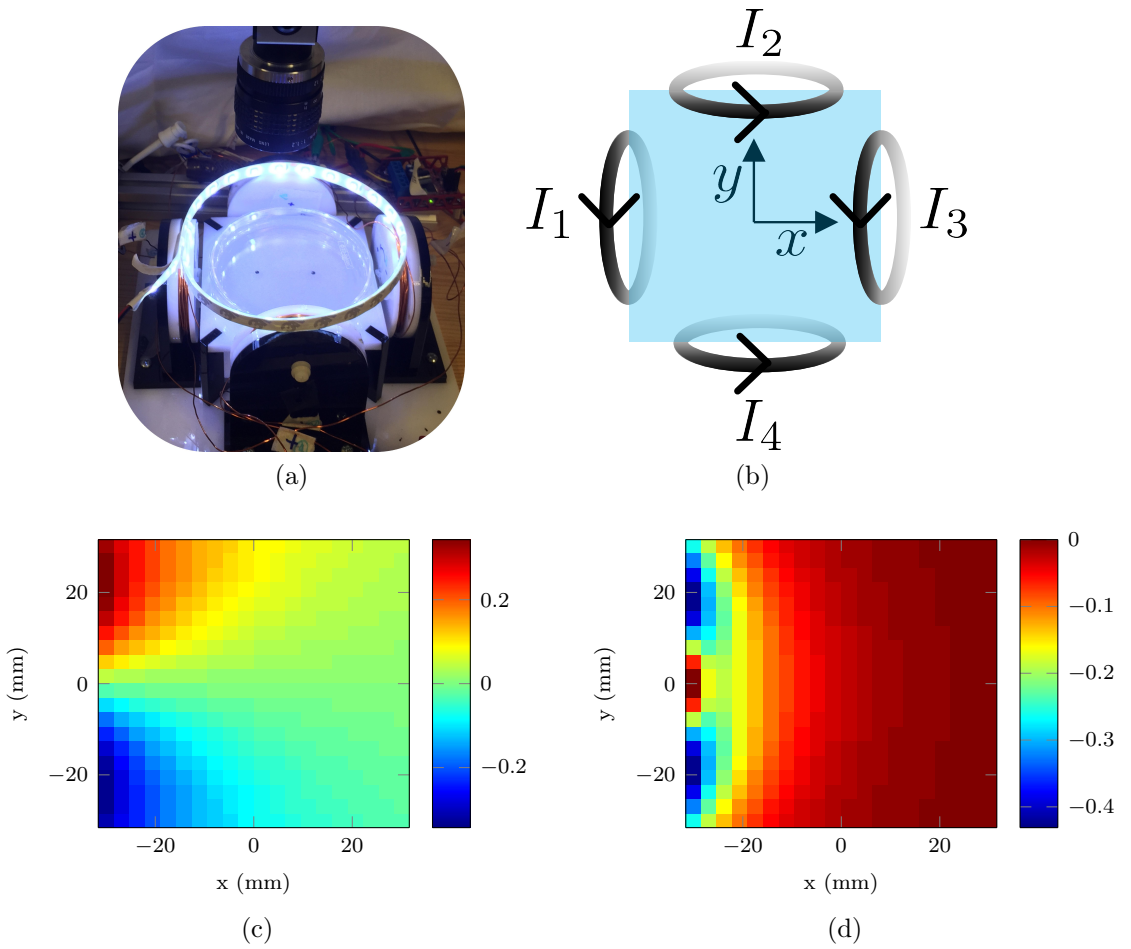

Figure 32: (a) Image of experimental implementation. The petri dish shown has a diameter of 85 mm and the magnets contained in the dish each have a diameter of 2 mm. (b) Schematic of coil placement. (c) Comparison between the angle of the magnetic field computed by elliptic integral and point-dipole model measured in radians. (d) Comparison between normalized magnitude of magnetic field (unit-less).

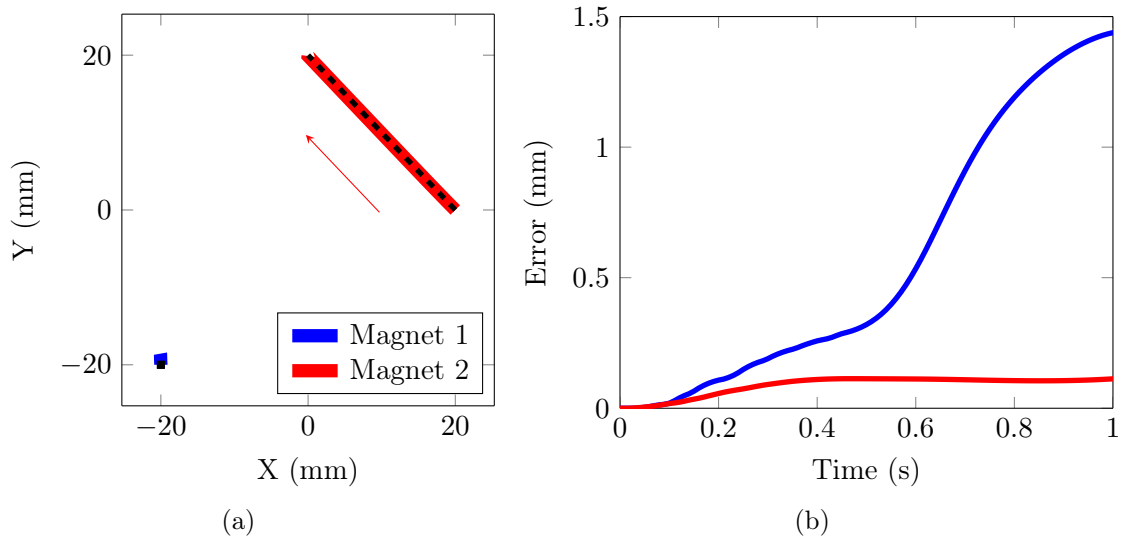

Figure 33: Simulation results. (a) Trajectory of magnets in simulation, colored markers represent the actual trajectory and the dotted black line represents the desired trajectory. (b) Position error from trajectory waypoints. (See Supplementary Video.)

6.2.3 Simulation

Control of the position of 2 magnets using the four coil system is first demonstrated in simulation. The magnetic field generated by the coils is modeled as a point-dipole using equation (6.9). The force exerted at each magnet is computed using equation (6.6). The parameters used for the electromagnetic coil and magnet simulate the experimental setup and are described in Section 6.2.4.

The equations of motion consider the force exerted on each robot from the electromagnetic coil and a drag force. Inter-magnet forces are not included because the electromagnetic coils are unable to pull apart magnets once they have attached to each other. Therefore, the trajectories planned ensure a distance between the magnets such that the interaction force between magnets is small and negligible compared to the force exerted by the electromagnetic coils. To simulate the magnets floating, the drag force is modeled as quadratic drag, where the force is proportional to the square of the velocity of the robot,

$$\vec{F}_{drag} = -\frac{1}{2}|v|^2 \rho C_D A \hat{v} \tag{6.10}$$

where ρ is the density of water, C_D is the drag coefficient, A is the cross-sectional area of the object and v is the velocity of the magnet . For simplicity, the drag force is calculated using the model for a sphere moving in a fluid. A drag coefficient of 0.47 is used and the area is modeled as the cross-sectional area of a sphere with diameter 2 mm. This is likely an overestimate of the drag on a flat plate, because the drag on a sphere would be greater; additionally, the plate is at an air-water interface as opposed to submerged fully in water. Inertial forces are observed in the experiments, and therefore quadratic drag is used. When the electromagnets switch from on to off, the magnet continues to drift for a short but perceivable period of time. The Reynolds number in simulation is on the order of 10^0.

A trajectory with waypoints defined by time, desired position, velocity and acceleration is pre-computed. A PD controller with a feed forward term is used. The controller is updated at 100 Hz and the position of the robot is propagated between updates as a result of the current through the coils. At each controller update, a numerical solver is used to calculate the currents required to achieve the desired force at the present position of each robot by solving the system of four equations (6.6). MATLAB is used to simulate the system and the numerical solver function *vpasolve* is used to compute solutions to the system of equations (6.6). The differential equation solver function *ode45* is used to calculate the position of the magnet as a result of the applied force.

Figure 33 shows a simulated trajectory where one robot is held at coordinate [-20,-20] mm and the other travels between [20, 0] to [0, 20] mm. This example trajectory is used to illustrate our control strategy because holding one magnet still while moving another magnet within the same workspace is challenging using stationary electromagnetic coils. Additional simulation examples are shown in the video included in the Supplementary Materials.

A fast update rate is needed because there can be high spatial variation in the magnetic field gradient causing changes in velocity as the magnet moves through space. Moreover, by updating the desired position to the next waypoint when the magnet position is within a certain bounding distance, as opposed to temporally prescribing the trajectory, can reduce position error for more complicated trajectories or when position errors are large. This

position based waypoint update policy is implemented in the experimental system.

6.2.4 System Design

Each electromagnet consists of a coil that has an inner diameter of 51 mm and a length of 6 mm. The coil carries 40 wraps of 22 gauge, insulated copper wire. The electromagnetic coil has a resistance of 0.34 Ω. The supporting structure of the equipment is made of acrylic.

The current through each electromagnetic coil is independently controlled by a microcontroller board (RoboClaw 2x5 A Motor Controller, Orion Robotics) and sends pulse width modulated (PWM) signals through the coils. A continuous 5 A supply current is independently modulated with 10-bit resolution. The effective current through the coil is calculated by $I = \frac{PWM}{512} I_{max}$.

The robots are magnetic disks of rubber impregnated with ferrite magnetic material and have a diameter of 2.0 mm and a thickness of 0.25 mm. The magnetization of the magnet is not affected by the applied field. The robots are placed in a water-filled chamber at the center of the four coils. The robots float on the surface of the water, restricting motion of the robots to the plane of the surface. This surface is assumed flat at the center far from the edge of the chamber. The air-water interface minimizes translational drag in the plane and rotational drag about the z-axis resulting in a system that is very sensitive to small changes in current through the coils.

One stationary camera provides visual feedback from the top. The camera, Point Grey Flea 3 Monochrome, is fitted with a Cosmicar Television Lens 6mm resulting in a frame size of 640 x 480 pixels with an effective pixel size of 0.207 mm^2. Position feedback is provided by visual processing using OpenCV library [8]. A blob detector is used to locate the position of the magnets and correlation of position between frames is used to differentiate the two magnets. The system is controlled through C++ and Python using Robot Operating System (ROS).

A trajectory controller to calculate the desired forces, $\vec{F}^{des}$, uses a PID controller with

a feed-forward acceleration term,

$$\vec{F}^{des} = K_p\left(\vec{x}_T - \vec{x}\right) + K_d\left(\vec{v}_T - \vec{v}\right) + K_i \int \left(\vec{x}_T - \vec{x}\right) dt + \vec{a}_T M \tag{6.11}$$

where M is mass of the robot, the subscript T indicates the desired position, x, velocity, v, and acceleration, a, from the precomputed trajectory; without the subscript indicates the actual position or velocity. K_p, K_d, K_i indicate the proportional, derivative and integral gains respectively.

For straight line trajectories, a quintic polynomial position function is fit between waypoints to ensure smooth accelerations. For circular trajectories, a constant angular velocity trajectory is used. Position feedback is processed and controller commands computed at 100 Hz, while the current through the coils are updated at 10 Hz.

To parameterize the system, trajectories of one robot resulting from a known current through one coil were captured in open loop. A resultant force profile of the robot was extracted from the trajectory and an effective radius of the coil, R_{eff}, and effective magnitude of the magnetic dipole moment, $|m_{eff}|$, were computed. These values are used to compute the magnetic field. By empirically solving for these parameters, it ensures that the model matches the observed behavior of the system. The values used in the closed loop feedback experiments are $R_{eff} = 75\,\text{mm}$ and $|m_{eff}| = 35.8\,\mu\text{Am}^2$.

6.2.5 Experimental Results

Due to the sensitivity of the magnets to small changes in the magnetic field, as discussed in Section 6.2.4, small currents can generate rotation and translation of the robot. The applied field magnitudes are 10-400 μT. This is on the order of magnitude of Earth's magnetic field as evident by the consistent reorientation of the magnets when no current is applied. This causes a bias in the orientation of the magnet. Therefore, the expression for the magnetic dipole moment, expressed previously by equation (5.10), is written as the sum of the applied

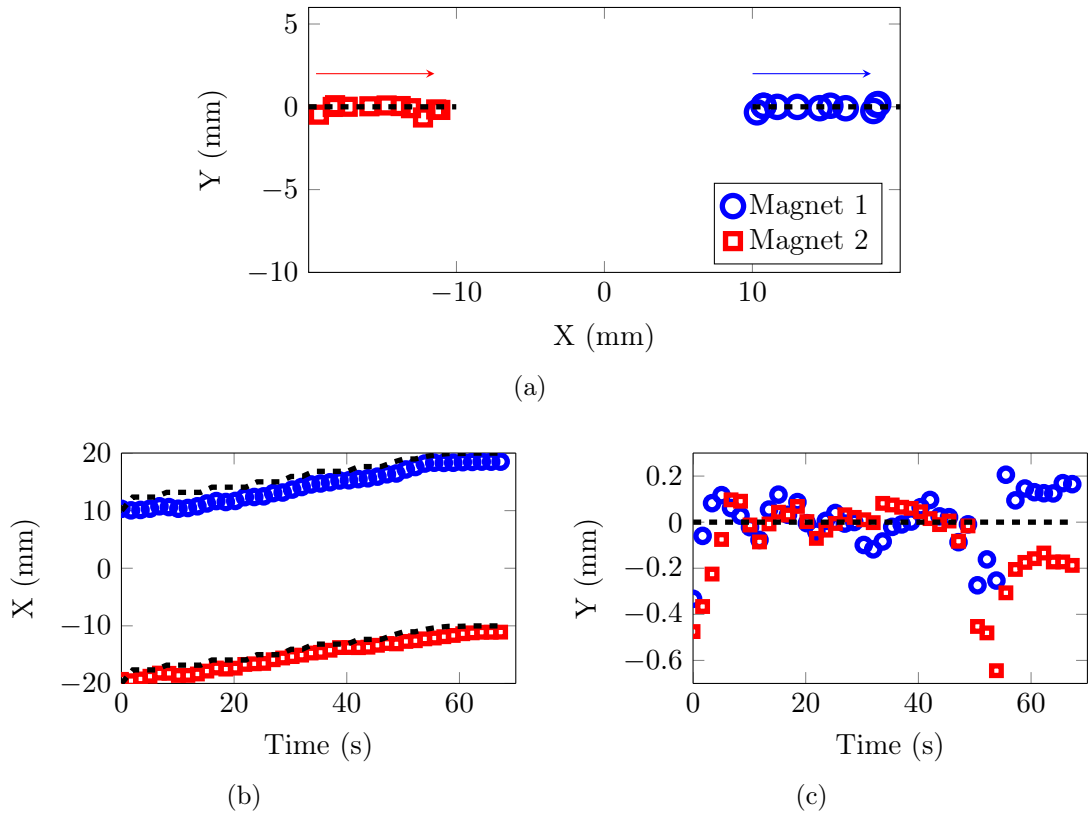

Figure 34: Experimental result demonstrating the same velocity for two robots, colored markers represent the actual trajectory and the dotted black lines represent the desired trajectory. (a) Trajectory of magnets. (b) Time series of x-position. (c) Time series of y-position. (See Supplementary Video.)

magnetic field by the coils, $\vec{B}$, and Earth's magnetic field, $\vec{B}_{Earth}$:

$$\vec{m} = \frac{|m|}{|\vec{B}(x,y) + \vec{B}_{Earth}|}(\vec{B}(x,y) + \vec{B}_{Earth}) \tag{6.12}$$

The magnitude and direction of Earth's magnetic field is empirically derived as $\vec{B}_{Earth}$ = -40 $\hat{i}$ μT in the fixed frame of the workspace.

Waypoints are precomputed for each trajectory, with each waypoint defining a desired position, velocity and acceleration. The control sequence updates the desired position, velocity and acceleration to the next waypoint once the magnets are within a threshold radius from the desired waypoint. A threshold radius of 1.5 mm is used on the magnets that are moving along trajectories in the experimental results in Figure 34 and 35.

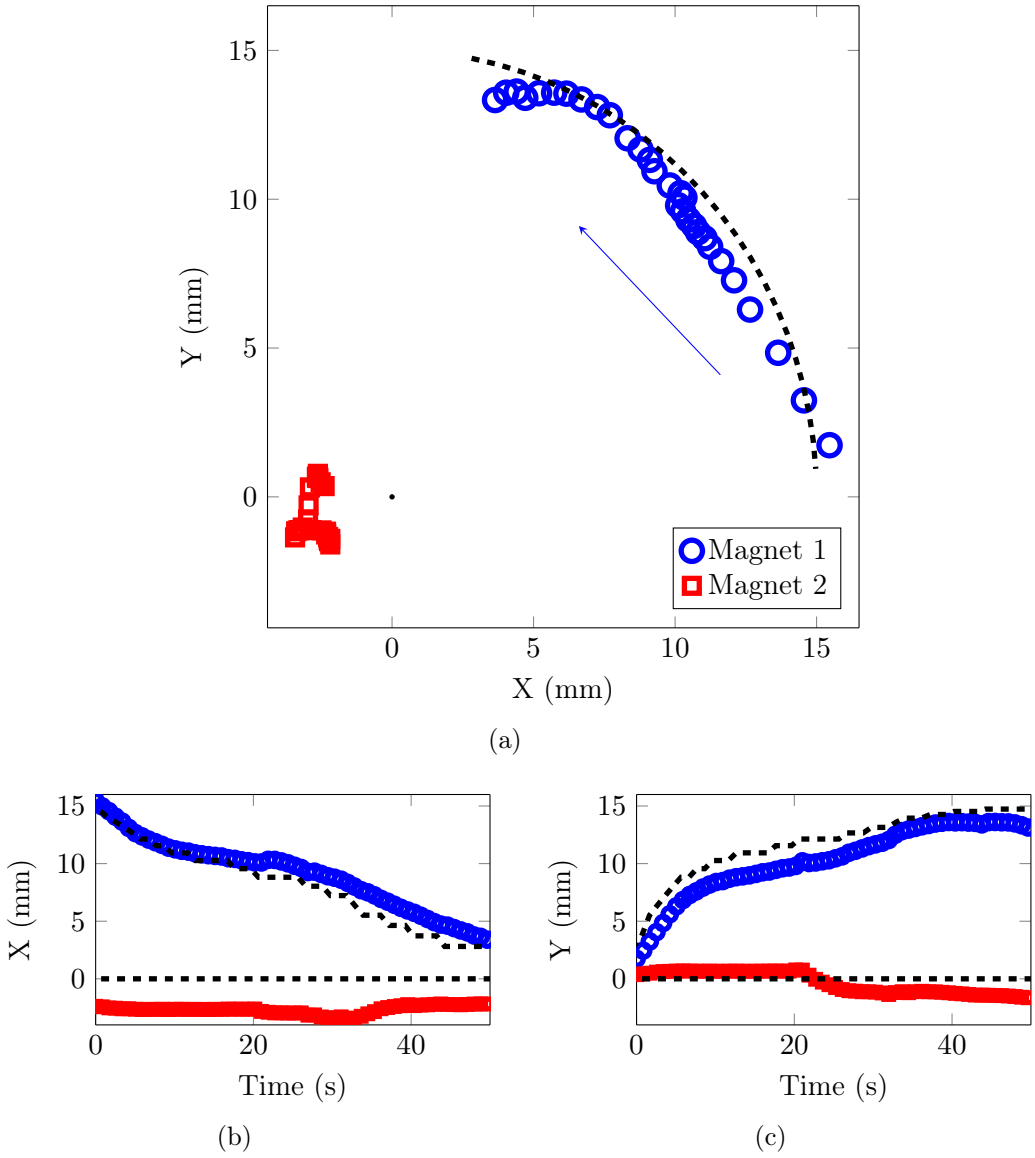

Figure 35: Experimental result demonstrating varying trajectories, solid colored lines represent the actual trajectory and the dotted black lines represent the desired trajectory. (a) Trajectory of magnets. (b) Time series of x-position. (c) Time series of y-position. (See Supplementary Video.)

A unique feature of this system is the ability to exert the same forces on magnets at different locations so that magnets can move with the same velocity in addition to being able to move along differing trajectories. Figure 34 shows a trajectory where both magnets are moving at the same velocity in the positive x-direction. Figure 35 shows a trajectory where one robot is held stationary as the other is moving in a counter-clockwise arc with a radius of 15 mm. Our method uses homogeneous robots that are identical in all aspects and can accomplish independent direction control of robots without the use of a specialized substrate.

6.2.6 Relevance to Microscale Systems

In our experimental system where the Reynolds number is on the order of 10^{-1}, inertia causes the magnet to drift slightly after the electromagnetic coils are turned off. This makes the control problem challenging. As the system is scaled down to the microscale, we can qualitatively consider the governing physics equation to begin to understand feasibility of our proposed control strategy. Abbott et al. [2] provided a scaling analysis for pulling a magnet, of diameter d, with gradients generated by two opposing current coils at a separation distance, $2L$. The radius of the coils are assumed to be the optimal size for maximizing the gradient at the center between two coils, $R = \sqrt{\frac{2}{3}}L$. The magnetization of the robot and the current through the coils enter linearly into the maximum velocity and force, so the results are normalized to these quantities. They show that the gradient of the magnetic field scales with coil separation as $\sim L^{-4}$, while maximum force scales as $\sim d^3$. Forces scale favorably as the system reduces in size as the electromagnetic coils move closer together and the magnetic robot reduces to microscopic size as long as scaling is comparable.

At microscale, viscous forces will dominate as inertial forces become insignificant. Drag force on the magnet in macroscale is modeled as quadratic in velocity, whereas in viscous flows drag force is linear in velocity. Experimentally, when a magnetic field gradient is applied, the magnetic robot will reach terminal velocity almost instantaneously, and similarly will come to a halt when the magnetic field gradient is removed.

To understand how the magnetic fields will scale to the microscale, we simulate a low

Reynolds number system. The simulation is analogous to the simulation described in Section 6.2.3 with the geometry of the electromagnetic coils and magnet reduced by 2 orders of magnitude. The drag force is computed using Stokes' drag,

$$\vec{F}_{drag} = -3\pi\eta d\vec{v} \tag{6.13}$$

where η is the dynamic viscosity of water. This equation is used to compute the desired force for a desired velocity. A similar prescription of desired velocities is precomputed at waypoints for a given trajectory and an open loop controller is simulated for a system without disturbances. Simulation results are shown in the video included in the Supplementary Video. While our simulation is idealized, these results suggest that the force control algorithm introduced here for multi-magnet control is relevant for microscale systems where inertial forces are dominated by viscous forces. An experimental implementation would need to include a closed loop feedback system to overcome disturbances unique to microscale systems.

At smaller scale a variety of interaction forces become important to consider, such as surface interactions, electrostatic forces and van der Waals forces as the order of magnitude of these forces are comparable to manipulation forces. In our case, where robots are being manipulated at a fluid interface, we take advantage of the surface interaction forces to stay confined to the fluid interface and away from solid surfaces in order to minimize electrostatic and van der Waals forces, which are prevalent at solid interfaces. A controller capable of handling external disturbances unique to microscale manipulation, such as those caused by convective flows due to temperature fluctuations, is needed.

6.2.7 Discussion

The mapping from force to current is not a one-to-one mapping, and there can be many solutions for current given a set of positions and desired forces. Different solutions will result in the same force exerted but with the robot in varying orientations. The system of equations (6.6) used in our implementation does not guarantee smooth orientation of

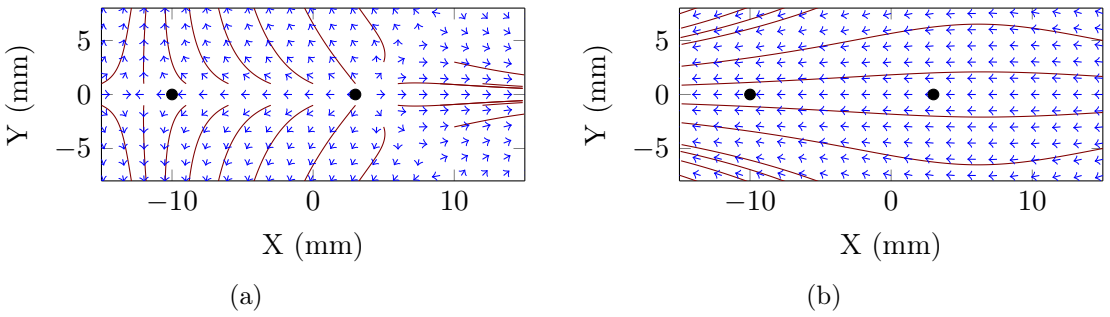

Figure 36: Multiple solutions satisfy the same constraints on the position of robots and desired forces. $\vec{x}_1 = [-10, 0]$ $\vec{x}_2 = [3, 0]$ $\vec{F}_{1,des} = [-3, 0]$ $\vec{F}_{2,des} = [-1, 0]$. Arrows indicate unit force vector field and lines show force streamlines. (a) $\vec{u} = [0.45, -2.93, -1.93, 2.93]$ A. (b) $\vec{u} = [-0.17, 0.05, 0.02, -0.05]$ A.

the magnets and constrains only force. Large variations in current between updates cause high rotational velocity, drastically changing the orientation of the robot and can lead to momentary instability, resulting in deviation from the desired trajectory. This is shown in the y-position time series plot at time 50 seconds for the linear trajectory case, Figure 34(c), and can also be observed in the Supplementary Video.

Figure 36 shows the normalized force vector field for two solutions to the same force and position constraint. For this control problem, given the assumptions and approximations used, it is important to choose the most robust solution. There are many different measures of robustness; one method would be to consider the spatial derivative of the force around the solution and to consider critical points in the force vector field, where the spatial derivative of the magnetic field is zero and force on the magnet is zero [75]. In the example in Figure 36, solution (b) would be a more robust solution than (a). In solution (b) both robots are on a stable manifold such that small perturbations in position would still exert a force on the robot in the desired direction; whereas in solution (a), there is an unstable critical point close to the location of the robot at [3,0] mm such that a slight error in the positive x-direction would lead to a force being exerted in the opposite direction than desired. The existence of many suboptimal solutions at each control update makes this a challenging problem. The Levenberg-Marquardt algorithm as implemented in the Eigen libraries for C++ [32] returns solutions that are dependent on the initial value provided. One method

of ensuring robust solutions is by initializing the Levenberg-Marquardt algorithm with a robust solution for a similar problem. In both the example trajectories in Section 6.2.5, the currents were precomputed at each waypoint for the desired force.

An additional source of uncertainty is the orientation of the magnet. The controller assumes that the robot reorients instantaneously, however, there is a delay due to non-zero rotational drag of the disk. For improved force control it would be beneficial to track the magnet's orientation or implement both field and gradient control [56]. Additionally, for trajectory planning, geometric analysis of singularities must be considered to ensure feasibility and also to select trajectories that are robust given the electromagnetic coil configuration [79].

6.3 Simulations of Multi-Magnet Control

To control multiple magnets independently using a set of stationary electromagnetic coils, large variations in the magnetic field across the workspace are created. This translates to large field-gradients and therefore forces being exerted on the magnets. As a result of these variations in the magnetic field, a small deviation in position and orientation of the magnetic robot can lead to varying forces being applied ot the robot. Therefore, it is important to have an accurate mapping between coil current input and the spatial properties of the magnetic field generated.

In simulation, where the system is idealized and we have perfect information about the state of the system, we can develop controllers that might be able to be used for such a system. Moreover, we can visualize the accuracy needed in the shape of the magnetic field to obtain the desired force outputs.

6.3.1 Simulation Design

We simulate a system that models the dynamics of the robot using the linear and rotational drag coefficients derived empirically in Chapter 5. In our previous simulation in Section 6.2, we assumed that the magnetic robot immediately aligned to the magnetic field and therefore the orientation of the robot was a function of the applied current, an assumption

that is relevant at the microscale. In this simulation we relax the constraint that assumes no torque in the system and instead allow the robot to rotate to align to the magnetic field. As illustrated in the empirical studies in this chapter, allowing the robot to rotate more accurately describes the observed behavior.

By treating the orientation of the magnet, $\vec{m}$, as a known quantity that can be determined by visual feedback of the system, the force exerted on each of the robots, $\vec{F}$, by the applied field is a linear function of the applied currents. (The equations are repeated here for clarity.)

$$\begin{aligned} F_{1,x} &= [m_{1,x}, m_{1,y}]\mathbf{D}_{1,x}\vec{u} \\ F_{1,y} &= [m_{1,x}, m_{1,y}]\mathbf{D}_{1,y}\vec{u} \\ F_{2,x} &= [m_{2,x}, m_{2,y}]\mathbf{D}_{2,x}\vec{u} \\ F_{2,y} &= [m_{2,x}, m_{2,y}]\mathbf{D}_{2,y}\vec{u} \end{aligned} \tag{6.6}$$

Where $\vec{u}$ is the 4-element column vector of the applied currents through each coil and $\mathbf{D}_{i,j}$ is the 2×4 matrix form of the gradient of the magnetic field for the i-th robot in the j-th direction. $\mathbf{D}_{i,j}$ is a function of the position of the robots. The system of equations (6.6) can also be expressed in a matrix form where the force can be written as a function of the magnetic field gradient,

$$\begin{aligned} \vec{F} &= \begin{bmatrix} m_{1,x} & m_{1,y} & 0 & 0 & 0 & 0 \\ 0 & m_{1,x} & m_{1,y} & 0 & 0 & 0 \\ 0 & 0 & 0 & m_{2,x} & m_{2,y} & 0 \\ 0 & 0 & 0 & 0 & m_{2,x} & m_{2,y} \end{bmatrix} \begin{bmatrix} \frac{\partial B_{1,x}}{\partial x} \\ \frac{\partial B_{1,x}}{\partial y} \\ \frac{\partial B_{1,y}}{\partial y} \\ \frac{\partial B_{2,x}}{\partial x} \\ \frac{\partial B_{2,x}}{\partial y} \\ \frac{\partial B_{2,y}}{\partial y} \end{bmatrix} \\ &= \mathcal{F}(\vec{m})\,\mathbf{G} \end{aligned} \tag{6.14}$$

where the function $\mathcal{F}(\vec{m}_1, \vec{m}_2)$ packs the components of the magnetic dipole moment of each robot into a matrix so that it can be multiplied by the vector of the field-gradient, $\mathbf{G}$.

The torque can be written in matrix form as

$$\vec{\tau} = \begin{bmatrix} -m_{1,y} & m_{1,x} & 0 & 0 \\ 0 & 0 & -m_{2,y} & m_{2,x} \end{bmatrix} \begin{bmatrix} B_{1,x} \\ B_{1,y} \\ B_{2,x} \\ B_{2,y} \end{bmatrix}$$

$$= \mathcal{S}\left(\vec{m}\right)\mathbf{B} \tag{6.15}$$

where the function $\mathcal{S}(\vec{m}_1, \vec{m}_2)$ packs the components of the magnetic dipole moment of each robot into a cross product matrix so that it can be multiplied by the vector of the magnetic field, $\mathbf{B}$.

The field, $\mathbf{B}$, and gradient, $\mathbf{G}$, are a function of both position and current. We can separate the dependence by introducing two variables

$$\begin{aligned} \mathbf{B}\left(\vec{x}, \vec{u}\right) &= \mathbb{B}\left(\vec{x}\right)\vec{u} \\ \mathbf{G}\left(\vec{x}, \vec{u}\right) &= \mathbb{G}\left(\vec{x}\right)\vec{u} \end{aligned} \tag{6.16}$$

where $\mathbb{B}$ is the current normalized vector and $\mathbb{G}$ is the current normalized field gradient vector, which is a function of the position of the two robots.

In our system, there are 6 degrees of freedom and 4 current inputs. Therefore, the system is under actuated. In the controller we simulate, we control the force exerted at each magnet.

The system inputs are calculated using equation (6.14) and inverting the matrix $\mathcal{F}(\vec{m})\mathbb{G}(\vec{x})$,

$$\vec{u} = \text{inv}\left(\mathcal{F}\mathbb{G}\right)\vec{F} \tag{6.17}$$

$\mathcal{F}\mathbf{G}$ is a 4×4 matrix which is a function of the pose of the robots. The manipulation matrix, $\mathcal{F}\mathbf{G}$, maps the current inputs to the system to the force exerted at each robot and is analogous to the Jacobian of the system. A solution to the desired force exists as long as $\mathcal{F}\mathbf{G}$ is invertible. The determinant can be used to determine if $\mathcal{F}\mathbf{G}$ is invertible.

We simulate constant velocity trajectories defined by equally spaced waypoints. The desired force is calculated using a proportional controller with a feed forward term,

$$\vec{F}^{des} = K_p \left(\vec{x}_T - \vec{x}\right) + K_d \vec{v}_T \tag{6.18}$$

where the subscript T indicates the desired position, x, and velocity, v along the trajectory and K_p and K_d are the proportional and derivative gains respectively. The actual velocity at time T is not used in this formulation because a Stokes flow environment is assumed, in which case inertia is negligible and the velocity varies linearly with force.

At each controller update, the pose of the magnets is used to compute the matrix $\mathcal{F}\mathbb{G}$. The determinant is calculated to ensure that the matrix can be inverted. If the determinant is non-zero, equation (6.17) is used to calculate the desired current to exert the desired force. The vector of current inputs is applied to the system for a fixed time step, $\frac{1}{freq}$, based on the frequency update of the controller. MATLAB is used to simulate the system. The differential equation solver function *ode45* is used to calculate the pose of the magnet as a result of the applied current and the dynamics of the system defined by equations (6.14), (6.15).

6.3.2 Simulation Results

For a given set of trajectories, the stability of the system is a function of the initial conditions of the system, specifically the orientation of the magnetic dipole of each robot.

Figure 37 shows a simulation of the robots moving toward each other along the edges of a rotated V. The robots are initialized at the start of the trajectory oriented with the magnetic dipoles aligned with Earth's magnetic field to simulate a state of all coils off. Figure 37a shows the desired trajectory of the 2 robots in red, with the start indicated by green circles. The unit-vector fields show the magnetic field (blue) and the applied force assuming the magnet aligns with the magnetic field (red). The force vector field is calculated assuming that the magnet is oriented with the applied magnetic field. The dotted lines indicate the manifolds of the force field, with the green line indicating a stable manifold and the purple

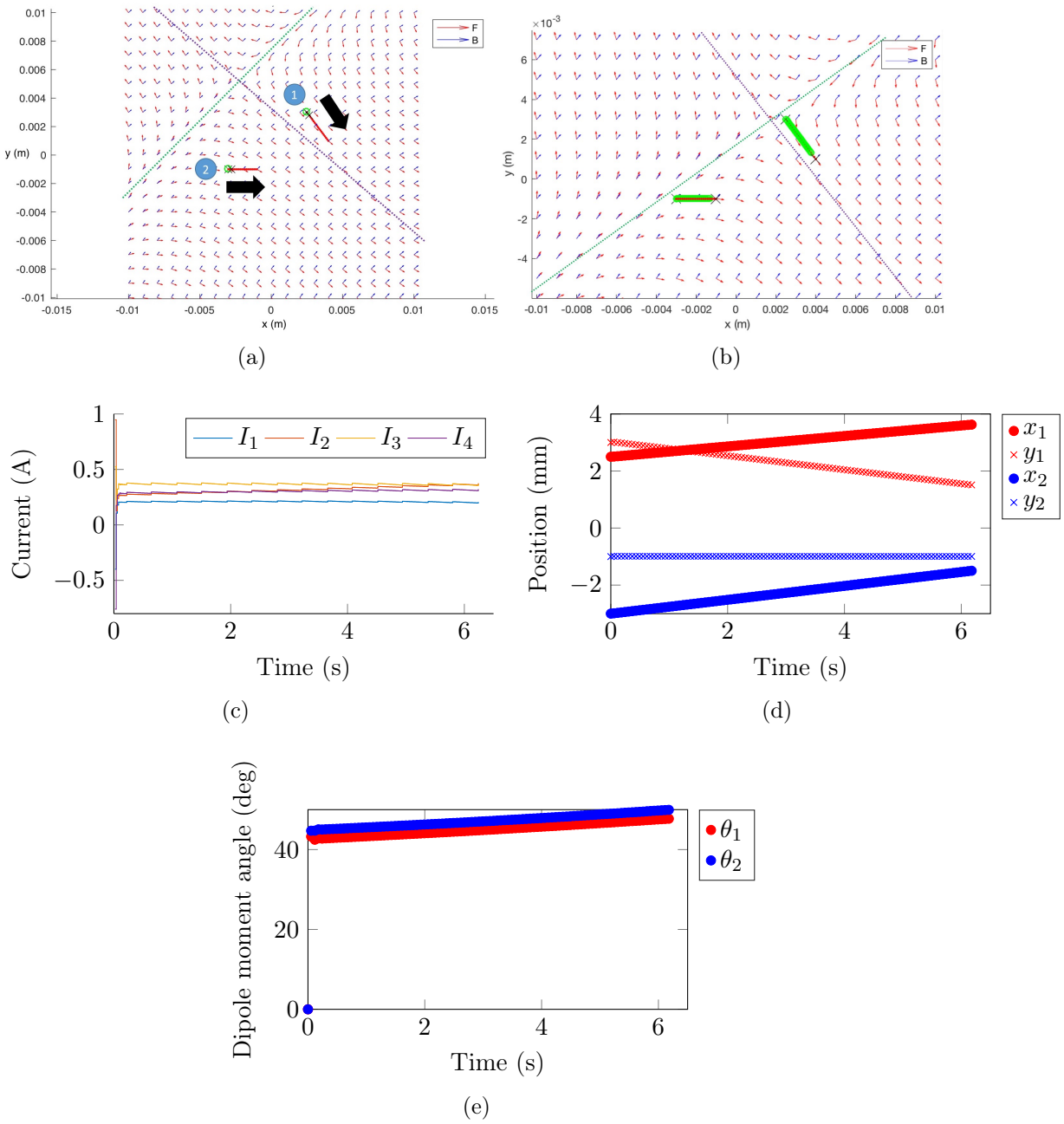

Figure 37: Simulation results of 2 magnetic robots moving toward each other. (a) Trajectory of the robots and the magnetic and force field applied at time = 0.04s, (b) Time series of the applied current, (c) Time series of position of the robots, (d) Time series of the angle of the magnetic dipole of the robot.

line an unstable manifold.

The time series plots show that, with the exception of the first controller input time interval, the position and angle of the robot is smooth. The applied currents are also stepwise continuous, larger steps indicate the transition between waypoints. The smoothness in the pose of the robot suggests that the robot is staying on the same side of a manifold. Far from the manifold, the gradient of the force field is uniform. Figure 37b shows the applied field at time 7.66 s, at the end of the trajectory, the magnets are still on the same side of the manifold throughout the trajectory, the critical point shifts continuously to apply the desired force.

Once the magnetic dipole aligns with the torque minimizing configuration for the desired force, the angle of the magnetic dipole and position changes smoothly. To understand how this occurs, we take a look at the dynamics of the robot at time 0 - 0.02 s, the first time step for the update rate of the simulation, 50 Hz, in Figure 38. Here we look into detail at the dynamics of robot 1, which starts at coordinates $[2.5, 3]$ mm. At time 0 s, the magnetic dipole is aligned to Earth's magnetic field at $0\,^\circ$. The current that is applied initially moves the robot in the desired direction along the red line, however as the robot rotates to align to the applied magnetic field, the robot's trajectory deviates from the desired trajectory. In this case, it moves in the positive y-direction, which is opposite of the desired trajectory. After a duration of 0.02 s, the robot has moved 22 μm to coordinates $[2.5009, 3.0220]$mm and is oriented at an angle of $45.3\,^\circ$. The currents at the next controller update generates a field that closely aligns to the angle of the robot and the robot moves toward the desired waypoint as desired. In this example, from this time onward, the behavior of the robot and the inputs into the system are smooth and the torque exerted on the robot is small.

By taking a closer look at the behavior of the robot at the start of the simulation, we can gain an appreciation of how sensitive the behavior of the robot is to the orientation of the magnetic dipole. This highlights the importance of the accuracy in the sensing of the pose of the robot as well as the model for the magnetic fields.

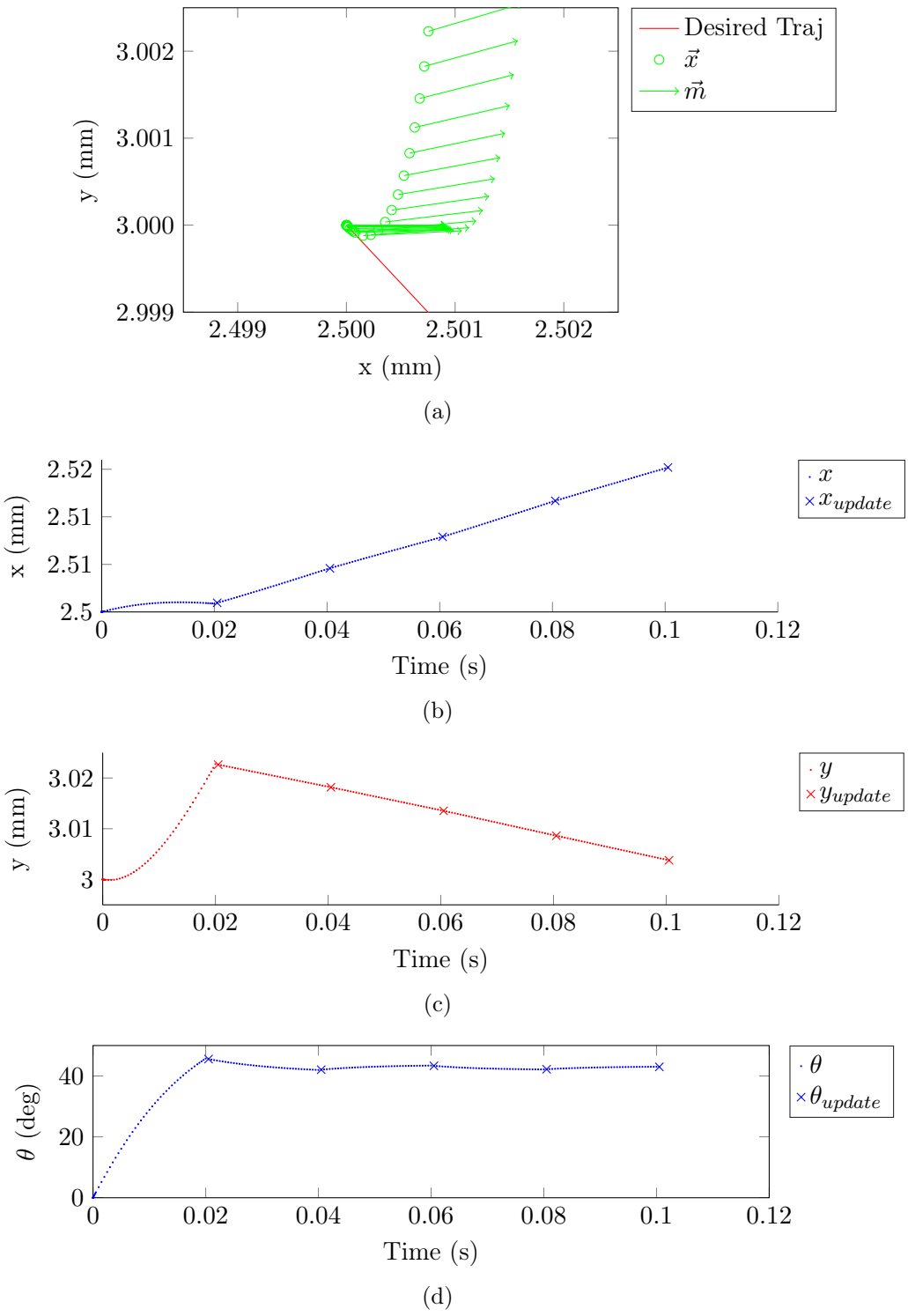

Figure 38: A closer look at the start of the simulation of 2 magnetic robots from the first controller input (Same as in Figure 37. (a) Trajectory of robot 1 at time = 0s, (b) Time series of the x position of robot 1, (c) Time series of the y position of robot 1, (d) Time series of angle of the robot 1.

6.4 Conclusion

In this chapter, we provide a model for controlling magnets using the spatially varying gradient of the magnetic field close to the electromagnetic coil and the superposition of the independent fields generated by several stationary electromagnetic coils. Firstly, we demonstrate independent control of multiple permanent magnets along the axis of electromagnetic coils. A model for local magnetic fields, generated by superposition of the field generated by the electromagnetic coils and neighboring permanent magnets, is used to compute resultant force on each permanent magnet. This model is verified through a one-dimensional experimental system where we demonstrate both open-loop and closed-loop visual feedback control of the position of two magnets with two electromagnetic coils; and in simulation the positions of three permanent magnets with three electromagnetic coils. Furthermore, we have contributed a theoretical framework to achieve independent position control of two identical magnets in a planar system. We analyze this method in simulation and experiment in order to show that independent forces can be applied on each robot. Experimental results demonstrate trajectory following using visual feedback. These results are relevant for microscale systems where inertia is negligible. Furthermore, using empirically derived parameters for the dynamics of the robot, a simulation for controlling two identical robots where inertia is not negligible is demonstrated. Our results shows that in special cases, it is possible to control two robots independently. We find that the behavior of the robot is dependent on the initial orientation of the robot and that this controller minimizes torque over time. These results highlight the need for an accurate map of the magnetic field in order of achieve high resolution manipulation given that the controller inputs create critical points in the force field close to the position of the robots. We may also consider strategies for designing trajectories to minimize torque. This control scheme has potential applications in micromanipulation for automated high-throughput biological experiments and use inside microfluidic channels for analysis and microassembly.

Chapter 7

Applications to Assembly

At the microscale, additive manufacturing techniques to build structures from bottom up has numerous advantages such as using only the materials that are necessary for the structure and being able to create and reconfigure assemblies from the same simple building blocks. When considering assembly at the microscale, one can take advantage of physical phenomenon that dominate at these length scales.

This chapter explores a micro assembly strategy that combines passive particle assembly in soft matter with robotics to develop new means of controlled interaction. In capillary assembly, particles distort fluid interfaces and move in directions that minimize the surface area. We propose a robot that serves as a programmable source of fluid curvature and allows the collection of passive particles. We study of the interaction between the robot and the passive particles and demonstrate automated assembly.

The research in this chapter was originally published in [83].

7.1 Introduction and Related Work

Micro assembly is the manipulation and assembly of sub-millimeter sized parts with high-resolution capabilities. Micro assembly has applications in many fields including micro surgery, microrobotics, biological sciences, micro manufacturing and soft matter. The ability to manipulate with microscale precision to assemble components is important in all of

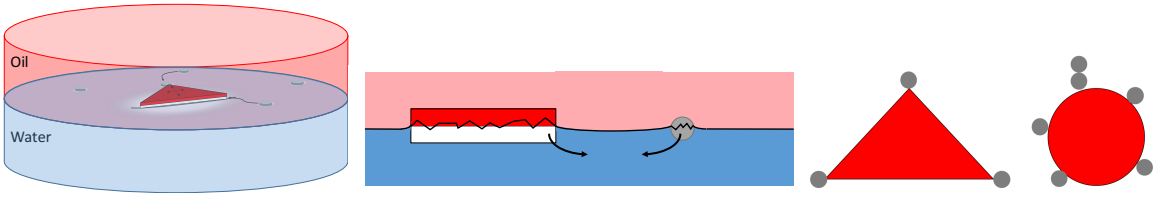

Figure 39: Magnetic robots can be used to direct assembly of passive micro structures using capillary effects at fluid interfaces. (a) The actuated robot (the triangle) can selectively assemble passive structures (shown as circles) to predetermined locations. (b) The curvature of the fluid interface created by the robot and the passive particle result in an attractive force that binds the robot and particle. (c) Top view of robots. Differently shaped robots will have different types of effect on the surface curvature and can direct particles with specificity to assemble to corners or more randomly around a circle.

these applications. To address these challenges in micro manipulation, a wide range of methods have been explored including probing payloads using a micro manipulator [10], using microfluidics to manipulate cells [33] and using capillary interactions to build tissues [24].

In recent years, magnetic manipulation has attracted increasing attention because of several key associated advantages. Magnetic manipulation allows control of the robot with high degrees-of-freedom, without the need for line-of-sight interaction or tethers. Additionally, magnetic manipulation allows selective addressability, in contrast to electric fields. This allows the robot to function in small and difficult to reach places. Additionally, magnetic fields are well known to be safe to biological cells and tissue, and are widely used in the medical field [25].

A variety of different strategies for magnetic micro actuation in fluidic environments using magnetic fields generated by electromagnetic coils have been demonstrated [2]. Image based position control of a single magnetic particle at an water-air interface is explored in one-dimension by Dkhil et al. [22] and in a plane by Keuning et al. [37]. In work that combines magnetic manipulation and capillary interaction, Grosjean et al. [31] use three soft ferromagnetic beads powered by externally applied magnetic fields to swim across a water-air interface. The beads were collectively controlled along trajectories by oscillating the magnetic field to break the symmetry in the system. One of the advantages of this system is that the structure is self assembled by capillary interactions, making scaling the system to

micro-scale applications feasible, as precise manipulation for assembly of the system is not required. This system differs from our work in that all particles in the system are magnetic and locomotion is based on non-reciprocal motion.

Micro manipulation and assembly of passive parts using magnetic actuation has been demonstrated using a variety of methods. Ng et al. [49] combine a mixture of magnetic and non-magnetic gears assembled by capillarity at a perfluorodecalin-air interface. An external magnetic source is used to rotate the magnetic gears and torque is transferred to the non-magnetic gears by a combination of mechanical interaction, hydrodynamic shear and capillarity. Martel et al. [43] use a swarm of magnetotactic bacteria to manipulate micro bricks to assemble structures. While this method may be effective, precise control of the micro bricks is challenging. Diller et al. [78] used a magnetic microrobot to manipulate building blocks submerged in fluid in 2D and 3D settings. In this example, heterogeneous building blocks of rigid and soft materials were combined to create complex functional materials. However, while the structures could be reconfigured with a resolution of tens of microns, the robot was teleoperated, and manipulation of the building blocks was challenging, as only pushing motions were possible, and no grasping or pulling of objects could be achieved with the cube shaped microrobot.

In soft matter, assembly of colloids and other microscale objects lends fundamental insight into collective behaviors that emerge from many-body interactions, and provides a route to form reconfigurable materials. Magnetized ferrofluids comprising suspensions of ferromagnetic particles have been widely studied in this context [45, 80]. There are other means of organizing colloids that do not rely on the usual electromagnetic fields. One important means exploits the energy stored by distortions made by particles in their soft matter hosts. Capillary interactions are an example; particles attached to fluid interfaces deform those interfaces. The energy stored from this deformation is the product of the surface area of the distortion and surface tension. When surface distortions from neighboring particles overlap, particles interact and assemble [7]. More generally, when particles distort curved interfaces, they move along principle axes to sites of high curvature to lower the

surface area, and hence the energy, of the interface via curvature capillary migration [13, 64, 87]. The particles themselves can be arbitrarily complex, for example, cell-laden microgel particles trapped at liquid interfaces were assembled by Du et al.[24] into biomimetic 3D tissues.

In this paper, we demonstrate that an untethered, independently actuated magnetic robot can serve to control the surface deformation source at a liquid interface, Figure 39. Passive particles located at that interface interact with the robot via curvature capillary migration, and are attracted to its edges. Moreover, by tailoring robot geometry, preferred sites for particle assembly are defined, e.g. at robot corners, where associated interface curvatures are high, Figure 39c. The ability to move the robot allows specific particles to be selectively assembled at predictable sites in a way which would not occur without the ability to manipulate the robot. Furthermore, the bulk motion of the assembly of passive particles can be manipulated precisely as a result of being docked to the magnetic robot.

7.2 Capillarity Background

Capillary interactions are ubiquitous among particles on fluid interfaces. Particles can distort interfaces because they are heavy [14]. Particles of negligible weight can also distort interfaces, for example, if they have rough surfaces, patchy wetting [51] or complex shapes [64, 66]. Any of these cause the contact line, where the interface meets the particle, to be undulated. The undulated contact line deforms the interface around the particle. The capillary energy for an isolated particle is given by the product γA, where γ is the interfacial tension and A is the area associated with the particle's distortion. When neighboring particles' distortions overlap, the interfacial area decreases and particles approach each other to minimize interfacial energy.

Curved interfaces offer special opportunities for directing capillary assembly. For heavy particles, particles migrate downhill to lowest sites on the interface. For particles with undulated contact lines, the interaction is more complex. The leading order mode of the interface distortion made by such particles is a quadrupolar mode in polar coordinates (r, ϕ)

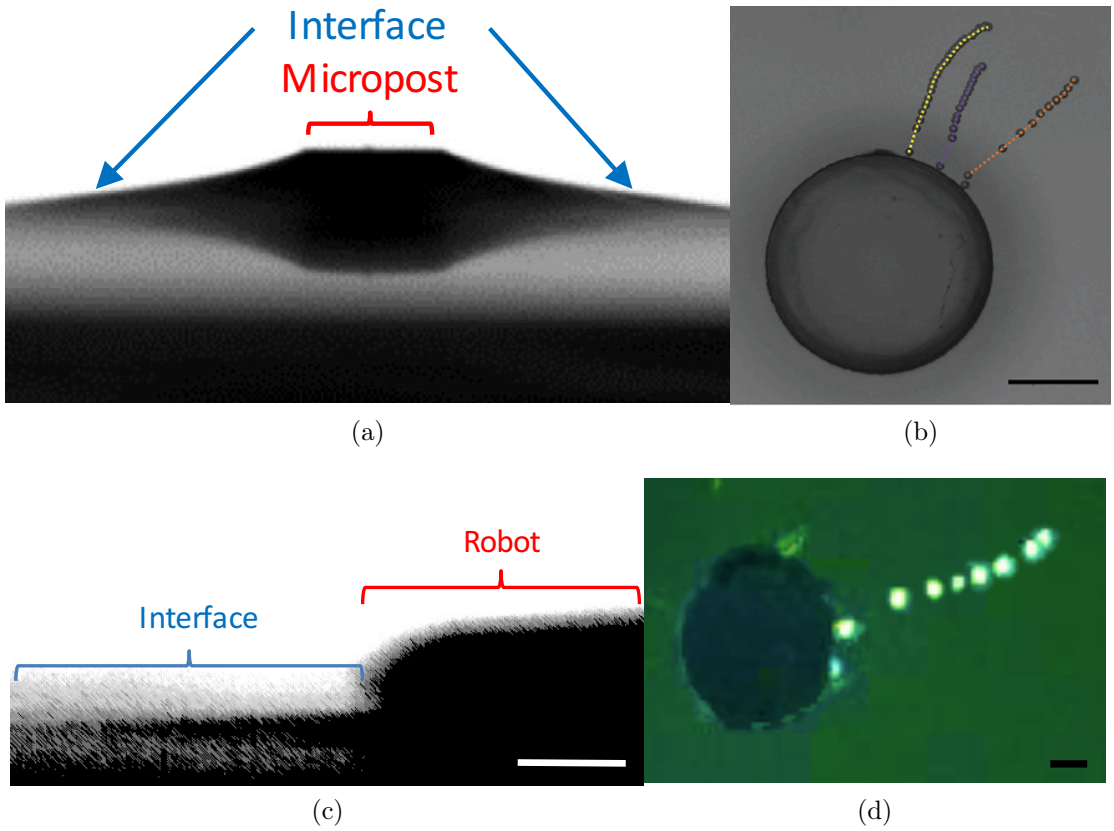

(a) (b)

(c) (d)

Figure 40: Capillary driven assembly on a curved interface. (a) Side view of the curved interface for a micropost of diameter 250 μm [88]. (Reprinted with permission.) (b) Time-stamped image (Δt=1 sec) showing trajectory of microsphere migration on a stationary curved fluid interface pinned around a micropost. Scale bar is 100 μm [64]. (Reprinted with permission.) (c) Curved interface at the edge of the robot. Scale bar is 250 μm (d) Time-stamped image (Δt=1 sec) showing trajectory of bead assembling to a mobile magnetic robot, with position of the bead taken in the frame of the robot. Scale bar is 250 μm.

centered on the particle, given by $h_{qp}(a^2/r^2)\cos 2\phi$, where h_{qp} is the magnitude of this mode and a is the characteristic length of the particle. In the limit of small interface slope, the shape of the fluid interface near the particle can be decomposed into two parts:

$$h_{host} = \frac{r^2 H}{2} + \frac{\Delta c}{4} r^2 \cos 2\phi \tag{7.1}$$

where $2H$ is the sum of the principal curvatures, and Δc, the deviatoric curvature, is the difference in principal curvatures. When a particle with an undulated contact line attaches to this interface, the associated capillary energy, E_{curv}, owing to finite Δc is [87]:

$$E_{curv} = E_0 - \gamma \pi a^2 (\frac{h_{qp}\Delta c}{2}), \tag{7.2}$$

where the first term is a constant. The associated capillary force, F_{curv}, moves particles along gradients in the deviatoric curvature is:

$$F_{curv} = -\nabla E_{curv} = \gamma \pi a^2 \frac{h_{qp}}{2} \nabla(\Delta c) \tag{7.3}$$

This has been observed for various particle shapes, including cylinders, disks and spheres [13, 64, 88]. For example, we can mold interface curvature by pinning a fluid at the edge of a micropost, Figure 40a. Particles on this surface migrate to sites of high deviatoric curvature owing to this curvature cue, Figure 40b. However, thus far, this has been studied only near fixed curvature cues.

7.3 System Design

Interface deformations made by passive microparticles decay rapidly, within a few particle radii. Deformations made by fixed curvature cues also have a limited spatial range, so they can only assemble particles in their vicinity. Therefore, a mobile curvature cue is needed to collect particles from desired locations. Furthermore, control over the curvature cue shape, such as corners, can define sites of high curvature to promote assembly at well defined sites. Moreover, a mobile curvature cue can shuttle assemblies about an interface. Here, we design

a magnetic robot to be used as a mobile curvature cue to interact with passive microdisks and microspheres on fluid interfaces.

7.3.1 Magnetic Robots

The magnetic manipulation system consists of four identical electromagnetic coils arranged around the square workspace at a distance of 115mm apart along the x- and y-axis. Each coil has an inner diameter of 51 mm and a length of 6 mm, with 40 turns of 22 gauge, insulated copper wire and has a resistance of 0.34 Ω. The support structure is made of acrylic.

Each electromagnetic coil is independently controlled using a microcontroller board (RoboClaw 2x5 A Motor Controller, Orion Robotics.) A pulse width modulated (PWM) signal is used to modulate a 5 A supply current with 16-bit resolution. The effective current through each coil is calculated as $I_{eff} = \frac{PWM}{32768} I_{max}$.

The magnetic robot is made of rubber impregnated with ferrite magnetic material. The rubber is heated, mixed with the ferrite magnetic material and poured into a sheet mold, which is exposed to a strong magnetic field to orient the poles of the magnetic material. Magnetic sheet stock was purchased and cut into different shapes for specific experiments. The disk is 2 mm in diameter and 0.25 mm in thickness. The right-angled triangle has sides of length 1.5 - 2.5 mm and a thickness of 0.25 mm. The ratio of the size of particles to the robots were chosen to achieve similar interactions observed in previous work with a stationary deformation source [64]. The magnetization of the magnet is not affected by the applied field and is assumed to be constant. The robot is placed in a chamber filled with water (bottom) and hexadecane (top.) Pre-wetting the robot with hexadecane facilitates trapping at the interface.

The robot and passive particles are trapped on to the water-oil interface by surface tension. Absent particles and the robot, the interface is assumed flat from the edges of the chamber. The presence of hexadecane reduces stray convection, allowing capillary interactions to dominate particle motion.

7.3.2 Passive Particles

The passive particles used in these experiments are glass spheres and SU-8 disks.

Spheres

The glass spheres have diameters ranging from 150-210 μm (Polysciences, Inc.) Particles are suspended in hexadecane, and gently introduced into the oil phase. The particles sediment until they encounter the water-oil interface, where they adsorb and become trapped.

Disks

The fluorescent disks are fabricated by photolithography, Figure 41. A negative-tone epoxy photoresist SU-8 (Microchem Corp.) is used to make microdisks. SU-8 2025 is aliquoted into an amber-colored glass bottle and mixed thoroughly with 0.1% by weight Rhodamine B, a red dye. This epoxy mixture is then spin-coated onto a silicon wafer with a 10 nm chromium-coat. After soft-baking, the wafer is exposed to UV light on a tabletop mask aligner (Model 100; OAI) through a photo mask with arrays of 150 μm diameter circles. The wafer is then transferred to a hot plate for post-exposure baking, which allows the UV-exposed regions to cross-link. Subsequently, the wafer is immersed in SU-8 developer to dissolve the unexposed region leaving only arrays of microdisks on the wafer. The resulting microdisks are 150 μm in diameter and 30 μm in height. These microstructures are then released from the wafer by dissolving the chromium coating with Nichrome etchant, and cleaned and dried before further use.

The disks are immersed in hexadecane, and then released into the top surface of the chamber using a pipette. Particles sediment, and attach to the interface.

7.3.3 Feedback Control

One overhead stationary camera provides visual feedback. The camera, Point Grey Flea 3 Monochrome, is fitted with a Navitar F1.4 6mm 1/2" M30.5 08C video camera lens resulting in a frame size of 1280 $\times$ 960 pixels with an effective pixel size of 0.207 mm^2. Position feedback is provided by visual processing using the OpenCV library [8]. The image is first

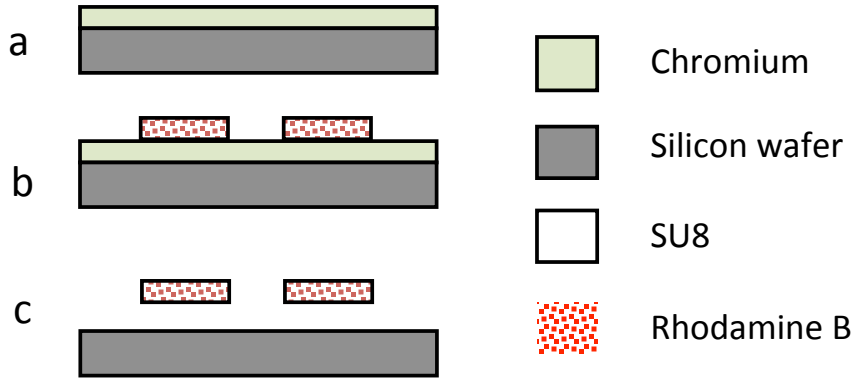

Figure 41: Disk fabrication by photolithography. (a) Sputter chromium on a clean silicon wafer. (b) Spin-coat negative epoxy on the wafer, expose to UV light, and dissolve away the non-exposed region. (c) Use chromium etchant to dissolve the chromium layer and clean disks with water and isopropanol.

converted to a binary image by thresholding and a blob detector is used to locate the position of the magnet. The system is controlled through C++ and Python using Robot Operating System (ROS).

7.4 Experimental Results

The reader is encouraged to view a video online [1] to see the experimental results.

7.4.1 Assembly Using a Stationary Deformation Source

When the magnetic robot is placed in the oil phase, it quickly settles to the water-oil interface, where it becomes trapped. The water-oil interface pins to the lower edge of the magnet. Owing to its weight, the magnet pulls downward, curving the interface. The interface profile pinned by the magnetic robot is similar to that of the interface pinned by the micropost in previous work [13] as shown in Figures 40a and 40c. Microspheres are then carefully introduced; those that settle near the robot sense the curvature field and migrate towards the robot's edge in a manner similar to the microsphere migration towards the stationary micropost, Figure 40b. A time-stamped image in the reference frame of the robot, Δt=1 sec, of microsphere trajectory is shown in Figure 40d, where the microsphere accelerates towards the magnetic robots as it migrates. Since the position of the magnetic

[1] https://youtu.be/5qOWN9MZKjo

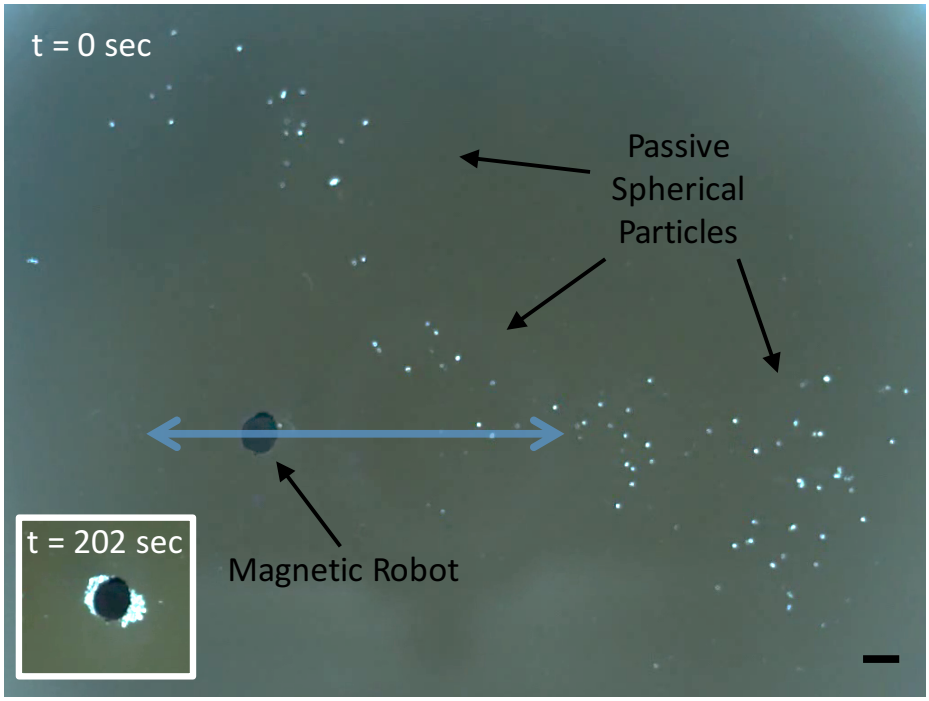

Figure 42: Directed capillary driven assembly using an actuated magnetic robot. Large image shows the distribution of particles at time, t = 0 sec. Inset shows particles attached to the magnetic robot at time, t = 202 sec. Scale bar is 2 mm.

robot is not fixed on the interface, it drifted slightly during the experiment, however, the drift is small compared to the movement of the microsphere.

7.4.2 Assembly Using a Mobile Deformation Source

Actuation allows the robot to collect particles initially sparsely dispersed on the interface, which would not occur with a stationary surface deformation structure such as the micro-post. For example, in Figure 42 the robot is driven back and forth along the x-axis. The particles are initially sparsely distributed. As the magnetic robot moves, the traveling surface deformation and flow associated with the robot motion cause the particles to migrate toward the center, and eventually to assemble on the robot, as shown in the inset. In this example, the orientation of the robot is held fixed; particles aggregate at the front and back side of the magnet.

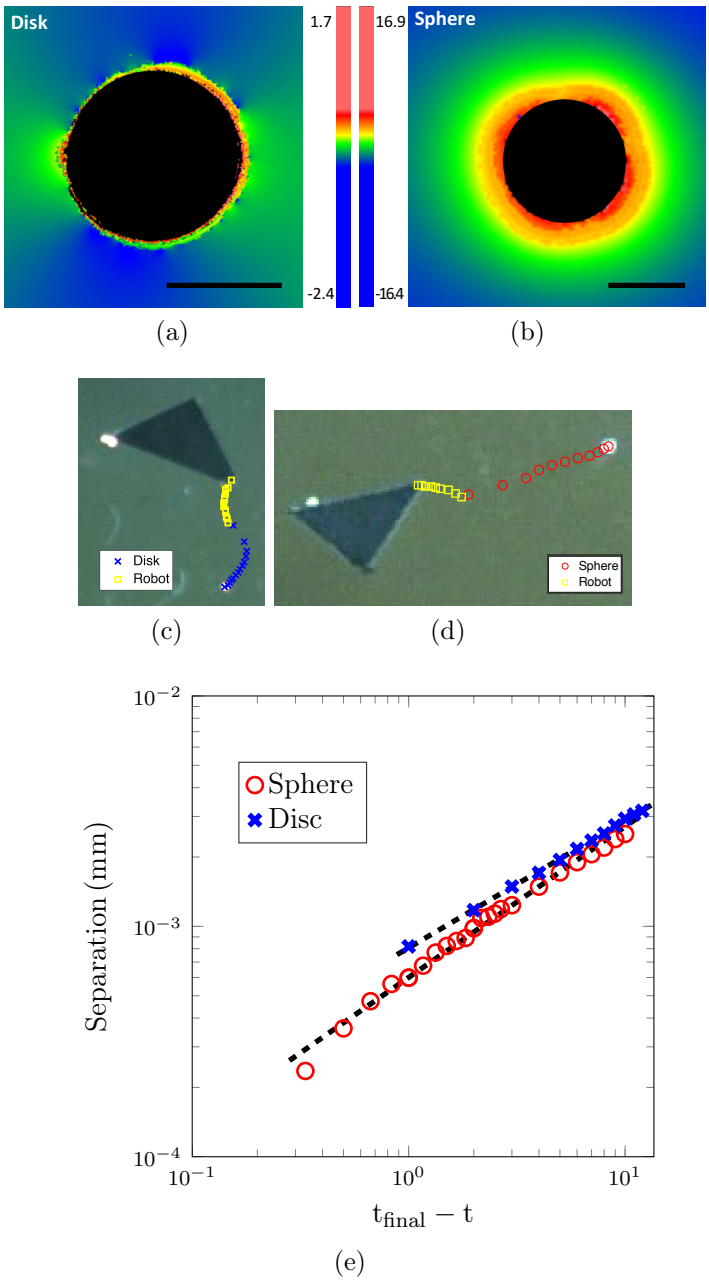

Figure 43: Geometry effects on assembly dynamics. Interferogram of passive particles (a) SU-8 microdisk and (b) glass sphere on an water-air interface. The peak-to-valley values are measured in μm. Scale bars are 100 μm. (c) Trajectory of disk assembly to the corner of the robot. (d) Trajectory of sphere assembly to the corner of the robot. (e) Euclidean separation distance between particle and robot docking location as a function of time to attachment for comparison between assembly rate of the disk and sphere to corner of the robot.

7.4.3 Geometry Effects on Assembly Dynamics

The interface shape around the robot depends on the robot weight and geometry. By tailoring the robot geometry, locations for preferred particle assembly can be defined. Corners are particularly interesting in this regard, as interfaces pinned to the corner of the robot have high curvature gradients. Such interface shapes exert high curvature capillary forces on passive particles, and should guide them to assemble at corners on the robot, Figs. 43c and 43d.

However, aberrations in the magnetic robot geometry like uncontrolled roughness arising from the cutting process can cause curvature to vary rapidly. Since such interface distortions decay with the characteristic wavelength of the roughness, these aberrations are important only in the near field, close to the robot surface [87]. Therefore, when the particle is close enough to the robot, the associated curvature fields can cause the passive particle to be attached to the robot's edge as opposed to its corner. With improved manufacturing techniques, such aberrations can be avoided, and more precise docking locations can be designed.

The shape and weight of the passive particle also affect the assembly dynamics. We experiment with two different passive particles, spheres and disks. The interferogram reveals the interface shape around the particle on otherwise planar interfaces, shown in Figs. 43a and 43b. Disks pin the interface on their weakly rough sides, and make distortions of only a few microns, as is evident in the heat map. More interestingly, these distortions exhibit a quadrupolar symmetry. In Figure 43a, starting at the east, and moving clockwise around the particle at some constant radius, the heat map changes from green, to blue, to green, and to blue again, indicating the interface has alternating regions of rise and fall around the circle, i.e. a $cos2\phi$ distribution. The spheres also pin the interface. In the far field, spheres can exhibit either a monopolar deformation, indicating that the particle weight is significant enough to pull down on the interface, or a quadrupolar deformation, suggesting that the particle weight is negligible [14]. Figure 43b shows that close to the sphere surface, the shape of the interface is irregular and a monopolar deformation is observed, which has a far longer range of interaction owing to its slow decay. Furthermore, the magnitude of

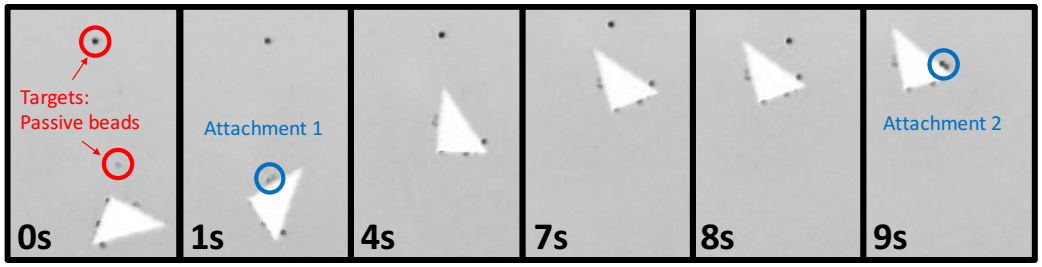

(a)

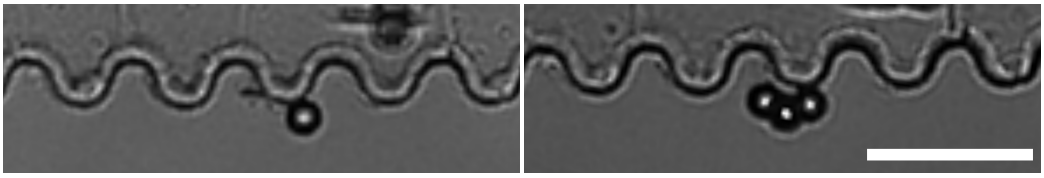

(b)

Figure 44: Small-scale features determine docking location. (a) The assembly of passive spheres to a triangular magnetic robot. By placing the robot at different poses relative to spheres, its attachment position of the particle to the robot can be controlled. The sphere attaches to the edge as opposed to the corners here because of surface roughness along the edge of the robot. Robot is teleoperated. Time in seconds is shown in each panel. (b) Microsphere attachment on stationary microstructure with undulated controlled roughness. Scale bar is 50 μm.

the deformation is an order of magnitude larger than that of the disk, which also implies a stronger interaction with the curvature field.

Figs. 43c and 43d shows the trajectory of the passive particle and the position of the docking location over time as the two approach and finally assemble for a disk and sphere, respectively. In both cases the trajectory of the particle is slightly curved, as expected. Since the magnetic field drives the triangle robot to move on the interface, this motion also induces flow on the interface. Even in the presence of this flow, disks and spheres quickly detect the change in the height profile and migrate to locations of steepest curvature. Figure 43e shows a log-log plot of the Euclidean separation distance between the passive particle and robot docking location, at the corner of a triangle robot, as a function of time to attachment (note that this reverses the time on the x-axis.) This plot shows that the sphere attaches to the robot faster than the disk of a similar diameter.

Inspired by the aberrant surface roughness that caused particles to dock on edges rather than corners, Figure 44a, we can design new docking motifs. By deliberately introducing

wavy edges, we can excite near field deformations that attract particles to preferred sites along the sides of the microstructure. Figure 44b shows how such undulations on a fixed curvature cue can create specified docking locations for particles.

7.5 Autonomous Assembly

Autonomous micromanipulation poses numerous challenges. Microscale interactions such as hydrodynamic forces, electrostatic forces and van der Waals forces are challenging to model. Moreover, tracking the robot and the object being manipulated can be challenging at these small length scales because imagery is often in low resolution, small particles can be difficult to differentiate and using tags to identify objects is not yet practical.

To create a system that is able to use capillary interactions for autonomous microassembly, we will need high-resolution manufacturing capabilities to create local regions of high curvature gradient that result in specified docking locations for passive particles. This sections discusses modifications to the system described above and presents experimental results demonstrating that predictable and repeatable autonomous assembly can be achieved by combining the design of preferential particle docking locations to the geometry of the robot with closed loop feedback for position control of the robot. Through an understanding of capillary interactions, we design geometric structures on the robot to create regions of high interface curvature to assemble passive microspheres with high specificity.

7.5.1 System Design Modifications for Autonomous Assembly

Robots

A material that can be machined with high-precision and with a high magnetic remanence is desired. This ensures first, that regions of high curvature gradient can be created and that there are minimal surface roughness affects that may cause more preferred docking locations for the passive particle as seen in the experiments in section 7.4. Secondly, a high magnetic remanence results in higher sensitivity of the robot motion to changes in magnetic field and allow the robot to be maneuvered throughout the workspace with higher resolution.

To that end, the robots in the following experiments are 500 μm thick Samarium Cobalt

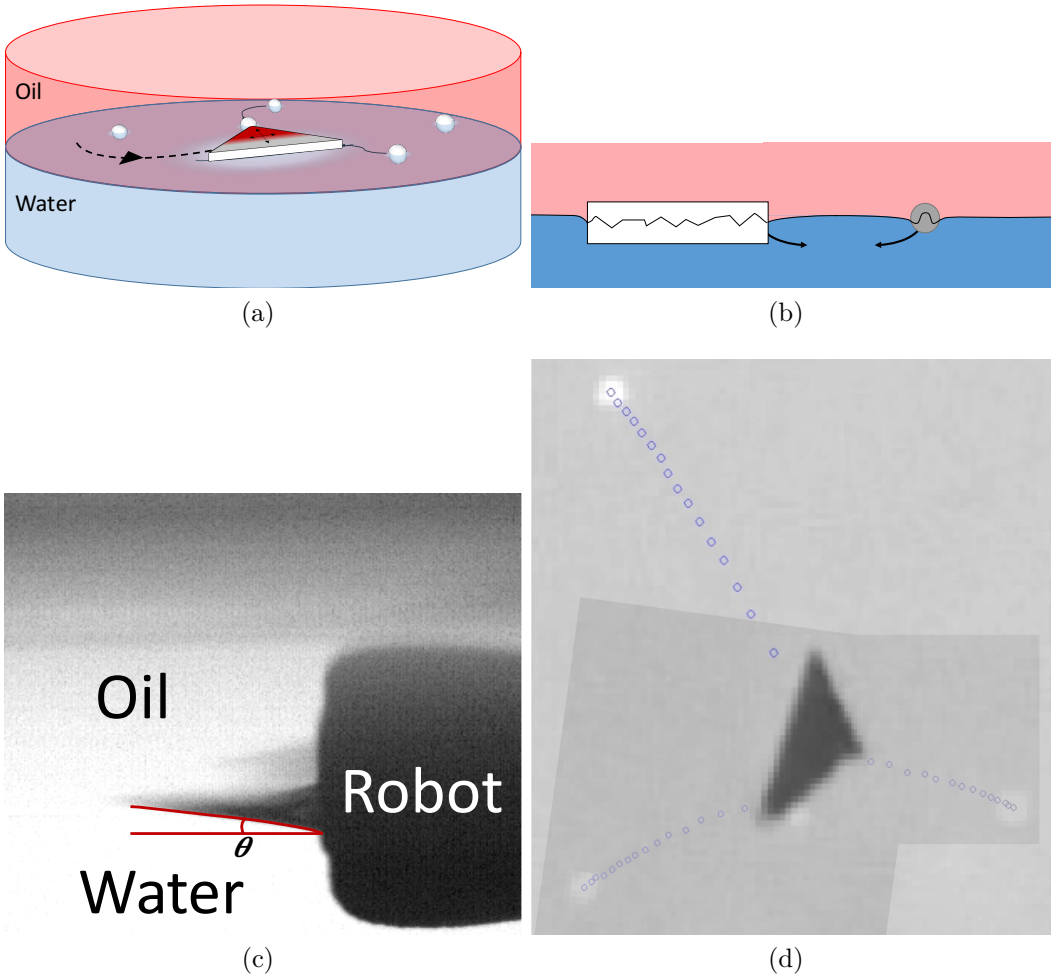

Figure 45: Autonomous robot for directed assembly (a) The magnetic robot (the triangle), magnetized along the plane, can be autonomously controlled to selectively assemble passive micro spheres. (b) Side view of the interface curvature caused by the robot and the sphere, (c) Side view of the curved fluid interface for a SmCo robot. The red lines indicate the angle of the interface at the edge of the robot with the horizontal, (d) Time-stamped image ($\Delta t = 0.5\,\text{sec}$) of 3 different initial positions and trajectories of microsphere assembly to the robot.

(SmCo) magnets. A laser is used to cut the SmCo to the desired geometry (IPG Microsystems IX-200-F). This fabrication method minimizes surface roughness. By minimizing surface roughness, attachment to a desired location can be highly specified because a single high curvature gradient dominates in the global as well as local region of the robot. Robots in the shape of triangles with edge lengths between 1-2 mm are used. Each corner creates a high curvature gradient which creates a desired docking location for passive microspheres. Figure 45b shows the goniometer image of the side view of the robot. The interface around the robot is downward sloping at approx. 10 °.

The direction of the magnetic dipole of the sheet of SmCo is into the plane. To ensure predictable dynamics of the robot, it is desirable to change the magnetic dipole of the SmCo to be along the plane of robot at the oil-water interface. To do this, the magnets are heated above the Curie temperature of SmCo, 800 °F to demagnetize the robots. The demagnetization of the robot can be verified using the magnetic manipulation system because the robot will not respond to applied magnetic fields. The robot is remagnetized in the desired orientation by bringing it close to a strong permanent magnet, Neodymium cylindrical magnet, Grade N42, Dia.: 15 mm L: 50 mm (D8Y0, K & J Magnetics, Inc.), and aligning the magnetic field lines to the desired magnetic dipole moment of the robot. The successful re-magnetization of the robot can also be verified using the magnetic manipulation system. While it is likely that there is some amount of remanent magnetization after heating the robot past the Curie temperature, for the purposes of these experiments, this method of re-magnetization is sufficient to create a magnetic robot with predictable dynamics as a result of an applied magnetic field.

The use of a rotationally asymmetric magnet allows the orientation of the robot to be tracked. This is important for control because the applied force and torque on the robot is a function of the magnetic dipole moment vector. For the isosceles triangle robots, a custom computer vision algorithm using the OpenCV libraries is designed to extract the orientation of the robot from the camera. As before, the image is first blurred using a Gaussian blur, a blob detector is used to determine the location of the robot. The blobs are filtered by size.

The contour of each blob is fit to a polygon using the Ramer-Douglas-Peucker algorithm (as implemented in the OpenCV libraries) [23, 59]. Then blobs that fit polygons with 3 edges are filtered out. This typically ensures that only one blob remains, which is the robot. If not, the candidate blobs are filtered based on proximity to the robot's last known location. Once the blob of the robot is known, the corners of the blob from the polygon fit are used to determine the corners corresponding to the longest edge. The orientation of the robot is determined relative to he longest edge. This algorithm runs at 20Hz, and has the potential to be optimized to run faster such as by narrowing the search space for blobs based on prior knowledge of where the robot was in the last frame and the maximum speed that the robot can travel.

Controller

A DAQ (Measurement Instrument, USB-3103) is used to control the current via a custom power electronics circuit. Each coil has a DC current supply and can carry up to $\pm 1\,\mathrm{A}$. The current is updated at $10\,\mathrm{Hz}$. We use a PI controller to move the robot to the desired position, which is defined manually. The current input, $\vec{u}$, is calculated by

$$\vec{u} = \vec{e}(t)k_p + \int_0^t \vec{e}(t)k_i \tag{7.4}$$

where $\vec{e}(t)$, is the position error between the goal and actual location at time t, $\vec{x}_{goal}(t) - \vec{x}_{actual}(t)$, k_p and k_i are the proportional and integral gain respectively. This equation returns two values for current inputs, while there are four electromagnetic coils. Depending on the sign of the input, different coils are activated such that only two coils are energized at each time, one along the x-axis and another along the y-axis. The coil corresponding to the direction in which the robot is moving is used, e.g. if the coil is moving in the positive x, the coil located in the positive x direction of the center of the workspace is used. To minimize the torque on the magnet, the direction of the magnetic field applied by each pair of magnetic coils along the axes is the same such that the magnet is always pointed within a $90\,^\circ$ envelope.

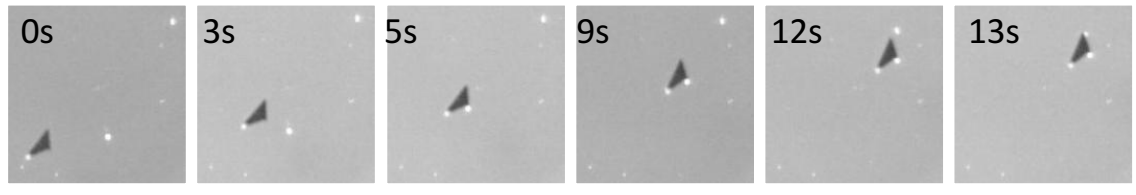

(a)

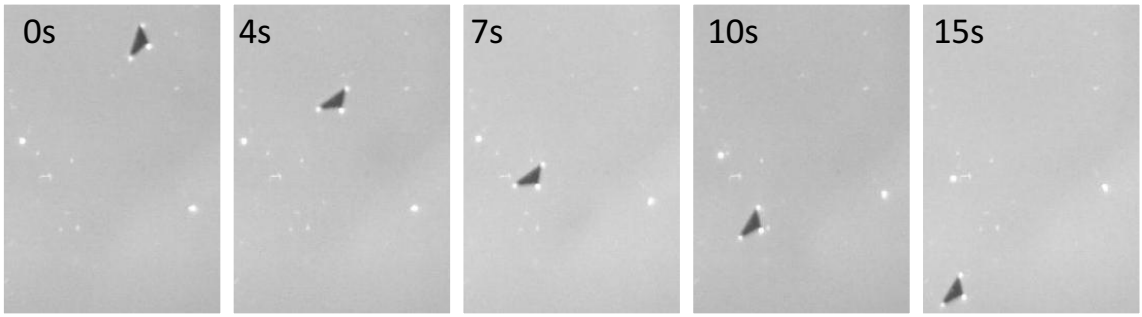

(b)

Figure 46: Assembly dynamics of microsphere assembly to triangular robot. Time series (a) robot moving toward 2 microspheres that assemble to the middle and top corner, (b) robot maneuvering around workspace while avoiding assembly to 2 microspheres.

Once the magnet reaches the desired position, all coils are turned off, allowing Earth's magnetic field to orient the magnet. Given the uniformity of Earth's magnetic field across the workspace, this method stably orientates the magnet to align with the Earth's magnetic field.

7.5.2 Results

Actuation of the robot enables the topology of the fluid interface to be dynamic, allowing microspheres to be assembled to the robot selectively. The geometry of the robot dictates the shape and axis of high interface curvature, which will create sites of preferred assembly for the microsphere. We demonstrate this by using a robot with 3 corners. The corners create regions of high interface curvature, when the interface distortion of the robot and of the microsphere overlap, the distance between the two will decrease to minimize the total capillary energy of that interaction. Capillary energy is minimized locally, thus the initial position of the microsphere relative to the robot will determine the assembly site of the microsphere to the robot, Figure 45d. Supplementary videos show examples of semi-

autonomous control of the robot to enable selective assembly of microspheres to specific sites on the robot by maneuvering to positions would present the desired site closest to the target microsphere.

Capillary force is a function of the relative distance between the robot and the microsphere. By maneuvering the robot to pass microspheres at the close proximity, assembly can be accomplished, Figure 46a. Assembly can be avoided by maintaining a larger distance from microspheres as well as a high velocity when moving past microspheres, Figure 46b. The parameters for assembly depend on the geometry of the robot and passive particles. Different shapes will result in different assembly dynamics. These interactions are difficult to derive empirically because of the high-resolution imaging necessary to determine details of the interface geometry. Instead, these interactions can be characterized empirically as demonstrated here.

7.6 Design Guidelines and Limitations

In order to explore the design of a magnetically actuated microrobotic system for specific applications, we can begin by considering the capabilities and limitations of the system. Here, we specifically quantify the capabilities of the 4-coil system that was introduced in Section 6.2.4 and also used in the assembly experiments in this chapter. Table 5 lists some of the key parameters and properties of this magnetic manipulation system.

With an estimate of the forces that can be exerted by our magnetic manipulation system, we can begin to consider applications that may or may not be feasible using such a system. We already demonstrated that the robots exert enough force to manipulate passive microscale particles on fluid interfaces. Some examples of tasks in minimally invasive medicine that may be appropriate for microrobots are discussed by Nelson et al. [47]. As an example, it may not be feasible to extract a cell sample from a tissue during minimally invasive surgery using a pulling force, as the force required for this task exceeds the force that can currently be exerted by magnetic robots at this scale. Given that large torques can be applied, perhaps a torquing motion to activate a tool would be more effective for

Table 5: Magnitude of key parameters for multi-magnet manipulation setup

Earth's magnetic field	O 10e-6	T
Applied magnetic field	O 10e-6	T
Magnetization of the robot	O 1e-4	Am^2
Robot velocity	O 1e-1	mm s^{-1}
Magnetic torque	O 1e-8	Nm
Damping torque	O 1e-8	Nm
Magnetic force	O 1e-9	N
Friction force	O 1e-9	N
Robot weight	O 1	g

removing a cell sample from tissue. On the other hand, tasks that require small forces and torques align well with the capabilities of the magnetic microrobot; for example, it may be feasible to perform rheological measurements for fluids by being able to track the rotation of a magnetic robot on top of a fluid.

Certainly, design modifications can be made to enhance specific capabilities. For a different design, a separate analysis would be necessary.

Spatial scales

An additional consideration is the ability to image the robot and the environment. In our systems, we have used cameras to track the pose of the robot using computer vision. This requires a clear and stationary fluid, ample lighting and line of sight between the camera and the robot. Additionally, this puts limitations on the visible workspace where the robot can be fully tracked.

Time scales

When designing a microrobotic system, depending on the application, different time scales will become important. In assembly, we can compare the timescale between capillary interaction of the particles and moving the robot. As shown in experiments earlier in this chapter, particles that create a smaller surface deformation and therefore have smaller capillary energy will typically assemble more slowly than particles that create larger surface deformation. For spheres of different sizes, larger spheres will assemble more quickly than

smaller spheres. This is an important consideration, especially as the system is scaled down.

When interfacing magnetic microrobots with biological organisms, we need to consider the time scales that biology operates compared to the time scales for manipulation. For example, in Chapter 3 where biological organisms are used as sensors manipulated by magnetic microrobotics, there is a large discrepancy between the time it takes to manipulate the biological payload, which is on the order of seconds; compared to the time for gene expression, which is on the order of hours. There are other biological reactions that have shorter response times, such as protein-protein interactions, which occur instantaneously.

7.7 Conclusion

In this chapter, we developed a system which uses magnetic robots as the interface curvature source to guide the assembly of passive unactuated particles at liquid interfaces. We explored the assembly of SU-8 disks and glass spheres on the water-oil interface to study the effect of geometry on directed assembly. In the case of passive assembly, spheres and disks migrate to the high curvature sites at the edge of the circular magnetic robots. In active assembly, by controlling the motion of the robot, particles assemble to preferred locations around the robot based on the velocity of the robot and the orientation of the robot relative to the particle. Moreover, geometric cues can also direct particles to assemble to corners and rough sites. By strategically designing the geometry of the robot, preferred docking sites for passive particles can be created. We demonstrate semi-autonomous microassembl, we manually identify the initial position of the microsphere and command the required position of the robot to obtain the desired assembly, the robot is controlled autonomously using closed-loop visual feedback to the planned goal position to achieve predictable assembly of the microsphere to the robot. This system enables spatial and temporal control of surface curvature and suggests new opportunities to create complex and reconfigurable assemblies. As an extension to the application of micro magnetic robots, we explore design considerations and limitations of our system and create guidelines which are important to consider when determining feasible applications for micro magnetic robots.

Chapter 8

Conclusion

8.1 Contributions

Unique challenges arise when building microscale robots, macroscale robots cannot simply be miniaturized. This dissertation makes several contributions towards creating swarms of microrobots that can be controlled with high-precision and sense the environment. We investigate methods to integrate biological organisms with synthetic components to create hybrid organic-inorganic microbiorobots.

We begin by exploring the use of biological organisms, specifically bacteria, for sensing and actuation. Chapter 3 presents the use of synthetically engineered biological cells for sensing onboard microrobots to create a system capable of detecting a change in the local environment, storing and reporting the information. We demonstrated the integration of microrobotic actuation techniques with engineered cells to create mobile biosensors. For this proof-of-concept prototype, we used cells that were programmed to respond to and report on exposure to UV light. This is the first time low power toggle cells have been attached as biosensors on to robots, a significant achievement that promises a pathway for transitioning research in synthetic biology to robotics. These results have implications for incorporating other synthetically engineered cells that can serve as chemical sensors, data-loggers, or quorum sensors onboard microbiorobotic systems. This work paves the path for using synthetic biology as a technique to integrate new capabilities into microrobots, and

provides an alternative path to microfabricating organic signal processors, power sources, and memory units.

In Chapter 4, we use bacteria attached to microstructures to create un-tethered microbiorobots with onboard power. We present two models, first, a top-down stochastic kinematic model, which informs the second, a bottom-up chemotactic model. We demonstrate that the top-down stochastic kinematic model is able to capture the biased clockwise rotation of microbiorobots propelled by flagellated bacteria which are adhered to the surface of the robot. The model is validated by three different experiments to determine the force exerted at different locations on the microbiorobot. The force contribution by free-swimming bacteria in solution colliding with the sides of the microbiorobot is investigated by observing the dynamics of micro structures powered by the active suspension compared to microbiorobots powered by bacteria attached to the micro structure. Our bottom-up model of bacteria propelled microstructures is able to capture the stochasticity of cell behavior. This chapter makes contributions towards steering bacteria propelled microbiorobots using external stimuli, such as using patterned light to control the dynamics of microbiorobots [34, 72].

Magnetic fields are used to deterministically actuate magnetic microrobots. Chapter 5 explores the characterization of our magnetic manipulation system to create a model that would enable the implementation of novel control schemes for both single and multi-robot control. Chapter 6 explores the control of multiple magnetic robots which are affected by the same global field. We provide a model for controlling magnets using the spatially varying gradient of the magnetic field close to the electromagnetic coil and the superposition of the independent fields generated by several stationary electromagnetic coils. A model, simulation and experiments are shown for a one-dimensional systems as well as a planar system. Our force-based control algorithm allows un-coupled independent control of multiple magnetic robots. Chapter 7 presents a system which uses magnetic robots as the interface curvature source to control the assembly of passive unactuated micro particles at fluid interfaces. We explore the effect of geometry of both the robot and the passive building

blocks on the assembly dynamics and the ability to design assembly configurations through these geometries. With an understanding of the assembly dynamics, we demonstrate that autonomous microassembly is possible, which has applications in microassembly of complex structures. While having implications in the field of microrobotics, this work also has implications in the field of soft matter, where being able to repeatedly probe a system in a controlled manner is powerful.

8.2 Future Work

8.2.1 Organic and Inorganic Microrobots

Biology will continue to play a crucial role as robots scale down, both as components on microrobots and also microrobots will be an indispensable tool in the biological sciences. Continued developments in synthetic biology will enable biosensors that are integrated into cells that are capable of sensing a wide array of stimuli such as toxins, metals, salinity, pH, temperature and light. These responses can be integrated into a more complex biomolecular network that will filter and amplify the inputs to allow it to be processed for logical operations. With specialized microbiorobots, a swarm of heterogeneous microbiorobots can create a communication network to sense and modify an environment in a coordinated fashion. The behavior at the microscale can also be linked to larger scale robots to create a two-way micro-to-macro world interface where signals at the microscale can be interpreted and communicated to the macroscale and commands can be broadcast from the macroscale to the microrobots.

In the biological sciences, microrobots can be used to synthesize desired behaviors in populations of bacterial and mammalian cells by delivering chemicals or expediting and controlling the transport of cells that secrete chemicals. With advancements in automation of micro machines, microrobots will also play a role advancing and standardizing synthetic biology.

8.2.2 Magnetic Robots for Probing Scientific Phenomenon

The magnetic microrobot manipulation system used to demonstrate capillary driven assembly can be extended by engineering functionalities into the passive building blocks. For example, chemical sensors can be incorporated into the robot to enable them to sense and report on their surroundings. Furthermore, the robot can also be imbued with hierarchical structures and additional functions.

As we improve the manufacturing processes for the magnetic robot and develop model-based nonlinear control algorithms derived from our understanding of the interfacial mechanics and curvature affects, we will develop the ability to predict the trajectories of the particles in response to the robot deformation field. This will enable us to plan trajectories through a crowded interface while avoiding unwanted interactions en route to a selected particle to collect it or to interrogate it. A controller that does not require *a priori* knowledge of the system parameters would enable the same controller to be used for different shaped robots.

This work could also feed back into the field of soft matter and materials science. With spatial and temporal control of a fluid interface curvature source, the assemblies can be reconfigured by locally changing the stresses of the material. In essence, the device acts as the master, while the passive particles follow its direction. Designing the master is the key towards hierarchical assembly on interfaces.

Future work will involve implementing automation to enable the assembly of complex predefined structures and also consider capabilities that would allow assembled structures to be released from the magnet. Furthermore, the size of the robot can be scaled down to more precisely interact with smaller passive particles.

8.2.3 Multi-Robot Control

The control scheme introduced for multi-magnetic robot control has applications in micromanipulation for automated high-throughput biological experiments and use inside microfluidic channels for analysis and microassembly. Validating the algorithm on the microscale would

enable applications in micromanipulation and extensions to micromanpulation. Furthermore, it would be possible to incorporate more electromagnetic coils to extend control to more degrees-of-freedom. Additionally, more robust controllers can be developed to take into account critical points that arise based on the current input configuration to improve accuracy of trajectory following as well as introduce a new strategy for controlling swarms of magnetic robots.

8.3 Concluding Remarks

This dissertation presents several strategies to address challenges which arise when creating microscale robots. We consider each challenge individually to present a collection of modular methods that can be combined to create microrobots with a suite of capabilities. Each method is validated with a model as well as experimental demonstration of the potential of that technology. Depending on the specifications of the microscale system that is desired, different strategies will be more useful. It is worth noting that combining this methods is non-trivial. Future work in microrobotics will be a cross-disciplinary endeavor. It will combine these strategies into a single system while continuing to make these individual strategies more robust, reliable and accurate. In synthetic biology, engineered cells with an array of sensing capability with more robust signals that have high signal-to-noise ratio are needed. In interface science, a highly detailed model of the interactions at the interface would enable creation of complex structures through automated directed assembly. We hope that the work in this dissertation will help create swarms of microrobots with an ensemble of manipulation and sensing capabilities working together to be able to sense and modify the environment.

Bibliography

[1] J. J. Abbott, O. Ergeneman, M. P. Kummer, A. M. Hirt, and B. J. Nelson. Modeling magnetic torque and force for controlled manipulation of soft-magnetic bodies. *IEEE Transactions on Robotics*, 23(6):1247–1252, 2007. 52

[2] J. J. Abbott, M. C. Lagomarsino, L. Zhang, L. Dong, and B. J. Nelson. How should microrobots swim? *Intl. J. of Robotics Research*, 28(11-12):1434–1447, 2009. 85, 97

[3] A. Becker, G. Habibi, J. Werfel, M. Rubenstein, and J. McLurkin. Massive uniform manipulation: Controlling large populations of simple robots with a common input signal. In *Intelligent Robots and Systems (IROS), 2013 IEEE/RSJ International Conference on*, pages 520–527. IEEE, 2013. 9

[4] B. Behkam and M. Sitti. Bacterial flagella-based propulsion and on/off motion control of microscale objects. *Applied Physics Letters*, 90(2):023902, 2007. 7, 27

[5] J. Belcher, P. Dourmashkin, S.-b. Liao, D. Litster, N. Derby, and S. Olbert. Mit physics 8.02 electricity and magnetism, 2004 (accessed November 2014). 51

[6] H. C. Berg. Motile behavior of bacteria. *Physics Today*, 53(1):24–29, 2000. 31, 44

[7] L. Botto, E. P. Lewandowski, M. Cavallaro, and K. J. Stebe. Capillary interactions between anisotropic particles. *Soft Matter*, 8:9957–9971, 2012. 98

[8] G. Bradski. The opencv library. *Dr. Dobb's Journal of Software Tools*, 2000. 70, 81, 103

[9] D. Bray. Bacterial chemotaxis in silico. 46

[10] D. J. Cappelleri, P. Cheng, J. Fink, B. Gavrea, and V. Kumar. Automated assembly for mesoscale parts. *Automation Science and Engineering, IEEE Transactions on*, 8(3):598–613, July 2011. 97

[11] D. J. Cappelleri, D. Efthymiou, A. Goswami, N. Vitoroulis, and M. M. Zavlanos. Towards mobile microrobot swarms for additive manufacturing. *International Journal of Advanced Robotic Systems*, 11(150), 2014. 10

[12] C. Cassandras and S. Lafortune. *Introduction to Discrete Event Systems*. Dordrecht: Kluwer, 1999. 31

[13] M. Cavallaro, L. Botto, E. P. Lewandowski, M. Wang, and K. J. Stebe. Curvature-driven capillary migration and assembly of rod-like particles. *Proc. Natl. Acad. Sci. USA*, 108(52):20923–20928, 2011. 99, 101, 104

[14] D. Chan, J. Henry, and L. White. The interaction of colloidal particles collected at fluid interfaces. *Journal of Colloid and Interface Science*, 79(2):410–418, 1981. 99, 107

[15] U. K. Cheang, K. Lee, A. A. Julius, and M. J. Kim. Multiple-robot drug delivery strategy through coordinated teams of microswimmers. *Applied Physics Letters*, 105(8):083705, 2014. 9

[16] P. J. Choi, L. Cai, K. Frieda, and X. S. Xie. A stochastic single-molecule event triggers phenotype switching of a bacterial cell. *Science*, 322:442, 2008. 20

[17] S. Chowdhury, W. Jing, P. Jaron, and D. J. Cappelleri. Path planning and control for autonomous navigation of single and multiple magnetic mobile microrobots. In *ASME International Design Engineering Technical Conferences (IDETC)*, Boston, MA, 2015. 10

[18] N. Darnton, L. Turner, K. Breuer, and H. C. Berg. Moving fluid with bacterial carpets. *Biophysical Journal*, 86(3):1863 – 1870, 2004. 6

[19] R. Di Leonardo, L. Angelani, D. Dell'arciprete, G. Ruocco, V. Iebba, S. Schippa, M. P. Conte, F. Mecarini, F. De Angelis, and E. Di Fabrizio. Bacterial ratchet motors. *Proceedings of the National Academy of Sciences of the United States of America*, 107(21):9541–5, May 2010. 38, 39

[20] E. Diller, S. Floyd, C. Pawashe, and M. Sitti. Control of Multiple Heterogeneous Magnetic Microrobots in Two Dimensions on Nonspecialized Surfaces. *IEEE Transactions on Robotics*, pages 1–11, 2011. 9

[21] W. R. DiLuzio, L. Turner, M. Mayer, P. Garstecki, D. B. Weibel, H. C. Berg, and G. M. Whitesides. Escherichia coli swim on the right-hand side. *Nature*, 435(30):1271–4, jun 2005. 6

[22] M. Dkhil, M. Kharboutly, A. Bolopion, S. Régnier, and M. Gauthier. Closed-loop control of a magnetic particle at the air-liquid interface. PP(99):1–13, 2015. 97

[23] D. H. Douglas and T. K. Peucker. Algorithms for the reduction of the number of points required to represent a digitized line or its caricature. *Cartographica: The International Journal for Geographic Information and Geovisualization*, 10(2):112–122, 1973. 112

[24] Y. Du, E. Lo, S. Ali, and A. Khademhosseini. Directed assembly of cell-laden microgels for fabrication of 3d tissue constructs. *Proceedings of the National Academy of Sciences*, 105(28):9522–9527, 2008. 97, 99

[25] Fischer, P and A. Ghosh. Magnetically actuated propulsion at low Reynolds number: towards nanoscale control. *Nanoscale*, 3:557–563, 2011. 8, 97

[26] A. E. Friedland, T. K. Lu, X. Wang, D. Shi, G. Church, and J. J. Collins. Synthetic gene networks that count. *science*, 324(5931):1199–1202, 2009. 8

[27] P. D. Frymier, R. M. Ford, H. C. Berg, and P. T. Cummings. Three-dimensional tracking of motile bacteria near a solid planar surface. *Proceedings of the National Academy of Sciences of the United States of America*, 92(13):6195–9, 1995. 6, 46

[28] T. S. Gardner, C. R. Cantor, and J. J. Collins. Construction of a genetic toggle switch in Escherichia coli. *Nature*, 403:339–342, 2000. 8, 14, 17, 19

[29] D. T. Gillespie. A general method for numerically simulating the stochastic time evolution of coupled chemical reactions. *Journal of Computational Physics*, 22:403–434, 1976. 44

[30] D. Griffiths. *Introduction to Electrodynamics*. Always learning. Pearson, 2013. 55

[31] G. Grosjean, G. Lagubeau, A. Darras, M. Hubert, G. Lumay, and N. Vandewalle. Remote control of self-assembled microswimmers. *Scientific reports*, 5, 2015. 97

[32] G. Guennebaud, B. Jacob, et al. Eigen v3. http://eigen.tuxfamily.org, 2010. 87

[33] M. Hagiwara, T. Kawahara, and F. Arai. Local streamline generation by mechanical oscillation in a microfluidic chip for noncontact cell manipulations. *Applied Physics Letters*, 101(7), 2012. 97

[34] E. E. Hunter, N. Chodosh, E. B. Steager, and V. Kumar. Control of microstructures propelled via bacterial baths. In *2016 IEEE International Conference on Robotics and Automation (ICRA)*, pages 1693–1700. IEEE, 2016. 7, 118

[35] W. Jing and D. Cappelleri. A magnetic microrobot with in situ force sensing capabilities.

Robotics, 3(2):106–119, 2014. 9

[36] W. Jing, X. Chen, S. Lyttle, Z. Fu, Y. Shi, and D. J. Cappelleri. Design of a micro-scale magnetostrictive asymmetric thin film bimorph (μmab) microrobot. In *ASME 2010 International Mechanical Engineering Congress and Exposition*, pages 599–607, 2010. 8

[37] J. D. Keuning, J. de Vriesy, L. Abelmanny, and S. Misra. Image-based magnetic control of paramagnetic microparticles in water. In *IEEE/RSJ International Conference on Intelligent Robots and Systems*, pages 421–426, Sept 2011. 97

[38] I. S. M. Khalil, F. van den Brink, O. S. Sukas, and S. Misra. Microassembly using a cluster of paramagnetic microparticles. pages 5527–5532, 2013. 9

[39] H. Kobayashi, M. Kærn, M. Araki, K. Chung, T. S. Gardner, C. R. Cantor, and J. J. Collins. Programmable cells: interfacing natural and engineered gene networks. *Proceedings of the National Academy of Sciences of the United States of America*, 101(22):8414–8419, 2004. 19

[40] M. P. Kummer, J. J. Abbott, B. E. Kratochvil, R. Borer, A. Sengul, and B. J. Nelson. Octomag: An electromagnetic system for 5-dof wireless micromanipulation. 26(6):1006–1017, 2010. 8, 49

[41] E. Lauga, W. R. DiLuzio, G. M. Whitesides, and H. A. Stone. Swimming in circles: motion of bacteria near solid boundaries. *Biophysical journal*, 90(2):400–12, Jan. 2006. 30, 37

[42] A. W. Mahoney, N. D. Nelson, K. E. Peyer, B. J. Nelson, and J. J. Abbott. Behavior of rotating magnetic microrobots above the step-out frequency with application to control of multi-microrobot systems. *Applied Physics Letters*, 104(14):144101, 2014. 9

[43] S. Martel and M. Mohammadi. Using a swarm of self-propelled natural microrobots in the form of flagellated bacteria to perform complex micro-assembly tasks. In *Robotics and Automation (ICRA), 2010 IEEE International Conference on*, pages 500–505, May 2010. 98

[44] S. Martel, C. C. Tremblay, S. Ngakeng, and G. Langlois. Controlled manipulation and actuation of micro-objects with magnetotactic bacteria. *Applied Physics Letters*, 89(23):233904, 2006. 27

[45] J. E. Martin and A. Snezhko. Driving self-assembly and emergent dynamics in colloidal suspensions by time-dependent magnetic fields. *Reports on Progress in Physics*, 76(12):126601, 2013. 98

[46] D. C. Meeker, E. H. Maslen, R. C. Ritter, and F. M. Creighton. Optimal realization of arbitrary forces in a magnetic stereotaxis system. *IEEE Trans. on Magnetics*, 32(2):320–328, 1996. 52

[47] B. J. Nelson, I. K. Kaliakatsos, and J. J. Abbott. Microrobots for minimally invasive medicine. *Annual review of biomedical engineering*, 12:55–85, 2010. 49, 114

[48] N. D. Nelson and J. J. Abbott. Generating two independent rotating magnetic fields with a single magnetic dipole for the propulsion of untethered magnetic devices. In *IEEE International Conference on Robotics and Automation*, pages 4056–4061, 2015. 10

[49] J. M. K. Ng, M. J. Fuerstman, B. A. Grzybowski, H. A. Stone, and G. M. Whitesides. Self-assembly of gears at a fluid/air interface. *J. Am. Chem.l Soc.*, 125(26):7948–7958, 2003. 98

[50] A. Novick and M. Weiner. Enzyme induction as an all-or-none phenomenon. *Proceedings*

of the National Academy of Sciences, 43:553–566, 1957. 20

[51] B. J. Park, T. Brugarolas, and D. Lee. Janus particles at an oil-water interface. *Soft Matter*, 7:6413–6417, 2011. 99

[52] C. Pawashe, S. Floyd, and M. Sitti. Modeling and Experimental Characterization of an Untethered Magnetic Micro-Robot. *Intl. J. of Robotics Research*, 28(8):1077–1094, July 2009. 8

[53] C. Pawashe, S. Floyd, and M. Sitti. Multiple magnetic microrobot control using electrostatic anchoring. *Applied Physics Letters*, 94(16):164108, 2009. 10

[54] R. Pelrine, A. Wong-Foy, B. McCoy, D. Holeman, R. Mahoney, G. Myers, J. Herson, and T. Low. Diamagnetically levitated robots: An approach to massively parallel robotic systems with unusual motion properties. In *IEEE International Conference on Robotics and Automation*, pages 739–744, 2012. 10

[55] A. Petruska, J. Edelmann, and B. Nelson. Model-based calibration for magnetic manipulation. *In-review*, 2016. 55

[56] A. Petruska and B. Nelson. Minimum bounds on the number of electromagnets required for remote magnetic manipulation. 31(3):714–722, June 2015. 88

[57] E. M. Purcell. Life at low reynolds number. *Am. J. Phys*, 45(1):3–11, 1977. 6

[58] P. E. Purnick and R. Weiss. The second wave of synthetic biology: from modules to systems. *Nature Reviews Molecular Cell Biology*, 10(6):410–422, 2009. 8, 12

[59] U. Ramer. An iterative procedure for the polygonal approximation of plane curves. *Computer Graphics and Image Processing*, 1(3):244 – 256, 1972. 112

[60] K. Rinaudo, L. Bleris, R. Maddamsetti, S. Subramanian, R. Weiss, and Y. Benenson. A universal rnai-based logic evaluator that operates in mammalian cells. *Nature biotechnology*, 25(7):795–801, 2007. 8

[61] M. S. Sakar, E. B. Steager, D. H. Kim, A. A. Julius, M. Kim, V. Kumar, and G. J. Pappas. Modeling, control and experimental characterization of microbiorobots. *Intl. J. of Robotics Research*, 30(6):647–658, 2011. 7, 27, 28, 31

[62] M. S. Sakar, E. B. Steager, D. H. Kim, A. A. Julius, M. J. Kim, V. Kumar, and G. J. Pappas. Biosensing and actuation for microbiorobots. In *IEEE International Conference on Robotics and Automation*, pages 3141–3146, Anchorage, AL, 2010. 12

[63] M. S. Sakar, E. B. Steager, D. H. Kim, M. J. Kim, G. J. Pappas, V. Kumar, et al. Single cell manipulation using ferromagnetic composite microtransporters. *Applied physics letters*, 96(4):043705, 2010. 14

[64] N. Sharifi-Mood, I. B. Liu, and K. J. Stebe. Curvature capillary migration of microspheres. *Soft Matter*, 11:6768–6779, 2015. 99, 100, 101, 102

[65] A. Sokolov, M. M. Apodaca, B. a. Grzybowski, and I. S. Aranson. Swimming bacteria power microscopic gears. *Proceedings of the National Academy of Sciences of the United States of America*, 107(3):969–74, Jan. 2010. 35, 38, 39

[66] D. Stamou, C. Duschl, and D. Johannsmann. Long-range attraction between colloidal spheres at the air-water interface: The consequence of an irregular meniscus. *Phys. Rev. E*, 62:5263–5272, 2000. 99

[67] E. Steager, C.-B. Kim, J. Patel, S. Bith, C. Naik, L. Reber, and M. J. Kim. Control of microfabricated structures powered by flagellated bacteria using phototaxis. *Applied Physics Letters*, 90(26):263901, 2007. 7, 27, 34

[68] E. Steager, M. S. Sakar, U. K. Cheang, D. Casale, V. Kumar, G. J. Pappas, and M. J. Kim. Galvanotactic control of self-powered microstructures. In *ASME 2008 International Mechanical Engineering Congress and Exposition*, pages 365–370. American

Society of Mechanical Engineers, 2008. 7

[69] E. B. Steager, M. S. Sakar, D. H. Kim, V. Kumar, G. J. Pappas, and M. J. Kim. Electrokinetic and optical control of bacterial microrobots. *Journal of Micromechanics and Microengineering*, 21:035001, 2011. 8

[70] E. B. Steager, M. S. Sakar, C. Magee, M. Kennedy, A. Cowley, and V. Kumar. Automated biomanipulation of single cells using magnetic microrobots. In *IEEE International Conference on Robotics and Automation*, Minneapolis, Minnesota, 2012. 49

[71] E. B. Steager, M. S. Sakar, C. Magee, M. Kennedy, A. Cowley, and V. Kumar. Automated biomanipulation of single cells using magnetic microrobots. *Intl. J. of Robotics Research*, 32(3):346–359, 2013. 8, 9, 14, 21

[72] E. B. Steager, D. Wong, N. Chodosh, and V. Kumar. Optically addressing microscopic bioactuators for real-time control. In *Robotics and Automation (ICRA), 2015 IEEE International Conference on*, pages 3519–3524. IEEE, 2015. 118

[73] E. B. Steager, D. Wong, D. Mishra, R. Weiss, and V. Kumar. Sensors for micro bio robots via synthetic biology. In *IEEE International Conference on Robotics and Automation*, pages 3783–3788, 2014. 9, 12

[74] E. B. Steager, B. Zern, M. S. Sakar, V. Muzykantov, and V. Kumar. Assessment of protein binding with magnetic microrobots in fluid. In *IEEE International Conference on Robotics and Automation*, pages 5502–5507, 2013. 9, 41

[75] S. H. Strogatz. *Nonlinear dynamics and chaos: with applications to physics, biology, chemistry, and engineering*. Westview press, 2014. 87

[76] Y. Sun, B. J. Nelson, D. P. Potasek, and E. Enikov. A bulk microfabricated multi-axis capacitive cellular force sensor using transverse comb drives. *J. of Micromechanics and Microengineering*, 12(6):832, 2002. 9

[77] J. J. Tabor, H. M. Salis, Z. B. Simpson, A. A. Chevalier, A. Levskaya, E. M. Marcotte, C. A. Voigt, and A. D. Ellington. A synthetic genetic edge detection program. *Cell*, 137(7):1272–1281, 2009. 8

[78] S. Tasoglu, E. Diller, S. Guven, M. Sitti, and U. Demirci. Untethered micro-robotic coding of three-dimensional material composition. *Nature communications*, 5, 2014. 98

[79] B. Véron, A. Hubert, J. Abadie, and N. Andreff. Geometric analysis of the singularities of a magnetic manipulation system with several mobile coils. In *IEEE/RSJ International Conference on Intelligent Robots and Systems*, pages 4996–5001, 2013. 88

[80] M. Wang, L. He, and Y. Yin. Magnetic field guided colloidal assembly. *Materials Today*, 16(4):110 – 116, 2013. 98

[81] L. Weiss, J. Badalamenti, L. Weaver, A. Tascone, P. Weiss, T. Richard, and P. Cirino. Engineering motility as a phenotypic response to luxi/r-dependent quorum sensing in escherichia coli. *Biotechnology and Bionengineering*, 100:1251–1255, 2008. 8

[82] D. Wong, E. E. Beattie, E. B. Steager, and V. Kumar. Effect of surface interactions and geometry on the motion of micro bio robots. *Applied Physics Letters*, 103(15):153707, 2013. 27

[83] D. Wong, I. B. Liu, E. B. Steager, K. J. Stebe, and V. Kumar. Directed micro assembly of passive particles at fluid interfaces using magnetic robots. In *Manipulation, Automation and Robotics at Small Scales (MARSS), International Conference on*, pages 1–6. IEEE, 2016. 96

[84] D. Wong, E. Steager, and V. Kumar. Independent control of identical magnetic robots in a plane. *Robotics and Automation Letters, IEEE*, accepted, 2016. 64

[85] D. Wong, E. B. Steager, and V. Kumar. Near-wall dynamics and photoresponse of

swimming microbiorobots. In *ASME 2012 International Design Engineering Technical Conferences and Computers and Information in Engineering Conference*, volume 5, pages 205–212, DETC2012-71033, 2012. 27

[86] D. Wong, J. Wang, E. B. Steager, and V. Kumar. Control of multiple magnetic micro robots. In *ASME 2015 International Design Engineering Technical Conferences and Computers and Information in Engineering Conference*, number DETC2015-47683, 2015. 64

[87] L. Yao, L. Botto, M. Cavallaro, Jr, B. J. Bleier, V. Garbin, and K. J. Stebe. Near field capillary repulsion. *Soft Matter*, 9:779–786, 2013. 99, 101, 107

[88] L. Yao, N. Sharifi-Mood, I. B. Liu, and K. J. Stebe. Capillary migration of microdisks on curved interfaces. *J. Colloid Interface Sci.*, 449:436 – 442, 2015. 100, 101

[89] J. Zhuang and M. Sitti. Chemotaxis of bio-hybrid multiple bacteria-driven microswimmers. *Scientific reports*, 6, 2016. 7